The Electronically Steerable Parasitic Array Radiator Antenna for Wireless Communications: Signal Processing and Emerging Techniques

Rongrong Qian

Submitted for the degree of Doctor of Philosophy

Heriot-Watt University

Institute of Sensors, Signals and Systems

School of Engineering & Physical Sciences

April 2015

The copyright in this thesis is owned by the author. Any quotation from the thesis or use of any of the information contained in it must acknowledge this thesis as the source of the quotation or information.

ABSTRACT

Smart antenna technology is expected to play an important role in future wireless communication networks in order to use the spectrum efficiently, improve the quality of service, reduce the costs of establishing new wireless paradigms and reduce the energy consumption in wireless networks. Generally, smart antennas exploit multiple widely spaced active elements, which are connected to separate radio frequency (RF) chains. Therefore, they are only applicable to base stations (BSs) and access points, by contrast with modern compact wireless terminals with constraints on size, power and complexity. This dissertation considers an alternative smart antenna system the electronically steerable parasitic array radiator (ESPAR) which uses only a single RF chain, coupled with multiple parasitic elements. The ESPAR antenna is of significant interest because of its flexibility in beamforming by tuning a number of easy-to-implement reactance loads connected to parasitic elements; however, parasitic elements require no expensive RF circuits. This work concentrates on the study of the ESPAR antenna for compact transceivers in order to achieve some emerging techniques in wireless communications.

The work begins by presenting the work principle and modeling of the ESPAR antenna and describes the reactance-domain signal processing that is suited to the single active antenna array, which are fundamental factors throughout this thesis. The major contribution in this chapter is the adaptive beamforming method based on the ESPAR antenna. In order to achieve fast convergent beamforming for the ESPAR antenna, a modified minimum variance distortionless response (MVDR) beamfomer is proposed. With reactance-domain signal processing, the ESPAR array obtains a correlation matrix of receive signals as the input to the MVDR optimization problem. To design a set of feasible reactance loads for a desired beampattern, the MVDR optimization problem is reformulated as a convex optimization problem constraining an optimized weight vector close to a feasible solution. Finally, the necessary reactance loads are optimized by iterating the

convex problem and a simple projector. In addition, the generic algorithm-based beamforming method has also studied for the ESPAR antenna.

Blind interference alignment (BIA) is a promising technique for providing an optimal degree of freedom in a multi-user, multiple-inputsingle-output broadcast channel, without the requirements of channel state information at the transmitters. Its key is antenna mode switching at the receive antenna. The ESPAR antenna is able to provide a practical solution to beampattern switching (one kind of antenna mode switching) for the implementation of BIA. In this chapter, three beamforming methods are proposed for providing the required number of beampatterns that are exploited across one super symbol for creating the channel fluctuation patterns seen by receivers. These manually created channel fluctuation patterns are jointly combined with the designed spacetime precoding in order to align the inter-user interference. Furthermore, the directional beampatterns designed in the ESPAR antenna are demonstrated to improve the performance of BIA by alleviating the noise amplification.

The ESPAR antenna is studied as the solution to interference mitigation in small cell networks. Specifically, ESPARs analog beamforming presented in the previous chapter is exploited to suppress inter-cell interference for the system scenario, scheduling only one user to be served by each small BS at a single time. In addition, the ESPAR-based BIA is employed to mitigate both inter-cell and intra-cell interference for the system scenario, scheduling a small number of users to be simultaneously served by each small BS for a single time.

In the cognitive radio (CR) paradigm, the ESPAR antenna is employed for spatial spectrum sensing in order to utilize the new angle dimension in the spectrum space besides the conventional frequency, time and space dimensions. The two-stage spatial spectrum sensing method is proposed based on the ESPAR antenna being targeted at identifying white spectrum space, including the new angle dimension. At the first stage, the occupancy of a specific frequency band is detected by conventional spectrum-sensing methods, including energy detector and eigenvalue-based methods implemented with the switched-beam ESPAR antenna.

With the presence of primary users, their directions are estimated at the second stage, by high-resolution angle-of-arrival (AoA) estimation algorithms. Specifically, the compressive sensing technology has been studied for AoA detection with the ESPAR antenna, which is demonstrated to provide high-resolution estimation results and even to outperform the reactance-domain multiple signal classification.

Acknowledgements

Contents

List of Figures

List of Tables

Abbreviations

ABF	Aerial Beamforming
AoA	Angle of Arrival
AoD	Angle of Departure
A/D	Analog-to-Digital
AWGN	Additive White Gaussian Noise
BC	Broadcast Channel
BIA	Blind Interference Alignment
BS	Base Station
BP	Basis Pursuit
BPDN	Basis Pursuit De-Noise
CCC	Cross Correlation Coefficient
CD	Coherence Detection
CDF	Cumulative Distribution Function
CR	Cognitive Radio
CS	Compressive Sensing
CSI	Channel State Information
CSIR	Channel State Information at the Receiver
CSIT	Channel State Information at the Transmitter
D/A	Digital-to-Analog
DBF	Digital Beamforming
DC	Direct Current
D/C	Down Convertor
DoF	Degree of Freedom
DPC	Dirty Paper Coding

DSL	Digital Subscriber Line
DSP	Digital Signal Processor
EPs	Estimation Pilots
ESPAR	Electronically Steerable Parasitic Array Radiator/Receptor
ESPRIT	Estimation of Signal Parameters via Rotational Invariance Techniques
FDD	Frequency-Division Duplex
GA	Genetic Algorithm
IF	Intermediate Frequency
LOS	Line-of-Sight
LMS	Least Mean Square
LNA	Low Noise Amplifier
LTE	Long Term Evolution
LZFBF	Linear Zero-Forcing Beamforming
MEMS	micro-electromechanical systems
MIMO	Multiple-Input-Multiple-Output
MISO	Multiple-Input-Single-Output
MSE	Mean Square Error
MUSIC	MUltiple SIginal Classification
MVDR	Minimum Variance Distortionless Response
NEC	Numerical Electromagnetic Code
PA	Power Amplifier
PDF	Probability Density Function
PU	Primary User
QoS	Quality of Service
RD	Reactance-Domain
RF	Radio Frequency
SCNs	Small-Cell Networks
SPA	Switched Parasitic Antenna
SINR	Signal-to-interference-plus-noise Ratio
SNR	Signal-to-noise Ratio
SISO	Single-Input-Single-Output

SU   Secondary User

SVD   Singular Value Decomposition

TDMA   Time Division Multiple Accessing

UCA   Uniform Circular Array

ULA   Uniform Linear Array

UT   User Terminal

Notations and Symbols

Symbol	Description
$(\cdot)^*$	Conjugate operator
$(\cdot)^T$	Transpose operator
$(\cdot)^H$	Conjugate transpose operator
$(\cdot)^{-1}$	Inversion operator
$(\cdot)^\dagger$	Pesudoinverse operator
$diag(\cdot)$	Form a diagonal matrix from a vector argument
$det(\cdot)$	Determinant of a matrix
$\lvert \cdot \rvert$	Amplitude of complex number
$\lVert \cdot \rVert$	l_2-norm/Euclidean Norm
$\lVert \cdot \rVert_0$	l_0-norm
$\lVert \cdot \rVert_1$	l_1-norm
$\lVert \cdot \rVert_{p,q}$	Mixed norm
$\lVert \cdot \rVert_F$	Frobenius norm of a matrix
j	Imaginary unit
$\mathbb{E}\{\cdot\}$	Expectation operator
$\mathbb{C}$	The set of complex numbers
$\mathbb{R}$	The set of real numbers
$Tr\{\cdot\}$	Trace of a matrix
$\mathbb{P}_{\mathcal{L}}(\cdot)$	Projection matrix
$\mathcal{L}$	Feasible set
$\boldsymbol{I}_n$	Identity matrix of size n
$\mathbf{0}_n$	Zero matrix of size n

Chapter 1

Introduction

1.1 Background

Smart multi-antenna systems are key trends for next-generation wireless communication systems, with the potential to increase channel capacity, enhance quality of service (QoS), improve radio frequency (RF) spectrum usage, extend coverage, reduce power consumption and steer transparent operation across multi-technology wireless networks. Much research has given considerable attention to the multi-antenna system for wireless communication applications, especially in the context of signal processing and coding architectures. A multi-antenna system can be exploited in a variety of ways to achieve the specific goal(s).

- *Beamforming:* Multi-antenna systems are generally exploited for beamforming functions, targeted at maximizing the array gain for certain directions of interest, while minimizing power leakage in other directions. The capability of beamforming is the goal of a smart antenna system at the initial development stage. Beamforming involves array signal processing: that is, signals derived from individual antenna elements are properly weighted and summed to produce the output of the array. Various beamforming algorithms have been sufficiently studied in the literature (see [6] and references
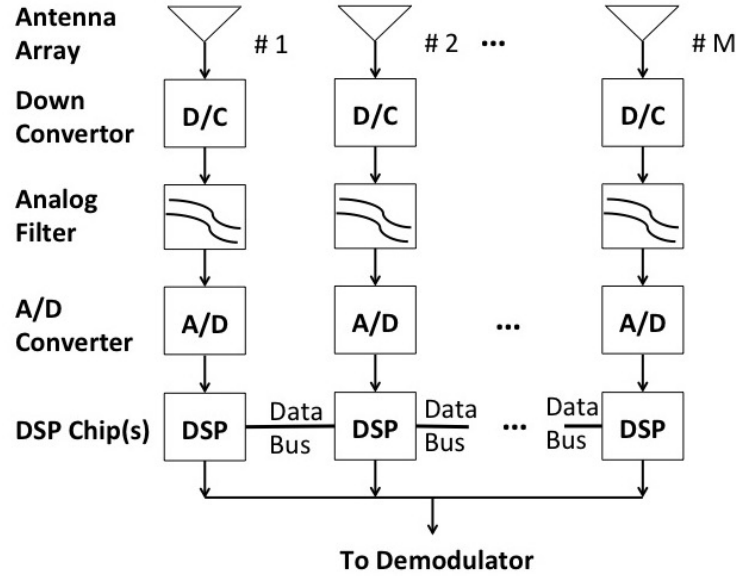
FIGURE 1.1: The block diagram of a DBF receiver [1].

therein), within which desired signal is differentiated from co-channel interference, using either a reference signal or knowledge of the directions of desired signal and interferers. It is noted that these algorithms are mainly designed based on a digital beamforming (DBF) array. The block diagram of a DBF array working in the receiving model is shown as Figure 1.1. The signal received by each element is converted to the baseband by the down converters (D/C) and analog filter. Then the baseband signal is digitized by the analog-to-digital (A/D) converter and passed to the digital signal processor (DSP) sections in which the beamforming algorithms reside.

- *Direction finding:* Direction finding, or angle-of-arrival (AoA) estimation, is an attractive area of research. It has been widely applied in the fields of radar and sonar surveillance, as well as mobile radio communications. For example, knowledge of the AoAs of desired signals and/or interferers plays an important role in a communication system, employing some form of spatial filtering with sectorized directional antennas, switched beam antennas or adaptive antennas. A number of AoA estimation methods have been developed, including conventional beamforming [7], Capon's method [8], subspace-based methods like MUSIC (MUltiple SIgnal Classification) [9] and ESPRIT (Estimation of Signal Parameters via Rotational Invariance)

2

[10] algorithms, and the methods based on the emerging compressive sensing technology [11]. The accuracy of these algorithms is evaluated by AoA estimation and the ability to detect closely spaced signals. It is worth noting that these algorithms are also based on the DBF array using multiple RF chains.

- *Multiple-Input-Multiple-Output (MIMO) technology:* Motivated by the demand for high data rate in wireless networks, MIMO technology has gained significant attention. It has been demonstrated that the channel capacity of the MIMO system (characterized by multiple antennas at both the transmit and receive ends) increases almost linearly with the minimum number of transmit-receive antennas [12–14]. On one hand, multiple antennas are used to increase diversity to overcome multipath fading, where signals carrying the same information are transmitted through independently faded paths to achieve reliable reception. On the other hand, since multiple parallel spatial channels are created between individual transmit-receiver antenna pairs with high probability, independent information streams are transmitted in parallel through spatial channels. As a consequence, degree of freedom (DoF) increases, leading to higher data rate. This effect is called *spatial multiplexing* [15]. It is noted that high capacity is achievable under assumptions of rich scattering and uncorrelated spatial channels.

Conventionally, *multi-antenna systems* refer to the DBF arrays described previously, where multiple active elements are connected to separate RF chains. Signal processing is operated at the baseband stage to achieve intelligence. Although multi-antenna systems have been proved, by theory and experimentation, to have the capabilities to improve the performance of wireless communications, the use of multi-antenna systems, indeed, increases complexity and cost, which has to be considered in establishing a practical system. On the other hand, the ongoing trend in modern wireless terminals is toward miniature, compact and highly integrated devices. Under small size constraints, the employment of multi-antenna systems

is more challenging. The limitations and challenges of multi-antenna systems for compact deployment are summarized as follows:

- *RF hardware complexity and cost:* With regard to the DBF array, one RF chain is composed of the A/D converter, digital-to-analog (D/A) converter, low-noise amplifier (LNA), power amplifier (PA), intermediate frequency (IF)/RF filters, etc. Since in the multi-antenna array an element is connected to a separate RF chain to independently modulate/demodulate signals, it is clear that hardware cost and complexity increase with the number of antenna elements.

- *Circuit power consumption:* In one RF chain, the direct current (DC) power is mainly consumed by the PA, D/A converter, mixer, and active filters in the transmit chain, and by the frequency synthesizer, LNA, A/D converter and active filters in the receive chain [16]. The power consumption increases with the number of antenna elements used in the array. It is rather costly in terms of battery-powered devices.

- *Antenna system efficiency:* Smaller inter-element spacing (usually smaller than a half-wavelength) is needed for compact device applications, which results in strong mutual coupling among antenna elements. Strong mutual coupling affects the input impedance seen by the RF ports, thereby leading to a mismatch loss: that is, some of the incident power is reflected back to the source. In addition, some of the radiated power will be absorbed by the neighboring elements being terminated by a resistive impedance [17]. These two losses account for the matching efficiency. Without delicate design in matching efficiency, the performance of the antenna systems will be significantly reduced.

- *Spatial correlation:* The antenna correlation (or spatial correlation) does impact the MIMO channel capacity. In [18], Tulino et al. studied the relation between the antenna correlation and the capacity of multi-antenna channels and demonstrated that, for separable correlations specifically, receive correlation is always detrimental due to the reduction of effective dimensionality

without increasing captured power; transmit correlation reduces the effective dimensionality of the transmitter with focusing power, thereby achieving an advantage in low SNR region, but it is detrimental in high SNR region. It has been shown that the antenna correlation is a function of antenna spacing, array geometry, and angular energy distribution [19]. With regard to the antenna spacing, the antenna correlation decreases with the increase of antenna spacing, thereby improving channel capacity. This improvement is more significant through enlarging antenna spacing at the transmit antenna than that at the receive antenna [19].

- *Inter-chain interference:* The use of non-ideal RF components will result in leakage among the parallel RF chains, thereby reducing the performance of the system [17].

These limitations related to multi-antenna systems lead to challenges in applications of compact, low-complexity terminals. Parasitic antennas have been proposed as the alternative to multi-antenna systems. In parasitic antennas (see Figure 1.2), only one antenna element is active and fed by the single RF source, and other elements, called *parasitic elements*, are connected to switches, or are short-circuited and loaded by reactance values. It is noted that a parasitic element requires only a simple control circuit instead of an expensive RF chain, thereby reducing hardware cost and circuit power consumption. In addition, a parasitic antenna system employs mutual coupling between active and parasitic elements to achieve beamforming. In this context, the inter-element spacing is desired to be smaller (usually smaller than a half-wavelength), compared to that of a multi-antenna system. Consequently, a parasitic antenna system has smaller volume, suited to a small portable terminal.

The switched parasitic antenna can be traced back to the early work of Yagi and Uda [20, 21], which offers a directional antenna pattern by switching the short-circuits on parasitic elements: the antenna pattern is steered to the open parasitic element while the others are short-circuited. Dinger [22] developed the reactively steerable parasitic array consisting of closely coupled microstrip elements. In the
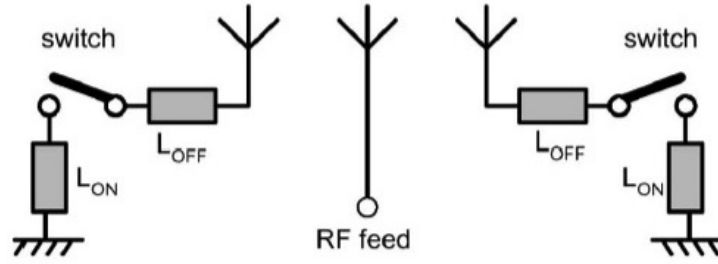
(a) Switched parasitic antenna
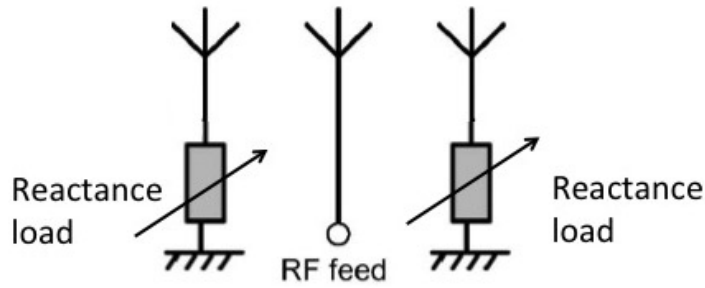
(b) Reactance-assisted parasitic antenna

FIGURE 1.2: Diagram of parasitic antenna configurations.

reactance-assisted parasitic antenna, reactively adjusting reactance loads of parasitic elements, the antenna pattern can be modified. Therefore, the reactance-assisted parasitic antenna is a more efficient and flexible solution to beamforming. In the Advanced Telecommunications Research (ATR) laboratories of Japan, a number of smart parasitic antennas named electronically steerable parasitic array radiator (ESPAR) antennas have been successively developed[23–25], which include several monopoles (one active element surrounded by several parasitic elements) mounted on a ground plane. Parasitic elements are short-circuited and connected to variable reactors (varactors), which control their reactance loads.

This work is motivated by the theoretical gains suggested by exploiting multi-antenna systems, where antenna aspects are combined with the associated signal

processing and other emerging techniques for transparent operation across multi-technology wireless networks. This dissertation addresses the limitations of multi-active antennas under compactness constraints by using the single-RF ESPAR antenna. The beampattern of an ESPAR antenna is controllable by electronically tuning a few easy-to-implement reactance loads of parasitic elements.

To meet the increasing demands for high data rate, multi-user MIMO techniques have attracted significant interest, due to the potential for spectral efficiency. The efficiency, fundamentally, results from an increase in the number of DoFs for transmission use. In particular, the achievable DoFs in a single-user MIMO system are known up to $\min(N_t, N_r)$, where N_t and N_r are numbers of transmit and receive antennas, respectively [13]. In order to increase the DoFs without increasing N_r or complexity at the user, a multi-user MIMO system is introduced, and it is demonstrated that the achievable DoFs are up to $\min(N_t, KN_r)$, where K is the number of users [26]. Generally, perfect knowledge of the channel state information (CSI) between the transmitter and receiver is required to achieve such DoFs, by using linear zero-forced beamforming (LZFBF), dirty-paper-coding (DPC), interference alignment, etc. However, in practical systems, acquiring the CSI at the transmitter is a challenging task and also leads to signaling overheads. To this end, a novel technique termed *Blind Interference Alignment* (BIA) [27] has been developed for the multi-user multiple-input-single-output (MISO) broadcast channel (BC) to achieve an optimal DoF without requirement for the CSI at the transmitter. The key to BIA is the use of a reconfigurable antenna at the receiving end to perform antenna mode switching. Motivated by this, in this thesis, we will employ the ESPAR as a solution to beampattern switching for practical implementation of BIA.

Small cell networks (SCNs) (e.g., picocells and femtocells) represent the other emerging technique introduced to improve system capacity, coverage and energy efficiency, while offloading traffic from expensive macrocellular networks [28]. The small cells are low-cost, low-power, user-deployed base stations (BSs), underlying the existing macrocells. They are designed with auto-configuration and self-optimization capabilities, and they leverage users' broadband internet connect as

the backhaul. However, to achieve the capacity expected by using small cells, co-channel deployment of dense small cells within the macrocell is essential, which leads to enormous inter-cell interference. Therefore, interference management becomes one of the technical challenges with SCNs. Generally, in the small cells, the traditional single omni-directional antenna is deployed at both the small BSs and user terminals, due to the size constraint. In this context, interference is generally mitigated by power control [29, 30] and resource allocation [31, 32], which could result in significantly increased system complexity due to the needs of message exchange and/or cooperation across femtocells. To achieve inter-cell interference mitigation while keeping the complexity and cost to a minimum, the smart antenna has been considered as a solution. Under the compact constraints, the ES-PAR antenna provides a solution to interference suppression with the capability of adaptive beamforming.

The concept of cognitive radio (CR) has been introduced to identify underutilized spectrum and allow secondary users (SUs) to opportunistically utilize the licensed spectrum without causing unacceptable interference for the primary users (PUs) [33]. When the interweave paradigm (where SUs exploit knowledge of the PU's activity in the spectrum to identify transmission opportunity [34]) is considered, spectrum sensing is the most important component of establishing the CR systems. Moreover, a new angle dimension can be introduced in the spectrum space for further efficient spectrum usage. In this sense, the spectrum sensing is referred to as *spatial spectrum sensing*, where the direction of primary signal should be detected. The smart antenna systems play an important role in the CR system, since they are exploited to perform and improve the spectrum sensing function, and they also offer beamforming capabilities, that is, the SU equipped with a smart antenna is able to steer the beam to the direction without causing harmful interference to the PU (i.e., the angle dimension) [35]. However, these benefits are not attractive in small CR terminals. A major area of study in this thesis is thus the *spatial spectrum sensing* for compact CR terminals.

1.2   Thesis Outline

Chapter 2: In this chapter, we first describe the single-radio parasitic antenna system – electronically steerable parasitic array radiator (ESPAR), which is the foundation of this thesis studied as a solution for compact transceivers applications, since the parasitic elements require no extra RF hardware. The ESPAR antenna systems are tractably modeling as the active element response and current vector controlled by parasitic ports. Particularly, in the ESPAR antenna, parasitic elements are terminated with variable reactors (varactors) that can continually tuning reactance values loaded to them. The parasitic elements are strongly coupled with the sole active element, due to smaller inter-element spacing. Therefore, the ESPAR antenna is able to adjust the beampattern by tuning reactance loads of parasitic elements. To achieve adaptive beamforming in the ESPAR antenna, the fast convergent algorithm is required. However, the unique configuration of the ESPAR imposes difficulty to apply sophisticated adaptive algorithms derived for the conventional DBF array. Based on the ESPAR antenna, the minimum variance distortionless response (MDVR) algorithm is modified, where we first processes array signals in the reactance domain, then reformulate the MVDR algorithm as a convex problem, and finally optimize necessary reactance loads by iterating the convex problem and a simple projector. Beside this method, the adaptive beamforming based on the genetic algorithm is also studied for an ESPAR antenna, exploiting the reference signal or desired beampattern.

Chapter 3: For the downlink of a multi-user MISO broadcast channel, blind interference alignment (BIA) [27] is a promising technique to achieve an optimal DoF without knowledge of channel state information at the transmitter (CSIT). BIA uses antenna mode switching (e.g., frequency, polarization and beampattern) at the receiving end to create channel fluctuation patterns in combination with a space-time coding structure at the transmitter to align inter-user interference. The subject of this chapter is the application of the ESPAR antenna in small user terminals for the implementation of BIA. Its capability of beamforming, by simply tuning a few easy-to-implement reactance loads, is exploited as the solution

to antenna mode switching for BIA, since frequency switching will increase the necessary frequency band, and polarization switching may be only suitable for communication systems insensitive to transmitter and receiver orientations (e.g., satellites). Furthermore, the ESPAR's beampattern can be designed to improve receive signal-to-noise ratio (SNR), thereby improving the performance of BIA, which is subject to high SNR requirements due to noise amplification. In particular, we propose three beamforming methods – random beamforming, sector beampattern selection and singular value decomposition (SVD) based beamforming – to provide the required number of different beampatterns across one *Super Symbol* for the implementation of BIA.

Chapter 4: Small cell networks provide a promising solution to increase system capacity and improve indoor coverage. However, inter-cell interference becomes enormous among small cells due to dense deployment and cell-size reduction. This part focuses on interference mitigation methods in the residential femtocells, by exploiting the ESPAR antenna. We first consider the system scenario: each femto-BS serves one user for a single time. In this scenario, the ESPAR is deployed at both the femto-BS and user terminal, and ESPAR's analog beamforming is used to mitigate inter-cell interference through increasing the signal-to-interference-plus-noise ratio (SINR). This method has low complexity compared to other methods including the resource allocation and power control methods. Then, we consider the system scenario: each femto-BS simultaneously serves a few number of users for a single time. The ESPAR-based BIA scheme is studied as the solution to mitigating both the intra-cell and inter-cell interference.

Chapter 5: Focusing on the interweave mode, spectrum sensing is essential to build the CR system. This part of the thesis deals with the *spatial spectrum sensing* problem with the signal-RF parasitic antennas equipped at the compact cognitive radios. As the directional antenna is assumed to be adopted in the CR, besides exploiting the conventional three dimensions in the spectrum space (i.e., the specific frequency subband at a certain time in a given geometry region), the new angle dimension is available to be exploited. Therefore, in this CR system, not only should the occupancy of a specific frequency subband be detected at a

particular time in a given region, but also the directions of the existing primary signals are required to be estimated. In this context, the two-stage *spatial spectrum sensing* method is considered. At the first stage, the *temporal spectrum sensing* methods are studied for the ESPAR antenna to identify the PU's activity in the three-dimension spectrum space. Once the decision has been made at the first stage that primary users are present, at stage two, the CR receiver has to estimate directions of present primary signals by using a high-resolution AoA estimation method, e.g., the reactance-domain (RD) MUSIC algorithm. The problem of the RD-MUSIC algorithm is its requirement for large number of samples and it is applicable for uncorrelated signals. In relation to this problem, compressive sensing is studied for the AoA estimation problem with the ESPAR antenna.

Chapter 6: The last chapter summarizes the work of the thesis, and we also suggest some further work that may be useful for extending the work of the thesis.

1.3 Publications

Throughout the PhD study, the following scientific papers have been published in the forms of conference papers and journal articles:

1.3.1 Conference Proceedings

R. Qian, M. Sellathurai, D. Wilcox, "On the design of blind interference alignment using ESPAR antenna", *In Proc. IEEE International Conference on Communications and Networking in China (CHINACOM),* pages 886 – 870, 2012.

R. Qian, M. Sellathurai, "Performance of the blind interference alignment using ESPAR antennas", *In Proc. IEEE International Conference on Communications (ICC),* pages 4885 – 4889, 2013.

R. Qian, M. Sellathurai, " Design of ESPAR based blind interference alignment for cellular systems", *In Proc. Wireless Communications and Networking Conference (WCNC)*, pages 3083 – 3087, 2013.

R. Qian, M. Sellathurai, T. Ratnarajah,"Directional spectrum sensing for cognitive radio using ESPAR arrays with a single RF chain", *In Proc. IEEE European Conference on Networks and Communications (EuCNC)*, pages 1 – 5, 2014.

R. Qian, M. Sellathurai, D. Wilcox, "A study on MVDR beamforming applied to an ESPAR antenna", *In Proc. Interference Conference on Acoustics, Speech and Signal Processing (ICASSP)*, April, 2015, Brisbane.

R. Qian, M. Sellathurai."Interference mitigation in femtocell networks using single-radio parasitic antennas", *In Proc. IEEE International Conference on Communications (ICC)*, June, 2015, London.

R. Qian, M. Sellathurai, J. Chambers, "Direction-of-arrival estimation with single-RF ESPAR antennas via sparse signal reconstruction", *IEEE International Workshop on Signal Processing Advances in Wireless Communications (SPAWC)*, June 2015, Stockholm. (Submitted)

1.3.2 Journal Articles

R. Qian, M. Sellathurai, D. Wilcox, "A study on MVDR beamforming applied to an ESPAR antenna", *IEEE Signal Processing Letters*, 2015, 22(1): 67-70.

R. Qian, M. Sellathurai, "On the implementation of blind interference alignment with single-radio parasitic antennas", *IEEE Transaction Vehicular Technology*, 2015.(Submitted)

The novelties in these publications are summarized as follows. A fast convergence beamforming algorithm based on MVDR is proposed for the ESPAR antenna. The unique configuration (single-active element) and the non-linear relationship between the beampattern and reactance loads impose difficulty in adaptive beamforming in the EAPR array. To address these problems, we exploit the convexity

of the sub-optimal problem – optimization of the equivalent weight vector, and introduce a simple projector for feasible reactance loads. Finally, the MVDR beamforming is modified as an iterative algorithm for the ESAPR antenna. The BIA [27] is a promising multi-user MISO BC technique, which provides an optimal DoF without requirements of knowledge of CSIT, where the key is the antenna mode switching at the receiving end. However, in most of the literature on BIA, authors simply assume the i.i.d channels as channel coefficients associated with different antenna modes. Thus, the results are given in the theoretic perspective. In this work, the first attempt to employing a realistic beamforming scheme (ESPAR) for the implementation of BIA is studied. Moreover, the ESPAR beam-pattern is also designed to further improve the performance of BIA. In the small cell networks, interference is one of the technique challenges. To mitigate interference while maintaining minimum system cost, the smart antenna is a practical solution. The ESPAR antenna is suitable to be applied by small modern wireless terminals including the home base stations and the user terminals. Thus, the ES-PAR antenna is first studied as an interference mitigation solution for femtocells, where its capability of beamforming is used. In the CR system, with the development of smart antenna technology, a new angle dimension can be introduced to further efficient usage of spectrum resources. In this context, the *spatial spectrum sensing* is considered based on the EPSAR antenna, where the high resolution AoA estimation method is included. To improve the AoA estimation performance of an ESPAR with reduced sampling numbers, the compressive sensing is first considered for a single-RF antenna array. The sparse signal is represented in terms of an overcomplete dictionary composed of samples from array manifold. In order to create spatial diversity for the signal-RF ESPAR antenna, we introduce a projection matrix, which is designed to divide the whole angle space of the receiver into sectors. Thus, the use of the projection matrix enables that the sparse signals are projected to beamspace measurements, by full scanning the whole angle space. The AoA estimation problem is thus cast to the sparse representation problem, where the sparse spectrum can be efficiently reconstructed by algorithms, e.g, l_1-SVD.

Chapter 2

Single-Radio Parasitic Antennas and Adaptive Beamforming

The single-radio electronically steerable parasitic array radiator (ESPAR) antenna is exploited in our work in order to address the limitations related to the use of multi-active antenna systems under compact constraints. This chapter presents the basic modelling of the ESPAR antenna system and deals with the adaptive beamforming algorithms. In Section 2.1, we present working principles and the modelling of an ESPAR antenna. An essential function of the ESPAR antenna system is beamforming, which is achieved by tuning a small number of reactance loads connected to parasitic elements. However, there is a non-linear relationship between the beampattern and reactance loads. In addition, the reactance loads are generally required to be pure imaginary values. These characteristics impose difficulties for the adaptive beamforming of an ESPAR antenna. To this end, a fast adaptive beamforming method based on a conventional MVDR beamformer is proposed in Section 2.3. We also present a beamforming method by using genetic algorithms. In addition, due to the symmetric geometry of the array, an ESPAR antenna is able to perform as a switched-beam antenna in order to switch between a fixed number of pre-designed sector beampatterns.

2.1 Electronically Steerable Parasitic Array Radiator

In 2000, Ohira et al. were the first to develop a smart antenna system, named the ESPAR, as an alternative solution for adaptive beamforming [23, 24]. The ESPAR antenna uses only a single active antenna and several parasitic elements. The sole active element is fed by an RF source, while parasitic elements are terminated with tunable reactance loads, rather than being connected to RF chains. The ESPAR antenna is a smart antenna system with a significant advantage over its counterpart (the multi-active antenna system), in that it is able to adaptively control its beampatterns, as does any smart antenna system, while using a single active element and a small number of parasitic elements.

Consider an ESPAR array consisting of $M+1$ thin electrical dipoles with a length of a half of the carrier wavelength, as shown in Figure 2.1. A single active element (# 0) is placed at the center of the circle, and it is surrounded by M parasitic elements sited at equal angular separations on the circle: i.e., the m-th parasitic element is located at the relative angle $\phi_m = (m-1)\frac{2\pi}{M}, m \in \{1, \cdots, M\}$. It is noted that an ESPAR antenna developed by Ohira et al. [23, 24] is designed as a circular array. This symmetrical antenna structure simplifies the analysis of the ESPAR antenna (especially the mutual coupling between array elements); moreover, this structure also enables the ESPAR antenna to work as a switched-beam antenna by simply shifting designed reactance loads of parasitic elements. By now, most of the literature focuses on the study of the circular ESPAR antenna. Other shapes (e.g., rectangular or linear) of parasitic arrays have been studied in the multi-active-multi-parasitic arrays [36].

The spacing between the active element and the parasitic element is d, which is usually smaller than a half of the carrier wavelength ($d < \lambda/2$, where λ is the wavelength). The active element is connected to a radio transceiver which has the load impedance Z_s: that is, the input impedance of the LNA. M parasitic elements are

loaded with reactance loads denoted by a vector $\hat{\boldsymbol{x}} = [x_1, \cdots, x_m, \cdots, x_M]$. Generally, a small inter-cell spacing is undesirable in a multi-active antenna. However, smaller inter-element spacing is required in the ESPAR array in order to achieve strong mutual coupling. Due to this strong mutual coupling, currents can be induced on the parasitic elements when the active element is fed by the RF source. In this context, adjusting reactance values results in changes to the currents of all elements and, consequently, the radiation pattern [37]. When a parasitic element is loaded with an inductive load (positive reactance), it performs as a director, radiating away from the active element. By contrast, when a parasitic element is loaded with a capacitive load (negative reactance), it performs as a reflector, radiating towards the active element.
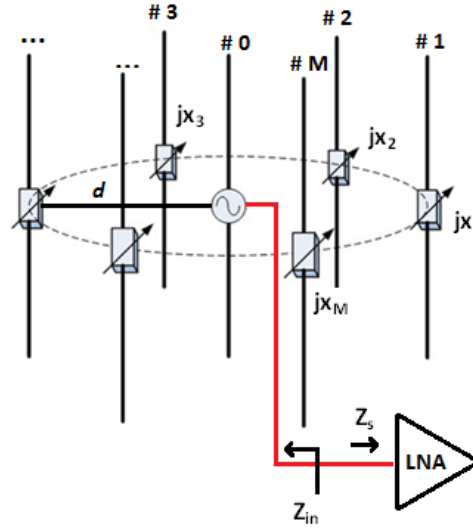
FIGURE 2.1: Structure example of an $(M + 1)$-element ESPAR.

The reactance loads (jx_m) are achieved by using a simple control circuit as shown in Figure 2.2, which includes a varactor diode (or an arrangement of varactor diodes) and two fixed inductors in series and parallel [38]. By imposing a DC voltage to the varactor, it exhibits a junction capacitance (i.e., reactance loads). If the voltage is then continuously adjusted, the capacitance changes according to the voltage. Here, the two fixed inductors are used to effectively provide a wide range reactance, since the variable capacitance range of a varactor is narrow [39]. Based on the varactor catalog data, the relationship between the digital control
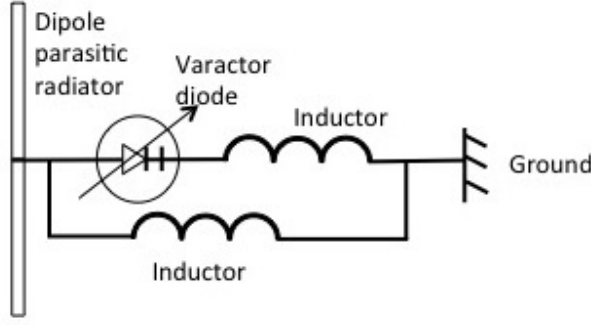
FIGURE 2.2: Control circuit of a parasitic element.

voltage to vatacor $v_{cc,m}$ and the reactance $x_m(m = 1, \cdots, M)$ has a linear equation [40]

$$x_m = -0.0217v_{cc,m} - 49.21.$$

Due to the above linear relation, we can always find a DC voltage for a required reactance load. Therefore, in this work, we simply consider the reactance loads as the variables of the beampattern of an ESPAR antenna.

Now, we start representing modeling of an ESPAR antenna, specifically, the beam-pattern expression of the ESPAR antenna. We first suppose that the ESPAR antenna is working as a transmitter. Signals transmitted at the single RF port excite parasitic elements with induced currents. Current and voltage vectors of the ESPAR array are respectively written as

$$\boldsymbol{i} = \begin{bmatrix} i_0 & i_1 & \cdots & i_M \end{bmatrix}^T,$$

and

$$\boldsymbol{v} = \begin{bmatrix} v_0 & v_1 & \cdots & v_M \end{bmatrix}^T.$$

Let the $(M+1)$-by-$(M+1)$ matrix $\boldsymbol{Z}$ represent mutual impedances between array elements. Due to the symmetric antenna structure, the entries of $\boldsymbol{Z}$ have the relation $Z_{i,j} = Z_{j,i}$ [40]. The values of mutual impedances are determined by the antenna configuration (i.e., the size and location of each array element). The values can be calculated by the analytical formulas given in [41] or the Numerical

Electromagnetic Code (NEC) [21]. The analytical formulas suited to dipoles are given in Appendix A. The relation between induced currents and voltages on elements of the ESPAR array is represented using an equivalent mutual impedance matrix model, of the following form

$$\boldsymbol{v} = \boldsymbol{Z}\boldsymbol{i}. \tag{2.1}$$

Assume that the driving RF port transmits signal voltage v_s (with amplitude and phase) at the active element. Thus, the excited voltages on the active element and the parasitic elements are represented as

$$v_0 = v_s - Z_s i_0, \tag{2.2a}$$

$$v_m = -jx_m i_m, m \in \{1, \cdots, M\}. \tag{2.2b}$$

Define a diagonal loading matrix as

$$\boldsymbol{X} = diag([Z_s, j\hat{\boldsymbol{x}}]). \tag{2.3}$$

Let a $(M+1)$-dimensional vector $\boldsymbol{u}_0 = [1, 0, \cdots, 0]^T$ be a selection vector. Then (2.2) can be rewritten in the vector version as

$$\boldsymbol{v} = v_s\boldsymbol{u}_0 - \boldsymbol{X}\boldsymbol{i}. \tag{2.4}$$

Combine (2.1) and (2.4), then one has

$$\boldsymbol{Z}\boldsymbol{i} = v_s\boldsymbol{u}_0 - \boldsymbol{X}\boldsymbol{i}. \tag{2.5}$$

After a simple mathematical manipulation, we can obtain an expression of the current vector as a function of reactance loads:

$$\boldsymbol{i} = v_s(\boldsymbol{Z} + \boldsymbol{X})^{-1}\boldsymbol{u}_0 = v_s\boldsymbol{w}, \tag{2.6}$$

where $\boldsymbol{w} = (\boldsymbol{Z}+\boldsymbol{X})^{-1}\boldsymbol{u}_0$ is the equivalent weight vector, since it plays a role similar

to that of the weight vector in conventional adaptive arrays. The far-field radiation pattern is a superposition of current signals on all elements in an antenna array [42]. Throughout this work, we focus on the analysis of the 2-dimensional plane through the antenna plane, such that the directions of signals may be described by the azimuth angle θ. Consequently, the beampattern of the ESPAR array is given as

$$B(\theta) = \boldsymbol{i}^T \boldsymbol{a}(\theta), \tag{2.7}$$

where $\boldsymbol{a}(\theta)$ is the steering vector defined by the array geometry, of the form

$$\boldsymbol{a}(\theta) = \begin{bmatrix} 1 & e^{-j\frac{2\pi d}{\lambda}\cos(\theta - \phi_1)} & \cdots & e^{-j\frac{2\pi d}{\lambda}\cos(\theta - \phi_M)} \end{bmatrix}^T. \tag{2.8}$$

From (2.6) and (2.7), we observe that the beampattern expression is a function of reactance loads at parasitic elements ($x_m, m \in \{1, \cdots, M\}$).

The beampattern expression in (2.7) is derived under the assumption that the ESPAR antenna works as a transmitter. According to the theorem of reciprocity (the radiation pattern of an antenna in the transmit-mode is the same as that in the receive-mode), formulation (2.7) is also available for an ESPAR antenna working as a receiver; however, in the receive-mode, the current vector $\boldsymbol{i}$ should be replaced by the equivalent weight vector $\boldsymbol{w}$ [43], i.e., $B(\theta) = \boldsymbol{w}^T \boldsymbol{a}(\theta)$.

In an ESPAR array, mismatching between the RF port impedance Z_s and the input impedance (Z_{in}) seen by the active element, determines the efficiency of the antenna system. The input impedance and related efficiency can be respectively calculated as [44, 45]

$$Z_{in} = \frac{1}{i_0} \boldsymbol{u}_0^T \boldsymbol{Z} \boldsymbol{i}, \tag{2.9}$$

$$\eta = 1 - \left[\frac{Z_{in} - Z_s^*}{Z_{in} + Z_s} \right]. \tag{2.10}$$

2.2 Adaptive Beamforming Algorithms

2.2.1 Overview

One important application of a smart antenna system is co-channel interference cancellation on the premise that the desired signal and interferences arrive from different directions. This involves adaptively designing a beampattern steering to the desired direction, while placing nulls in the directions of interference. Many researchers have proposed sophisticated beamforming algorithms based on the DBF array [6]. In DBF arrays, signals impinging on individual elements are sampled and stored; then, the optimal output of the beamformer is the sum of appropriately weighted signals derived from individual elements. The weight coefficient in each element branch is independently controlled. The beamformer diagram of a DBF array is shown in Figure 2.3. Widrow et al. [46] proposed the least mean square (LMS) algorithm based upon the steepest descent method. The minimum square error (MSE) algorithm is proposed to obtain the optimized weights by solving the Wiener filtering problem [6]. Capon [8] developed the MVDR beamformer by exploiting the second-order statistics of array outputs, which usually provides an improvement in the output SINR. However, in the DBF array each RF chain has a low noise amplifier, filter, analog-to-digital converter, etc., prior to the beamformer, so that power consumption and fabrication cost are increased with the number of active elements. This causes difficulties with the application of DBF arrays in small wireless modern terminals.

Nevertheless, the above-mentioned adaptive beamformers are not available for ESPAR antenna applications. As described in the previous section, the working principle of the ESPAR is based upon electromagnetic coupling among elements, and the beampattern is reactively controlled by tuning reactance loads of parasitic elements. In this context, an ESPAR antenna belongs to the aerial beamforming (ABF) array, in which signal combining is operated in space rather than in circuits [39]. The beamformer diagram of the EPSAR antenna is shown as Figure 2.4. Overall, new adaptive beamforming algorithms for the ESPAR antenna should
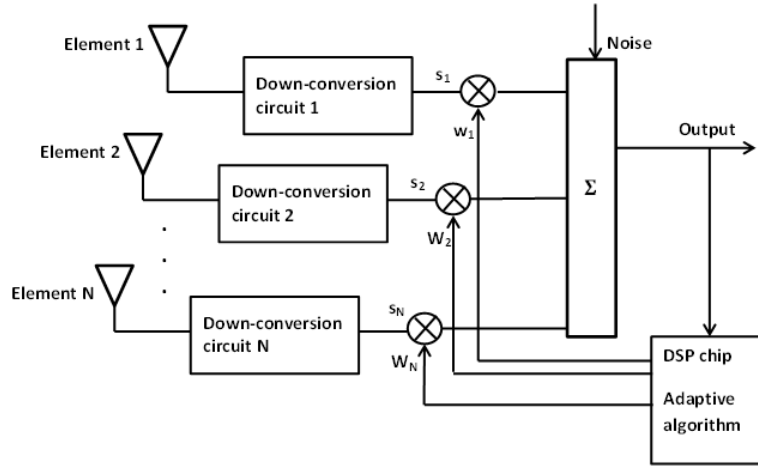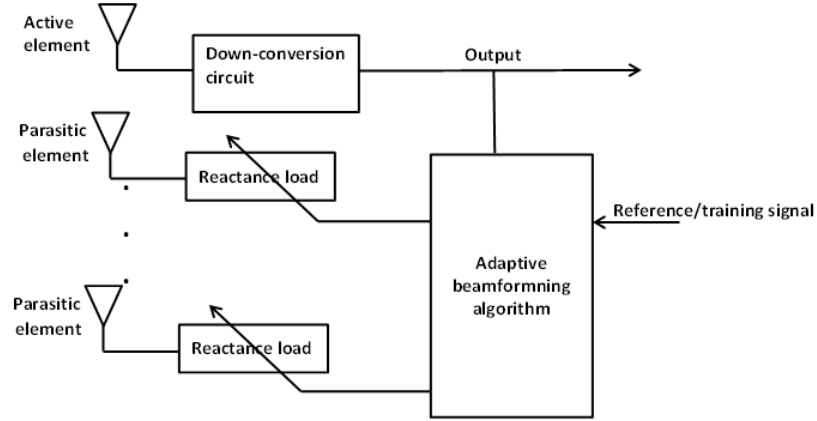
- To the best of our knowledge, there is no closed-form solution that returns reactance loading with pure imaginary components (i.e., zero real components).

Early on in the research, beampattern design for the ESPAR antenna is achieved through exhaustive search of parasitic reactance loadings at the design stage. For example, in the study of employment of the ESPAR antenna to build the beamspace-MIMO transmitter [47, 48], where signals are mapped onto orthogonal basis patterns, the desired transmitted beampattern (i.e., a linear combination of basis patterns weighted by signals) is obtained by exhaustive search of reactance loads. However, this method is only suitable at the design stage, rather than for real-time applications. In order to achieve an efficient adaptive beamforming solution for real-time applications, fast beampattern design strategies have to be developed for the ESPAR antenna. Cheng et al. [49] propose an adaptive beamforming for ESPAR antenna by sequentially perturbed values of reactance loadings based on the steepest gradient theory. In [40, 50], the authors propose stochastic based algorithms, where the objective function is the maximization of the cross-correlation coefficient (CCC) between the reference signal (or the desired beampattern) and the received signal (or the achievable beampattern). However, disadvantages of these beamforming methods are that they easily become trapped in the local minima/maxima with a poor initial guess, and require a large number of iterations. The genetic algorithm (GA) is another option to calculate necessary parasitic reactance loads for a desired beampattern [51, 52]. The benefits of the GA-based method are that it avoids becoming trapped in the local minima/maxima and the requirement of gradient calculation; however, this is a slow-convergence method. Wilcox et al. [45] developed a fast convergence beampattern design strategy that iterates between a convex problem and a simple projection of parasitic reactance loads, using knowledge of directions of desired signals as well as interferers.

2.2.2 Reactance-Domain Technique

Here, we first describe a signal processing method that is generally used in the single-radio antenna array. It is known that, in array signal processing, the correlation matrix of received signal is commonly exploited to perform adaptive beamforming and AoA estimation. In the DBF array, the correlated matrix is obtained by measuring signals induced on individual elements. For the ESPAR antenna, the problem is how to obtain a correlation matrix using a single output port.

To address this problem, the reactance-domain (RD) technique [43, 53, 54] is introduced to obtain a correlation matrix for the EPSAR antenna. Indeed, this technique is similar to the beamspace signal processing in multi-active antenna arrays [6]. The foundation of the RD technique is the feature that an $(M + 1)$-element ESPAR antenna possesses M variable reactances. We first use a set of reactance values and then obtain a measurement from the single output. We can always change the loaded reactance values and then obtain different measurements from the single output port with the same transmitted signal. Therefore, the obtained measurements are correlated across the different sets of reactance values.

We consider the propagation environment with the line-of-sight (LOS) path, ignoring the multipath components. Assume that there are P far-field narrowband signals impinging on the ESPAR array. Let $r_m(t), m = 1, \cdots, M + 1$ denote the response of the m-th element of the antenna to incident signals, and let $\boldsymbol{r}(t) \in \mathbb{C}^{(M+1)\times 1}$ be the column vector of the array response. Accordingly, the column vector $\boldsymbol{r}(t)$ is expressed as [46]

$$\boldsymbol{r}(t) = \sum_{p=1}^{P} \boldsymbol{a}(\theta_p)s_p(t) + z(t), \tag{2.11}$$

where $s_p(t)$ is the p-th signal from the AoA $\theta_p, p \in \{1, \cdots, P\}$, and $z(t) \sim \mathcal{CN}(0, \sigma_z^2)$ is the additive noise with random variables of zero-mean and variance σ_z^2.

Since the outputs of parasitic elements cannot be observed, instead they are electronically combined with each other and the active element. According to (2.7), the output of the ESPAR array is collected from the single active port, taking the following form

$$
\begin{aligned}
y(t) &= \boldsymbol{w}^T \boldsymbol{r}(t) + z(t) \\
&= \sum_{p=1}^{P} \boldsymbol{w}^T \boldsymbol{a}(\theta_p) s_p(t) + z(t) \\
&= \boldsymbol{w}^T \underbrace{\begin{bmatrix} \boldsymbol{a}(\theta_1) & \cdots & \boldsymbol{a}(\theta_P) \end{bmatrix}}_{\boldsymbol{A}} \begin{bmatrix} s_1(t) \\ \vdots \\ s_P(t) \end{bmatrix} + z(t).
\end{aligned}
\tag{2.12}
$$

Consider that N sets of reactance loads $\hat{\boldsymbol{x}}_1, \cdots, \hat{\boldsymbol{x}}_N$ (thus N beampatterns defined by $\boldsymbol{w}_1, \cdots, \boldsymbol{w}_N$) are used in the RD technique. Thus, one obtains measurements $y_1(t_1), \cdots, y_N(t_N)$, expressed as

$$
\begin{aligned}
y_1(t_1) &= \sum_{p=1}^{P} \boldsymbol{w}_1^T \boldsymbol{a}(\theta_p) s_p(t_1) + z(t_1) \\
&\vdots \\
y_N(t_N) &= \sum_{p=1}^{P} \boldsymbol{w}_N^T \boldsymbol{a}(\theta_p) s_p(t_N) + z(t_N).
\end{aligned}
\tag{2.13}
$$

There is a condition on the source signals in the RD technique that, during the sampling time, the impinging signals are required to be constant: i.e., $s_p(t_1) = s_p(t_2) = \cdots = s_p(t_N), \forall p$. It is clear that, if this condition does not hold, the obtained signals are not correlated across the N different sets of reactance loads.

In general, there two methods to implement the RD technique. In [43], the RD technique is implemented by transmitting the same information data as many times as the number of different reactance sets used. In this case, time indices $t_1, \cdots, t_N$ in (2.13) represent N sampling periods. The problem of such a repeating transmission method is that it decreases the transmission rate. However, it is still feasible in applications such as terminal localization or a handheld direction

finder [53]. Another method to implement the RD technique is oversampling signals with a proper rate over N directional beampatterns: that is, the ESPAR antenna fast switches N beampatterns during a sampling period. In this case, time indices $t_1, \cdots, t_N$ in (2.13) represent the sub-periods of a sampling time. However, unlike oversampling applied in digital communications, this oversampling technique should be considered as spatio-temporal oversampling. More work is needed to clarify the implementation of the RD technique based on oversampling strategy. For example, the SNR penalty resulting from oversampling, due to the noise, should be considered [55]. Therefore, unless otherwise indicated, we adopt the repeating transmission method in the RD technique.

With the constant signal condition, we have the N-dimensional output vector $\boldsymbol{y}$, expressed as follows (the time index is dropped to simplify discussion):

$$
\boldsymbol{y} = \begin{bmatrix} y_1 \\ \vdots \\ y_N \end{bmatrix} = \begin{bmatrix} \boldsymbol{w}_1^T \\ \vdots \\ \boldsymbol{w}_N^T \end{bmatrix} \begin{bmatrix} \boldsymbol{a}(\theta_1) & \cdots & \boldsymbol{a}(\theta_P) \end{bmatrix} \begin{bmatrix} s_1 \\ \vdots \\ s_P \end{bmatrix} + \begin{bmatrix} z_1 \\ \vdots \\ z_N \end{bmatrix}
$$
$$
= \boldsymbol{W}^T \boldsymbol{A} \boldsymbol{s} + \boldsymbol{z},
$$

(2.14)

where $\boldsymbol{W}^T = [\boldsymbol{w}_1, \cdots, \boldsymbol{w}_N]^T$ is called the *RF equivalent weight matrix* or *RD weight matrix*.

Let us denote $\boldsymbol{a}_{rd}(\theta) = \boldsymbol{W}^T \boldsymbol{a}(\theta)$ as the modified steering vector in the reactance domain. Thus, (2.14) can be rewritten as

$$
\boldsymbol{y} = \underbrace{\begin{bmatrix} \boldsymbol{a}_{rd}(\theta_1) & \cdots & \boldsymbol{a}_{rd}(\theta_P) \end{bmatrix}}_{\boldsymbol{A}_{rd}} \boldsymbol{s} + \boldsymbol{z}.
$$

(2.15)

The obtained measurements are similar to the signals sampled from individual elements in the conventional DBF array.

Assuming that noises are not correlated across beampatterns and are also not correlated to source signals, the correlation matrix, obtained by the RD technique

with the single-port ESPAR array, is expressed by

$$\boldsymbol{R}_{yy} = \mathbb{E}\{\boldsymbol{y}\boldsymbol{y}^H\}. \tag{2.16}$$

2.2.3 MVDR Beamforming

In this part, we develop the MVDR beamforming algorithm (also known as Capon's beamforming) [8] for the ESPAR antenna. MVDR beamforming is widely used in the DBF arrays, and is designed to minimize the power from interference while maintaining the desired gain at the direction of interest. The direction of interest is known.

1) MVDR for DBF Arrays

Consider a DBF array with N elements (e.g., a ULA or a uniform circular array (UCA)). Suppose that there are P incident signals $s_p(t)$ from AoAs $\theta_p, p \in \{1, \cdots, P\}$. Thus, outputs of the array are denoted by an N-dimensional vector $\boldsymbol{y}_{dbf}(t)$, represented as

$$\boldsymbol{y}_{dbf}(t) = \underbrace{\begin{bmatrix} \boldsymbol{a}(\theta_1) & \cdots & \boldsymbol{a}(\theta_P) \end{bmatrix}}_{\boldsymbol{A}} \boldsymbol{s}(t) + \boldsymbol{z}(t), \tag{2.17}$$

where $\boldsymbol{a}(\theta)$ is the array geometry defined steering vector, and $\boldsymbol{z}(t) \in \mathbb{C}^{N \times 1}$ are noises corrupted on elements.

The output of a beamformer is the sum of properly weighted outputs of elements. Mathematically, this is

$$\tilde{y}(t) = \tilde{\boldsymbol{v}}^H \boldsymbol{y}_{dbf}(t), \tag{2.18}$$

where $\tilde{\boldsymbol{v}} \in \mathbb{C}^{N \times 1}$ is the weight vector of the beamformer.

In the MVDR algorithm, the weights $\tilde{\boldsymbol{v}}$ are optimized by minimizing the power from interference under the constraint of maintaining the distortionless response to the direction of interest. Let $\boldsymbol{R} = \mathbb{E}\{\boldsymbol{y}_{dbf}(t)\boldsymbol{y}_{dbf}^H(t)\}$ denote the correlation matrix of the array outputs. The optimization problem is formulated as the following

linearly constrained quadratic problem [8]

$$
\begin{aligned}
\min_{\tilde{\boldsymbol{v}}} \quad & \tilde{\boldsymbol{v}}^H \boldsymbol{R} \tilde{\boldsymbol{v}}, \\
s.t. \quad & \tilde{\boldsymbol{v}}^H \boldsymbol{a}(\theta_d) = 1,
\end{aligned}
\tag{2.19}
$$

where θ_d is the desired direction. The closed-form solution to (2.18) is [8]

$$
\tilde{\boldsymbol{v}}_{mv} = \frac{\boldsymbol{R}^{-1} \boldsymbol{a}(\theta_d)}{\boldsymbol{a}^H(\theta_d) \boldsymbol{R}^{-1} \boldsymbol{a}(\theta_d)}.
\tag{2.20}
$$

2) MVDR for ESPAR Arrays

However, the MVDR beamforming algorithm described above cannot be directly applied to the ESPAR array, as we mentioned previously. First, we need to generate the spatial correlation matrix by the ESPAR array. This can be done by the RD technique presented in the last section. Specifically, we use N sets of reactance loads $\{\hat{\boldsymbol{x}}_1, \cdots, \hat{\boldsymbol{x}}_N\}$ in the RD technique. Thus, we obtain an N-dimensional measurement vector $\boldsymbol{y}$, given in (2.15).

In practice, we have only finite duration of sensing time to obtain measurements to feed back for weight adjusting. Therefore, we use estimate correlated matrix $\hat{\boldsymbol{R}}$ to replace the ideal correlated matrix $\boldsymbol{R}$. We collect L N-dimensional measurement vectors $\boldsymbol{Y} = [\boldsymbol{y}_1, \boldsymbol{y}_2, \cdots, \boldsymbol{y}_L]$ through L blocks of times, and thus a total of $L \times N$ time slots are required. Then the estimate spatial correlated matrix obtained by the ESPAR antenna is expressed as

$$
\hat{\boldsymbol{R}} = \frac{1}{L} \sum_{l=1}^{L} \boldsymbol{y}_l \boldsymbol{y}_l^H.
\tag{2.21}
$$

In the N-element DBF array, the beampattern is shaped by applying appropriate weights to outputs of N elements. Similarly, we consider applying appropriate weights $\tilde{\boldsymbol{v}} \in \mathbb{C}^{N \times 1}$ to outputs of N beampatterns of the ESPAR array. Since the beampattern of an ESPAR antenna is a function of the loading matrix (see Equations (2.3) and (2.6) to (2.8)), the beamforming is achieved by optimizing

the loading matrix $\boldsymbol{X}$ for a desired equivalent weight vector $\boldsymbol{w}$. However, this beamforming problem is a nonlinear problem due to the inversion in the Equation (2.6) and also the requirement of pure imaginary values of the reactance loads [40, 49]. In order to achieve the MVDR beamformer in the ESPAR array, we introduce a weight vector $\tilde{\boldsymbol{v}}$ (applied to the outputs of N different beams) as the intermediate variable. Indeed, the final goal of the beamforming is to obtain a desired equivalent weight vector $\boldsymbol{w}$ by optimizing $\boldsymbol{X}$, where the intermediate variable $\tilde{\boldsymbol{v}}$ is exploited to perform the function of the MVDR beamformer. The relation between $\tilde{\boldsymbol{v}}$ and $\boldsymbol{X}$ is $\tilde{\boldsymbol{v}}^H \boldsymbol{W}^T = \boldsymbol{w}^T = [(\boldsymbol{Z} + \boldsymbol{X})^{-1}]^T$. Thus, the MVDR beamforming in an ESPAR array is to optimize the loading matrix X by solving the following problem:

$$
\begin{aligned}
\min_{\boldsymbol{X}, \tilde{\boldsymbol{v}}} \quad & \tilde{\boldsymbol{v}}^H \hat{\boldsymbol{R}} \tilde{\boldsymbol{v}} \\
s.t. \quad & \tilde{\boldsymbol{v}}^H \boldsymbol{a}_{rd}(\theta_d) = 1, \\
& \tilde{\boldsymbol{v}}^H \boldsymbol{W}^T = [(\boldsymbol{Z} + \boldsymbol{W})^{-1} \boldsymbol{u}_0]^T.
\end{aligned}
\tag{2.22}
$$

The optimization problem (2.22) is non-convex.

Since it is difficult to directly solve problem (2.22) for $\boldsymbol{X}$. Thus, we first consider a sub-optimal problem: i.e., optimize weight vector $\tilde{\boldsymbol{v}} \in \mathbb{C}^{N \times 1}$ by solving the following problem

$$
\begin{aligned}
\min_{\tilde{\boldsymbol{v}}} \quad & \tilde{\boldsymbol{v}}^H \hat{\boldsymbol{R}} \tilde{\boldsymbol{v}} \\
s.t. \quad & \tilde{\boldsymbol{v}}^H \boldsymbol{a}_{rd}(\theta_d) = 1.
\end{aligned}
\tag{2.23}
$$

It is clear that problem (2.23) is a linear problem. Suppose the solution to (2.23) is $\tilde{\boldsymbol{v}}_{opt}$, then the desired beampattern of the ESPAR is given as $B_d(\theta) = \tilde{\boldsymbol{v}}_{opt}^H \boldsymbol{a}_{rd}(\theta)$. That is, one has the optimized equivalent weight vector $\boldsymbol{w}_{opt}^T = \tilde{\boldsymbol{v}}_{opt}^H \boldsymbol{W}^T$. Then, we will find calculate a necessary loading matrix $\boldsymbol{X}$ for the designed weight equivalent vector $\boldsymbol{w}_{opt}$ (thus a designed beampattern).

Now, the issue is how to achieve the desired beampattern by solving the problem (2.23) through tuning the reactance loads of parasitic elements. Again, there is no known closed-form solution to (2.23), which gives reactance loads with zero real

parts. Therefore, we resort to a strategy iterating between a convex problem and a simple projection of reactance loads, developed in [45], since the optimization problem (2.23) can be reformulated as a convex problem. In particular, the problem (2.13) will be reformulated as an second-order cone programming (SOCP) problem. According to the convex optimization theory [56], an SOCP problem is with the form that the objective function is a linear combination of optimizing variables, while the constraints are either second-order-cone constraints or linear equality (inequality) constraints. However, the objective function in problem (2.23) is quadratic, which does not satisfy the SOCP problem. Moreover, in the ESPAR beamforming related to optimization of reactance loads, we will show later that the optimizing beampattern has to be constrained to a feasible set, thereby leading to difficulty in constraint of the unity distortionless response. Therefore, both the objective function and constraint in problem (2.23) have to be reformulated as follows.

We first reformulate the problem (2.23) as an SOCP problem. Let $\hat{\boldsymbol{R}} = \hat{\boldsymbol{U}}^H \hat{\boldsymbol{U}}$ be the Cholesky decomposition of the estimate correlated matrix. We introduce a new scalar non-negative variable μ_1; then the objective function in (2.23) is rewritten as a constraint $\tilde{\boldsymbol{v}}^H \hat{\boldsymbol{R}} \tilde{\boldsymbol{v}} = \|\hat{\boldsymbol{U}} \tilde{\boldsymbol{v}}\|^2 \leq \mu_1$. And the distortionless response constraint in (2.23) is rewritten as $|\tilde{\boldsymbol{v}}^H \boldsymbol{a}_{rd}(\theta_d) - 1|^2 \leq \mu_2$, where μ_2 is an introduced non-negative variable. Then, we have the following SOCP problem by modifying (2.23)

$$\min_{\mu_1, \mu_2, \tilde{\boldsymbol{v}}} \quad \beta_1 \mu_1 + \beta_2 \mu_2,$$
$$s.t. \quad \|\hat{\boldsymbol{U}} \tilde{\boldsymbol{v}}\|^2 \leq \mu_1, \tag{2.24}$$
$$|\tilde{\boldsymbol{v}}^H \boldsymbol{a}_{rd}(\theta_d) - 1|^2 \leq \mu_2,$$

where β_1, β_2 are auxiliary constants, and μ_1, μ_2 are the weights defining the Pareto-optimal solution: that is, the weights define the importance of minimization of output power and the distortionless response to the desired direction. In particular, the values of constraints β_1, β_2 are chosen depending on the applications. That is, when β_1 is chosen to be larger than β_2, the optimization problem concerns more about the nulls; on the contrary, when β_2 is larger then β_1, optimization concerns

more about high beampattern gain in the direction of interest.

Suppose the solution to (2.24) is $\tilde{\boldsymbol{v}}_{opt}$, and then the corresponding optimized equivalent weight vector $\boldsymbol{w}_{opt}$ can be obtained. Now the problem is how to find the necessary reactance loads of the parasitic elements for $\boldsymbol{w}_{opt}$. As we emphasized, the inversion in Equation (2.6) leads to a non-linear one-to-one mapping between $\boldsymbol{X}$ and $\boldsymbol{w}$. Rearranging (2.6), one has the mapping

$$\boldsymbol{Z}\boldsymbol{w} + \boldsymbol{X}\boldsymbol{w} = \boldsymbol{u}_0. \tag{2.25}$$

Define $\mathcal{L}$ as the set of $\boldsymbol{w}$ corresponding to feasible loadings: i.e., $\boldsymbol{X}$ is of the form given in (2.3) (all diagonal elements are pure imaginary components, except the first one). It is easy to verify that generally $\boldsymbol{w}_{opt} \notin \mathcal{L}$, by using $\boldsymbol{w}_{opt}$ as the input to (2.25). Therefore, it is necessary to approximate $\boldsymbol{w}_{opt}$ by a point in $\mathcal{L}$. Define $\mathbb{P}_{\mathcal{L}}\{\cdot\}$ as an operator projecting $\boldsymbol{w}_{opt}$ to $\mathcal{L}$, which simply gets rid of the real parts of the diagonal elements in $\boldsymbol{X}_{opt}$ calculated by (2.25), except the first one. However, the use of $\mathbb{P}_{\mathcal{L}}\{\cdot\}$ may generate a poor approximation to the desired beampattern defined by $\boldsymbol{w}_{opt}$. Thus, we consider introducing constraints to make sure that the optimizing solutions $\boldsymbol{w}_{opt}$ are "close" to the feasible set $\mathcal{L}$.

The first diagonal element of $\boldsymbol{X}$ is the loading impedance to the active element, and we constrain it to a constant Z_s. According to (2.25), this can be done by using the following equality constraint:

$$[\boldsymbol{Z}(\tilde{\boldsymbol{v}}^H \boldsymbol{W}^T)^T](1) + Z_s[(\tilde{\boldsymbol{v}}^H \boldsymbol{W}^T)^T](1) = 1, \tag{2.26}$$

where $[\cdot](1)$ represents the first element of a vector. Let $\bar{\boldsymbol{Z}}_L$ be a matrix obtained by removing the first row of $(\boldsymbol{Z} + \boldsymbol{X})$. Given a feasible loading $\boldsymbol{X}$ that has the corresponding $\boldsymbol{w} \in \mathcal{L}$, we can maintain the optimizing equivalent weight vector close to the feasible point defined by $\boldsymbol{X}$, by using the Euclidean distance metric

$$\|\bar{\boldsymbol{Z}}_L(\tilde{\boldsymbol{v}}^H \boldsymbol{W}^T)^T\|^2 \leq \epsilon \tag{2.27}$$

where $\epsilon > 0$ is some small constant, defining the distance between the $\boldsymbol{w}$ being optimized and a feasible point in $\mathcal{L}$. With these constraints, the use of $\mathbb{P}_{\mathcal{L}}\{\cdot\}$ will not destroy the characteristics of the beampattern optimized by the MVDR algorithm, as $\boldsymbol{w}$ is close to $\mathcal{L}$.

Including constraints (2.26) and (2.27) in optimization problem (2.23), we have the final MVDR optimization problem modified for the ESPAR arrays [57]:

$$\min_{\mu_1,\mu_2,\tilde{\boldsymbol{v}}} \quad \beta_1\mu_1 + \beta_2\mu_2, \tag{2.28a}$$

$$s.t. \quad \|\hat{\boldsymbol{U}}\tilde{\boldsymbol{v}}\|^2 \leq \mu_1, \tag{2.28b}$$

$$|\tilde{\boldsymbol{v}}^H\boldsymbol{a}_{rd}(\theta_d) - 1|^2 \leq \mu_2, \tag{2.28c}$$

$$\|\bar{\boldsymbol{Z}}_L(\tilde{\boldsymbol{v}}^H\boldsymbol{W}^T)^T\|^2 \leq \epsilon, \tag{2.28d}$$

$$[\boldsymbol{Z}(\tilde{\boldsymbol{v}}^H\boldsymbol{W}^T)^T](1) + Z_s[(\tilde{\boldsymbol{v}}^H\boldsymbol{W}^T)^T](1) = 1. \tag{2.28e}$$

It is obvious that (2.28) is still an SOCP problem, that can be effectively solved by the interior-point methods [56].

The iterative beamforming strategy is described as follows. First select an initial value $\boldsymbol{X}_0$. It is used as the input to the SOCP problem (2.28) to optimize $\boldsymbol{v}$. Then obtain $\boldsymbol{w}_{opt}$, and a corresponding $\boldsymbol{X}_1^\star$ is calculated by (2.25). The projected solution $\boldsymbol{X}_1$ is achieved by getting rid of real parts of diagonal elements of $\boldsymbol{X}_1^\star$ except the first element which is constrained to a constant Z_s due to (2.28e). Again, the reactance load of each parasitic element should be restricted in a practical range (e.g., $[-300\Omega, 300\Omega]$). The above procedure is repeated with updated values of $\boldsymbol{X}$ until convergence.

In [58], it is demonstrated that the presence of the desired signal during the signal measurements under limited sampling numbers may lead to significant SINR degradation of the MVDR beamformer. The impact on our proposed method will be shown in the simulation results later. To overcome this problem, we consider replacing the signal estimate correlation matrix $\hat{\boldsymbol{R}}$ by the interference-plus-noise estimate correlation matrix $\hat{\boldsymbol{R}}_{i+n}$. This may be simply achieved when the desired user is silent, but it requires cooperation among users. Another method is using

a pilot-assisted algorithm, like the one developed in [58], to subtract the desired signal from measured signals before computing the estimate spatial correlated matrix.

2.2.4   Genetic Algorithm based Strategy

Although the GA-based beamforming method is a slow convergence solution, so that it might be impractical in real-time applications, it is still worth studying for the ESPAR array, since the greatest advantage of GA is that it can avoid becoming trapped in the local minima/maxima. Therefore, it outperforms some stochastic based beamforming algorithms. In this section, we present the GA for calculation of parasitic reactance loads to achieve the desired beampattern, which will be exploited for interference mitigation schemes later.

The GAs, as one kind of "global" optimization technique, have been successfully applied to many electromagnetic design problems which may not be readily handled by other traditional optimization methods. For example, the GAs have been used for antenna design in [59–61], antenna pattern synthesization [62], and also calculation of reactance loads for the ESPAR array [51, 52].

In the GA-based beamforming method for the ESPAR array, variables to be optimized are parasitic reactance loads $x_m, m \in \{1, \cdots, M\}$. In this work, we consider the binary-encoded GA, and thus a reactance load is encoded into a sequence of binary bits that constitutes a gene – the basic building block of the GA. The value of a reactance load is constrained in a practical range $[-x_{lim}, x_{lim}]$ (e.g., $x_{lim} = 300$ Ω [40]), which can be supported by the varactor control circuit. Let Δx be the searching resolution of a reactance value in the available range. Given the searching range and resolution, we can obtain the quantization levels N_{lev}. Therefore, a reactance load is encoded into $N_g = round(log_2(N_{lev}))$ bits (i.e., length of a gene). The set of M genes is called a chromosome with the length of $M \times N_g$ bits. Each chromosome is associated with an objective function, assigning "fitness" to that chromosome. The objective function for each chromosome is maximization of

the CCC between the desired beampattern denoted by $B_d(\theta)$ and an beampattern achievable at the ESPAR denoted by $B_a(\theta)$: that is,

$$\max \quad f(x_1, \cdots, x_M) = \frac{|\int_0^{2\pi} B_d^*(\theta) B_a(\theta) d\theta|}{\sqrt{\int_0^{2\pi} |B_d(\theta)|^2 d\theta \cdot \int_0^{2\pi} |B_a(\theta)|^2 d\theta}}. \qquad (2.29)$$

In addition, if the reference signal $r(t)$ is available, the objective function can be modelled as the CCC between the reference signal and the received signal $y(t)$ (expressed in (2.12)) at the sole RF port, given by

$$\max \quad f(x_1, \cdots, x_M) = \frac{\mathbb{E}\{y(t)r^*(t)\}}{\sqrt{\mathbb{E}\{y(t)y^*(t)\}\mathbb{E}\{r(t)r^*(t)\}}}. \qquad (2.30)$$

The GA starts with randomly generating a large number (N_{ch}) of chromosomes which are referred to as the population of the first generation. An example of a binary-encoded chromosome is of the form:

$$Chromosome = \underbrace{101 \cdots 1}_{x_1} \underbrace{001 \cdots 1}_{x_2} \cdots \underbrace{110 \cdots 0}_{x_M}.$$

Each chromosome is evaluated according to the cost function (2.29) or (2.30) and assigned the corresponding fitness. As the chromosomes are given as binary strings, they have to be decoded first, and then the decoded reactance values x_m are used to calculate the achievable beampattern $B_a(\theta)$ or the received signal $y(t)$, which is the input to the objective functions. According to the fitness values assigned to chromosomes, an appropriate portion of chromosomes are selected as "parents" to reproduce offspring. To select "parents", we adopt the roulette wheel selection scheme [63], which is widely used in the GAs. In the roulette wheel selection scheme, the selection probability of the i-th chromosome is represented as

$$Pr_i = \frac{f_i}{\sum_{i=1}^{N_{ch}} f_i}, \qquad (2.31)$$

where f_i is the fitness value assigned to the i-th chromosome. The selected chromosomes are then paired to operate crossover to reproduce two offspring. Consider
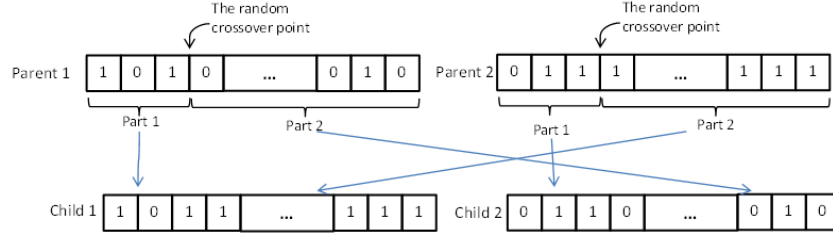
FIGURE 2.5: Crossover procedure.

the one-point crossover [60], in which one crossover point is randomly generated in the paired parental chromosomes dividing the binary strings into two parts: child 1 is given as the combination of the 1st part of parent 1 and the 2nd part of parent 2, while child 2 is the combination of the rest of the parts from the parents. The one-point crossover procedure is shown in Figure 2.5. In this work, we also use Elitism to enable the fittest chromosomes to be copied to the next generation. In particular, the Elitism means that a number of chromosomes with high fitness level are kept and copied to the offspring.

Finally, the mutation is performed, where a small percentage of bits is randomly selected from the list of reproduced chromosomes and they are changed from "1s" to "0s" or vice versa. The mutation helps to increase the GA's searching outside the current region of parameter space. In general, the mutation level is set to 1% of the total $N_{ch} \times N_g$ at each iteration. It should be noted that, at the final iteration, no mutation is performed. Once the mutation has been accomplished, the new list of chromosomes is the new generation. The procedure described above is repeated until convergence, or until the pre-determined maximum number of generations (iterations) has been exceeded.

2.3 Switched-Beam ESPAR Antennas

In addition to adaptive beamforming, the ESPAR antenna provides a solution for beam switching. Although it may not be an optimal solution, beam switching
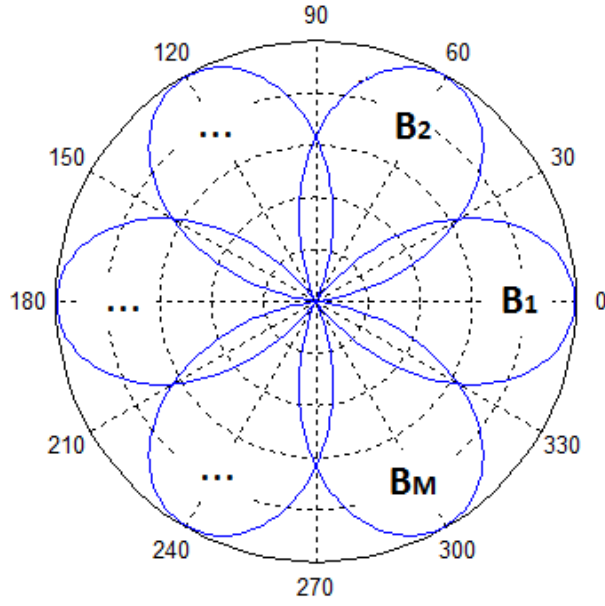
FIGURE 2.6: Example of sector beampatterns.

is sufficient in many applications (this will be described in later chapters). The switched-beam ESPAR antenna is easier to implement, due to its low complexity.

Specifically, the reactance loads of parasitic elements can be optimized to maximize the beam gain in a look direction (e.g., 0°), which can be achieved by using the beamforming methods previously described. Due to the symmetric antenna structure, circularly shifting elements of the optimal reactance loads rotates the beampattern to different directions. With this method, an $(M + 1)$-element ESPAR can achieve M directional beampatterns, dividing its whole angle space into M angular sectors: these are referred to as the *sector beampatterns* (as illustrated in Figure 2.6). Each angular sector is accessed by the corresponding beampattern. Directional sector beampatterns provide an SNR gain for reception and transmission of directional signals, the spatial filtering to suppress co-channel interference and also spatial diversity, by scanning the angle space through each of the sector beampatterns.

2.4   Simulation Results

In this section, we show some representative results for performance evaluation of the proposed beamforming algorithms. The simulated ESPAR antenna has $M + 1 = 7$ half-wavelength thin electrical dipoles. The inter-element spacing is set to $d = \lambda/4$. The mutual impedance matrix $\boldsymbol{Z}$ (calculated using the analytical formulas given in Appendix A) has the following form:

$$\boldsymbol{Z} = \begin{bmatrix} Z_{00} & Z_{01} & Z_{01} & Z_{01} & Z_{01} & Z_{01} & Z_{01} \\ Z_{01} & Z_{00} & Z_{01} & Z_{02} & Z_{03} & Z_{02} & Z_{01} \\ Z_{01} & Z_{01} & Z_{00} & Z_{01} & Z_{02} & Z_{03} & Z_{02} \\ Z_{01} & Z_{02} & Z_{01} & Z_{00} & Z_{01} & Z_{02} & Z_{03} \\ Z_{01} & Z_{03} & Z_{02} & Z_{01} & Z_{00} & Z_{01} & Z_{02} \\ Z_{01} & Z_{02} & Z_{03} & Z_{02} & Z_{01} & Z_{00} & Z_{01} \\ Z_{01} & Z_{01} & Z_{02} & Z_{03} & Z_{02} & Z_{01} & Z_{00} \end{bmatrix}$$

where $Z_{00} = 73.07 + j42.5$, $Z_{01} = 40.75 - j28.32$, $Z_{02} = -0.66 - j35.93$, $Z_{03} = -12.52 - j29.9$. In this work, we assume the loading impedance of the LNA is matched to the input impedance of the ESPAR array: i.e., $Z_s = Z_{in}$, so that the antenna efficiency can be considered as 100%.

2.4.1   MVDR Beamforming

In this section, we evaluate the performance of the MVDR beamforming algorithm. Here, we use $N = 7$ sets of reactance loads to realize signal sampling over 7 beams in the ESPAR array (the RD technique). As discussed in Section 2.2.3, in order to get $L = 100$ measurement vectors stored in the matrix $\boldsymbol{Y}$, a total of $L \times N = 700$ sampling periods are required in the MVDR algorithm for the ESPAR array. The SOCP problem (2.23) was solved using YALMIP [64] as the modelling tool and the free optimization software SeDuMi [65].

In simulations, we first consider performance comparison in three scenarios: 1) desired signal is from 0° and one interference is from 120°; 2) desired signal is from

90° and one interference is from 120°; 3) the desired and interfering directions are set as the same as in scenario 2, but here the measurements include only interference and noise ($\hat{\boldsymbol{R}}_{i+n}$). That is, the desired signal is subtracted form the measurements, similar to the formulation in minimizing output energy as proposed in [58]. Here, SNR and SIR (signal-to-interference ratio) are set to 10 dB and 0 dB, respectively.

Figure 2.7 shows that the designed beampatterns place nulls at the interfering directions and steer to the desired direction; however, when the angular separation between the desired signal and interference becomes small (scenario 2), the null depth is decreased by 8 dB compared to scenario 1. With the same angular separation, the performance of scenario 3 is improved compared to that of scenario 2, where we can observe a 3 dB increment in the null depth, because the desired signal is not present in signal measurements. Figure 2.8 shows the convergence performance of the ESPAR-based MVDR beamforming. The results of three scenarios are all converged within 20 iterations. Further, this illustrates again that subtracting the desired signal from measurements leads to improvement in beamforming performance when interference is close to the desired source. In the MVDR algorithm, there is a projection procedure, and we use a Euclidean metric (2.27) to make sure that the projection does not destroy the characteristics of the optimized beampattern. To illustrate this, we show the projected and optimized beampatterns in scenario 1 ($\epsilon = 0.1$) in Figure 2.9. A small difference between the two beampatterns is observed. The same results are also achievable for scenarios 2 and 3. In these simulated beampatterns, the maximum gain does not show 0dB (unity distortionless response in the direction of interest) like a conventional MVDR beamformer in DFB arrays, because in the optimization problem (2.28) $\tilde{\boldsymbol{v}}$ instead of $\boldsymbol{w}$ is maintained to approach to unity.

Next, we examine the performance of the MVDR algorithm at the presence of two interferers. The SNR and SIR are also set to 10 dB and 0 dB, respectively. The transmit powers of two interfering signals are set to be equal to half that of the desired signal. Moreover, in order to improve the beamforming performance, we assume that the desired signal has been subtracted from the signal measurements.

Figure 2.10 depicts two designed beampatterns, where the interfering signals are from 90° and 270° for the first design, and the interfering signals are from 180° and 270° for the second design. Both beampatterns are designed with nulls placed towards interferers. Up to a -20 dB null depth ratio is achievable.
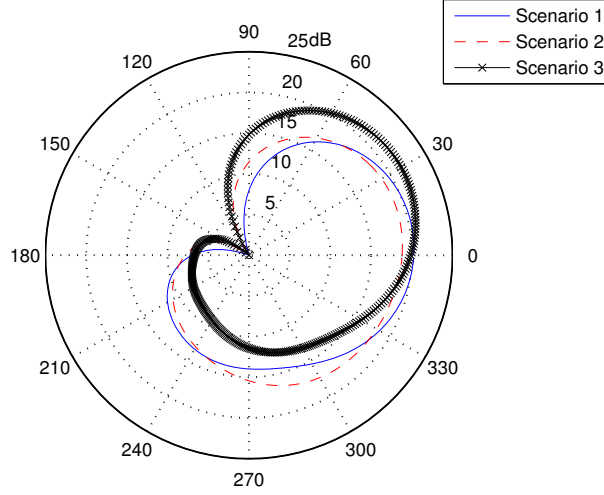
FIGURE 2.7: MVDR beamforming results under three scenarios: SNR=10 dB, SIR=0 dB.
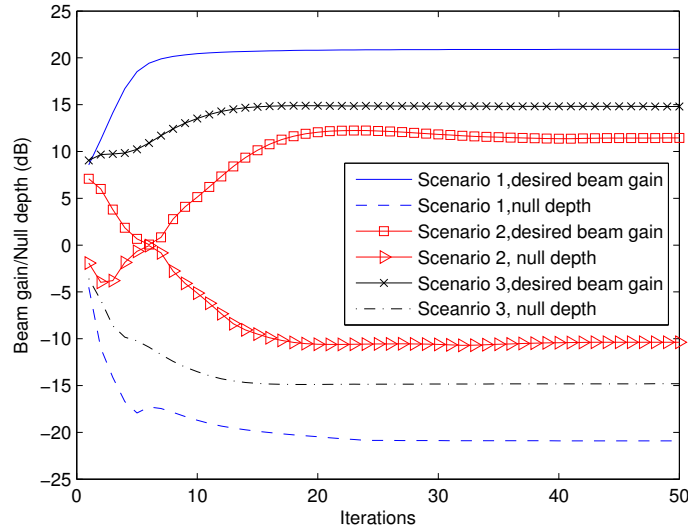
FIGURE 2.8: Convergence performance of MVDR beamforming under three scenarios.
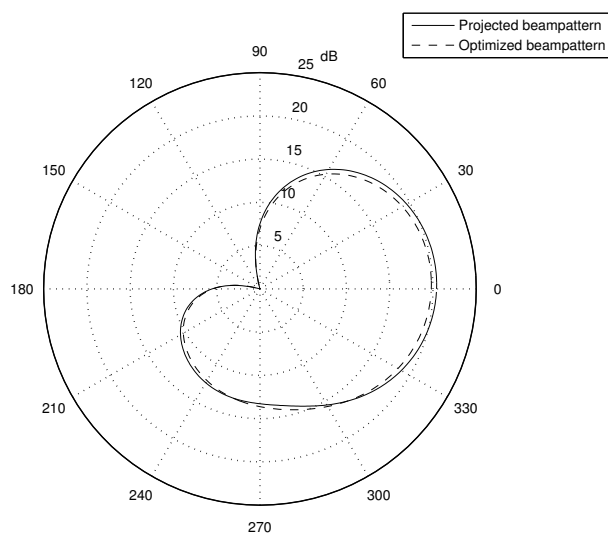
FIGURE 2.9: Difference between the projected and optimized beampatterns using a Euclidean metric ($\epsilon = 0.1$).
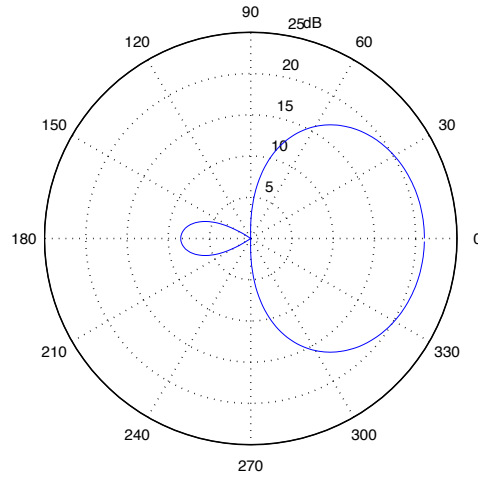
(a) Interferers at 90° and 270°
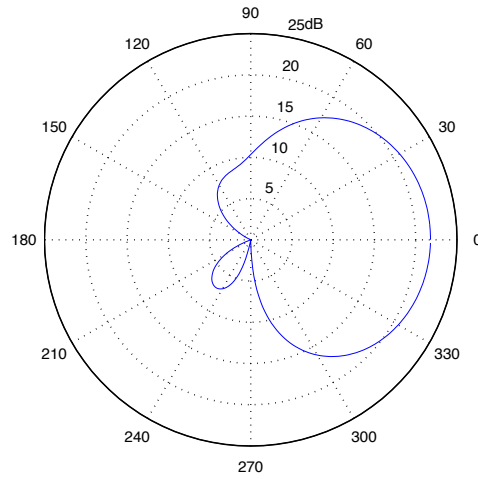
(b) Interferers at 180° and 270°

FIGURE 2.10: MVDR beamforming results at the presence of two interferers. SIR=0 dB, SNR=10 dB, 20 iterations.

2.4.2 GA-based Beamforming

We will now evaluate performance of the GA-based beampattern design method. Some parameters for simulations are summarized in Table 2.1.

TABLE 2.1: GAs Parameters

Parameter	Value
Number of genes	6
Bits per gene	12
Reactance limit x_{lim}	$300(\Omega)$
Population size	100
Number of generations	100
Crossover probability	0.7
Mutation probability	0.1

We first study the case using a reference signal from the desired direction $0°$. Consider three scenarios, where one interfering signal is from $90°$, $180°$ and $330°$, respectively. The SNR and SIR are set to 10 dB and 0 dB, respectively. The length of the data sample block is set to 50 bits. The cost function for each chromosome is calculated by (2.30). In Figure 2.11, we see that the designed beampatterns place one deep null at $90°$, $180°$ and $330°$, and all of them steer to the desired direction at $0°$. However, we also observe that the output SINR degrades when the desired signal is close to the interference (see Figure 2.11(c)). It is worth emphasizing that this problem is shown in the GA-based and MVDR algorithms, due to the antenna property. To explain this, we calculate the spatial correlation coefficient between ESPAR's steering vectors corresponding to the desired direction $\theta_d = 0°$ and the varying interfering directions $\theta_i \in [0°, 360°]$. The results are plotted in Figure 2.12, where it is observed that the value of the spatial correlation coefficient increases when the interferer becomes closer to the desired signal. It is demonstrated that the lower the spatial correlation between the desired signal and interference, the better the nulling performance of a designed beampattern [40].

The beamforming performance is also evaluated at the presence of two interferers. Consider two scenarios: 1) interference from $90°$ and $270°$; 2) interference from $180°$ and $270°$. The desired direction is kept at $0°$ for both scenarios. The transmit
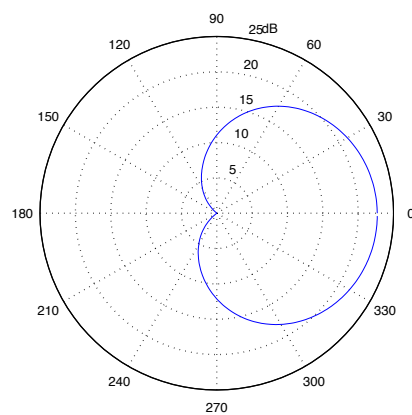
(a) Interference at 90°
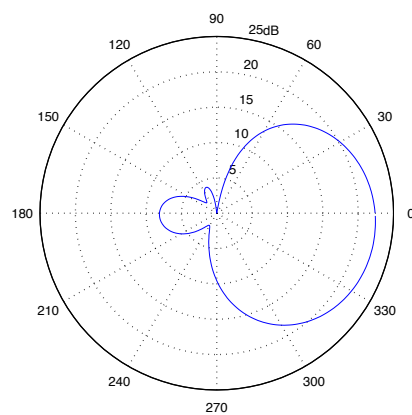
(b) Interference at 180°
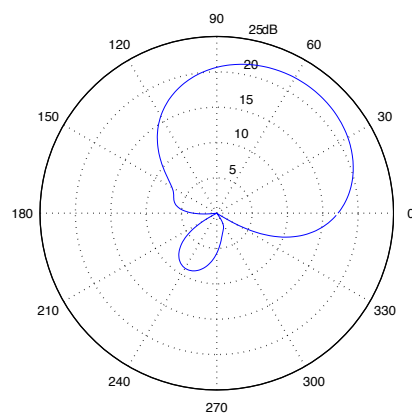
(c) Interference at 330°

FIGURE 2.11: GA-based beamforming simulation results. SNR=10 dB, SIR=0 dB.
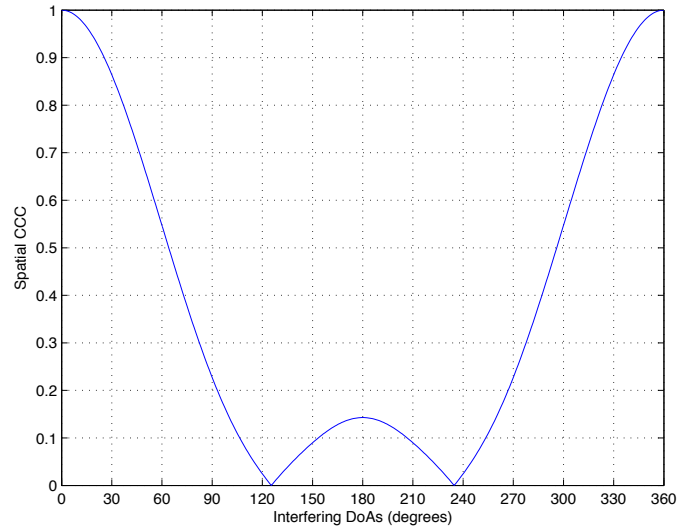
FIGURE 2.12: Spatial correlation coefficients between ESPAR steering vectors corresponding to desired direction (0°) and varying interfering direction (from 0° to 360°).

power of each interfering signal is assumed to be equal to half that of the desired signal. SNR is set to 10 dB, and SIR is set to 0 dB. Figure 2.13 shows that the output beampatterns for both scenarios have good nulling performance towards two interfering directions.

Finally, we examine the GA-based beamforming algorithm with the desired beampattern available. For example, take the desired beampattern as $B_d(\theta) = 1 - \cos(\theta)$. The cost function (2.29) is used. In Figure 2.14 the desired and simulated beampatterns are plotted, where we can observe that the simulated beampattern approximates to the desired one. It should be pointed out that the performance of the GA method approaching a desired beampattern cannot always be guaranteed. This depends on the shape of the desired beampattern. In other words, we cannot design an ESPAR beampattern to approach an arbitrary pattern shape: that is a very strict requirement. However, we can still exploit the GA method to design an ESPAR beampattern to approximate the desired beampattern as much as possible, which may still be sufficient in some applications.
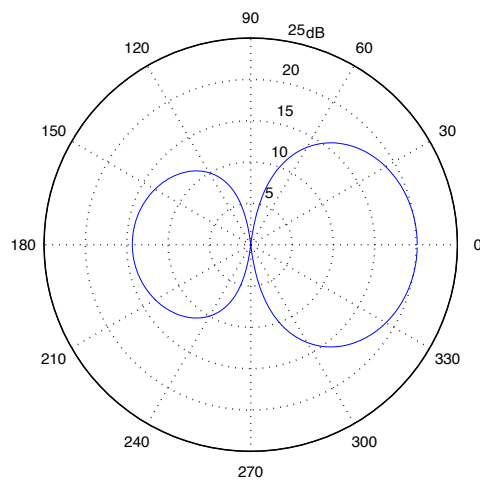
(a) Interferers at $90°$ and $270°$
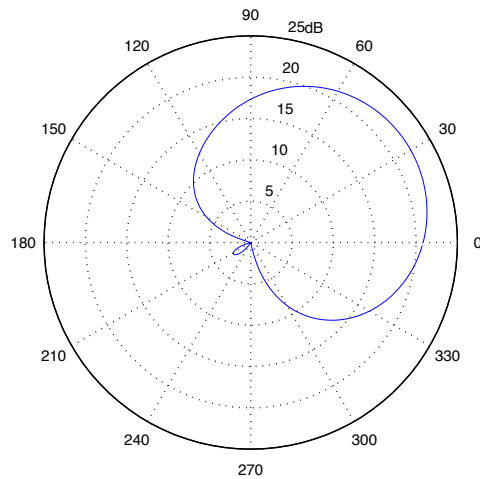
(b) Interferers at $180°$ and $270°$

FIGURE 2.13: Simulation results of GA-based beamforming at the presence of two interferers. SIR=0 dB, SNR= 10 dB.
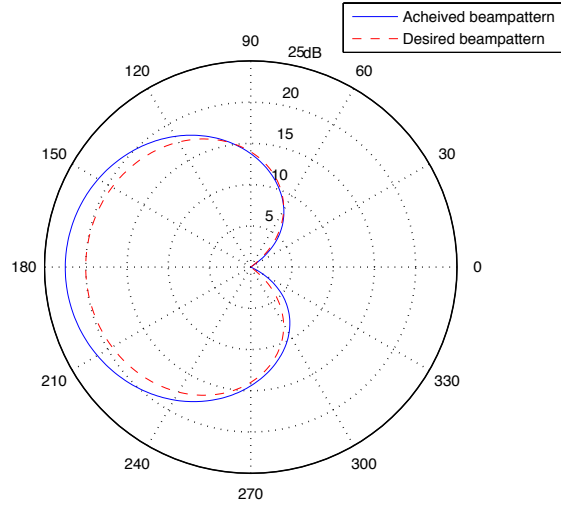
FIGURE 2.14: Simulated beampatterns compared to the desired beampatttern.

2.5   Summary

In this chapter, we have shown the adaptive beamforming methods for an ESPAR antenna, which is a smart antenna, uses only a single RF chain and several parasitic elements coupled to the sole active element. Unlike a DBF array, its beampattern is controlled by electronically tuning reactance loads connected to parasitic elements.

- In order to obtain a correlation matrix of signals with the single-active antenna system, reactance-domain signal processing rather than element-domain signal processing is exploited. Specifically, a fixed number of beampatterns defined by different sets of reactance loads connected to parasitic elements are used. Signals derived by individual beampatterns are then manipulated to achieve a specific goal.

- The MVDR beamfomer is modified as an iterative algorithm suited to the ESPAR antenna. In particular, the beampattern design strategy iterates between a convex problem and a simple projector. The optimization problem, minimizing power from interference and maintaining the distortionless response in the direction of interest, is reformulated as a SOCP problem, using a Euclidean metric to avoid poor approximation of the optimized

beampattern. The simulations verified its fast convergence and feasibility in beampattern design.

- The feasibility of the GA as an adaptive beamforming for the ESPAR antenna, using a reference signal or knowledge of a desired beampattern, has also been verified.

- Finally, it has been presented that the ESPAR antenna is able to work as a switched-beam antenna by circular permutations of a set of predesigned reactance loads, thereby rotating beampattern to different angular sectors. Due to the simplicity of the switched-beam antenna, it will also be adopted in the wireless communication techniques described later.

Chapter 3

ESPAR-based Blind Interference Alignment

3.1 Introduction

Recently, an emerging technique, termed *interference alignment* (IA), has gained significant attention as a promising solution for interference management, thereby improving spectrum efficiency in wireless communications. The central concept of IA is the signal design that casts interference in a reduced subspace (time, frequency, space, etc.), while remaining separate from the desired signal [66]. Based on feasibility conditions, various transmit and receive strategies [66–70] have been proposed for IA to achieve the maximum multiplexing gain at each receiver. Although substantial capacity benefits have been demonstrated, most of these IA schemes assume perfect, sometimes global, knowledge of the CSI at transmitters (CSIT), prohibiting them from practical implementation. In [71, 72], the authors claim that, without channel knowledge, DoFs of many networks, especially with independent and identical distributed (i.i.d) fading models, will collapse to that simply using orthogonal time-division multiple accessing (TDMA).

To achieve a practical IA scheme, blind interference alignment (BIA) has been introduced by Jafar [73], where "blind" means no knowledge of CSIT. Jafar studied five network communication problems – MISO BC (broadcast channel), X channel, the $M \times 2$ X channel, two-user MIMO interference channel and K-user interference channel – to demonstrate that the transmitters can exploit only the knowledge of channel coherence intervals instead of CSIT to align interference in multi-user settings. Gou et al. [27] then extended BIA for a general K-user $N_t \times 1$ MISO BC, where N_t is the number of transmit antennas. A heterogeneous block fading model is created with the use of a reconfigurable antenna at the receiving end to switch between N_t antenna models in a pre-determined fashion. A reconfigurable antenna is an antenna capable of dynamically changing its antenna modes, e.g., frequency, polarization, and beampattern, via advanced technologies such as micro-electromechanical systems (MEMS) switches. Frequency switching will increase the necessary frequency band, and polarization switching may be only suitable for communication systems that are insensitive to transmitter and receiver orientations (e.g., satellites). In this sense, beampattern switching is an easier way to implement BIA. For many applications, a reconfigurable antenna with a single-RF chain is more suitable, due to the space, power and cost constraints on modern wireless terminals. A normalized DoF of $\frac{N_t K}{N_t + K - 1}$ is shown to be achievable in this BIA system, with only finite symbol extensions and no channel knowledge at the receiver to null the interference.

This chapter is devoted to the employment of the ESPAR antenna as a beam switching solution for the practical implementation of BIA [27], which aligns inter-user interference into a reduced subspace without CSIT in the multi-user MISO BC. In Section 3.3 we review the original BIA scheme, where the main idea is related to building the *Super Symbol*[1] structure. In Section 3.4, we present the key point of our work: the ESPAR beamforming method suited to the BIA application. It is noted that $N_t > 1$ different beampatterns are required to be designed for one channel realization use. Indeed, BIA has its own intrinsic problem, i.e., noise

---

[1]The *Super Symbol* is a symbol extension structure introduced as a transmission unit, that is defined for each N_t and K [27]. It includes information about the beam-switching manner for each receiver and the precoding method for the transmitter.

amplification comes from the interference zero-forcing process. Thus, we also consider exploiting directional beampatterns of the ESPAR antenna to improve performance of BIA, by enhancing receive SNR. The greatest advantage of the BIA is that it reduces CSIT overhead. Finally, we examine the proposed ESPAR-based BIA scheme in comparison with other CSIT-based techniques (LZFBF), taking into account the CSI overheads (Section 3.5).

3.2 System Model

Consider the downlink of a K-user $N_t \times 1$ MISO BC, where the transmitter is equipped with an N_t-element antenna array (e.g., ULA) while each of K receivers is equipped with a reconfigurable antenna (thus only one RF chain) capable of switching among at least N_t antenna modes. In this work, an $(M + 1)$-element ESPAR antenna is adopted as the reconfigurable antenna, where $M \geq N_t$. The ESPAR antenna is required to be able to switch between N_t different beam-patterns. Let the set $\mathcal{B} = \{B_1, \cdots, B_{N_t}\}$ store the required beampatterns. A unique receiver is intended to receive an independent message from the transmitter. The diagram of the system model is shown in Figure 3.1. Let the vector $\mathbf{h}^{[k]}(B_n) \in \mathbb{C}^{1 \times N_t}, k \in \mathcal{K} = \{1, \cdots, K\}, B_n \in \mathcal{B}$, denote the channel between the transmitter and receiver k, when the receive ESPAR antenna forms beampattern B_n.
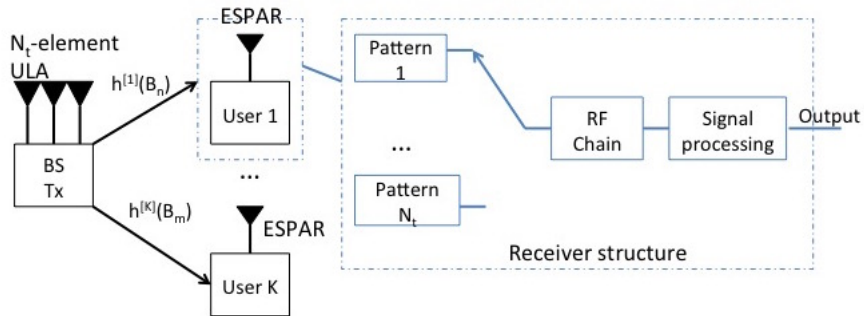
FIGURE 3.1: Diagram of the system model.

The propagation environment is modelled as a parametric physical model considering the geometry of the scattering environment [74, 75]. Suppose that there are N_{sc} paths reflected by N_{sc} scatterers distributed in the network. Each path $i \in \{1, \cdots, N_{sc}\}$ connecting the areas of the transmitter and receiver has a single angle of departure (AoD) $\theta_{t,i}$, a single AoA $\theta_{r,i}$, and a path gain α_i (α_i follows flat Rayleigh fading). Assume that, the ESPAR antenna of receiver k is forming beampattern $B_n(\theta)$. According to (2.7), we have the channel vector $\boldsymbol{h}^{[k]}(B_n)$ associated with beampattern B_n, expressed as

$$
\begin{aligned}
\boldsymbol{h}^{[k]}(B_n) &= \sum_{i=1}^{N_{sc}} \alpha_i B_n(\theta_{r,i}) \boldsymbol{a}_t^H(\theta_{t,i}) \\
&= \boldsymbol{w}_n^T \underbrace{\boldsymbol{A}_r(\boldsymbol{\theta}_r) \boldsymbol{H}_a \boldsymbol{A}_t^H(\boldsymbol{\theta}_t)}_{\boldsymbol{G}},
\end{aligned}
\tag{3.1}
$$

where $B_n(\theta_{r,i})$ represents the n-th beampattern sampled at $\theta_{r,i}$, $\boldsymbol{w}_n$ is the equivalent weight vector used to form beampattern B_n, $\boldsymbol{a}_t(\theta) \in \mathbb{C}^{N_t \times 1}$ is the transmit steering vector (defined by the geometry of the ULA). Vectors $\boldsymbol{\theta}_r$ and $\boldsymbol{\theta}_t$ store all paths' AoAs and AoDs, respectively, and thus $\boldsymbol{A}_r(\boldsymbol{\theta}_r)$ and $\boldsymbol{A}_t(\boldsymbol{\theta}_t)$ are matrices with columns of receive steering vectors corresponding to N_{sc} AoAs and transmit steering vectors corresponding to N_{sc} AoDs, respectively. $\boldsymbol{H}_a$ is an $N_{sc} \times N_{sc}$ diagonal matrix with complex path gains α_i as diagonal entries.

It is worth emphasizing that, in the channel coherence block structures, coherence times are assumed to be long enough to ensure constant channels across a *Super Symbol* [27]: that is, $\boldsymbol{G}$ in (3.1) is assume to be constant across a *Super Symbol*. This is a fundamental assumption for the BIA, and we will discuss it later.

Assuming staggered beampattern switching at the receiver in a pre-determined pattern, at time t, let receiver k switch to beampattern $B_n(t)$, resulting in channel $\boldsymbol{h}^{[k]}(B_n(t))$. At time t, the received signal at receiver k is

$$
y^{[k]}(t) = \boldsymbol{h}^{[k]}(B_n(t)) \boldsymbol{s}(t) + z^{[k]}(t), \quad k \in \mathcal{K}, \quad B_n(t) \in \mathcal{B},
\tag{3.2}
$$

where $\boldsymbol{s}(t) \in \mathbb{C}^{N_t \times 1}$ is the transmitted signal vector, $z^{[k]} \sim \mathcal{CN}(0,1)$ is the additive white Gaussian noise (AWGN). The input of the channel is subjected to the average power constraint, i.e., $\mathbb{E}\{\|\boldsymbol{s}(t)\|^2\} \leq P_t$, where P_t is the total transmit power. Throughout this chapter, we assume no CSIT. It is noted that, although the CSI at the receiver (CSIR) is not required in the BIA procedure, perfect CSIR is assumed primarily in order to be able define the DoFs as the capacity pre-log [27].

3.3 Review of Blind Interference Alignment

The original BIA scheme developed by Gou et al. [27] exploits finite symbol extensions, jointly combined with antenna mode switching at the receiving end, to achieve inter-user interference alignment without CSIT. Here, we first present the general idea of the BIA scheme via the simplest 2-user 2×1 MISO BC case. Since the *Super Symbol* includes all information about the BIA, we then describe the construction of the *Super Symbol* for the system with arbitrary values of K and N_t. Thus, the staggered beampattern switching manner, precoding matrices and post-processing methods can be obtained straightforwardly.

3.3.1 Two-User 2×1 MISO BC

For the 2-user 2×1 MISO BC, the transmitter is intended to simultaneously send two interference-free data streams to each of the two users, denoted by $\boldsymbol{u}^{[k]} = [u_1^{[k]}, u_2^{[k]}]^T, k = \{1, 2\}$. The *Super Symbol* is constructed by staggered beampattern switching (Figure 3.2). We drop the user index from the beampattern notation for simplicity. We can see that the length of the *Super Symbol* is three symbol periods. For the staggered beampattern switching manners for individual users, user 1 switches to B_1 at the 1st and 3rd symbol periods, and switches to B_2 at the 2nd symbol period; meanwhile, user 2 switches to B_1 at the 1st and 2nd symbol periods, and switches to B_2 at the 3rd symbol period. We would like to

emphasize that the beampattern is independently designed at each receiver, so that $B_n^{[1]} \neq B_n^{[2]}, n \in \{1, 2\}$.
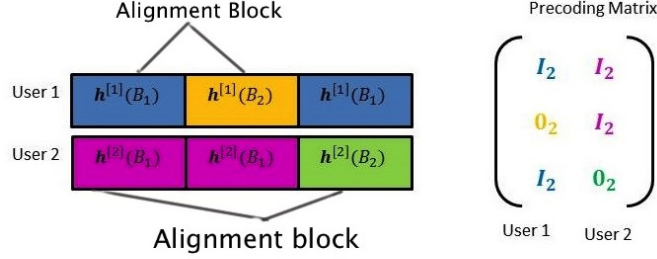
FIGURE 3.2: *Super Symbol* for the 2-user 2×1 MISO BC case.

The precoding matrices across the block of three symbol periods for each user are designed based on the *Super Symbol*. The precoding matrix for one user is a 6×2 matrix, storing three 2×2 matrices each for one symbol period across the *Super Symbol*. For one 2×2 matrix in the precoding matrix, if its corresponding symbol belongs to the *Alignment Block*[2], then it is a 2×2 identity matrix $\boldsymbol{I}_2$; otherwise it is a 2×2 zero matrix $\boldsymbol{0}_2$. The resulted precoding matrices for two users can be found in Figure 3.2. With the precoding matrices, the transmit signal across a *Super Symbol* is designed as

$$\begin{bmatrix} \boldsymbol{s}(1) \\ \boldsymbol{s}(2) \\ \boldsymbol{s}(3) \end{bmatrix} = \begin{bmatrix} \boldsymbol{I}_2 \\ \boldsymbol{I}_2 \\ \boldsymbol{0}_2 \end{bmatrix} \boldsymbol{u}^{[1]} + \begin{bmatrix} \boldsymbol{I}_2 \\ \boldsymbol{0}_2 \\ \boldsymbol{I}_2 \end{bmatrix} \boldsymbol{u}^{[2]}. \tag{3.3}$$

From the above transmitted signals, it can been that, at the first time slot, both users' symbols are transmitted, and at the second and third time slots only one user's symbols are transmitted at each time slot. It is clear that the transmit power used at the first time slot is twice that used at the second and third time slots. This is related to large noise amplification, which will be discussed later.

---

[2]The *Alignment Block* is introduced in [27] as a building unit to constitute the *Super Symbol*. We will explain it later.

The transmission strategy jointly coordinates the staggered beampattern switching at individual receivers. In consequence, the received signals across a *Super Symbol* for users 1 and 2 are respectively expressed as

$$
\begin{bmatrix} y^{[1]}(1) \\ y^{[1]}(2) \\ y^{[1]}(3) \end{bmatrix} = \begin{bmatrix} \boldsymbol{h}^{[1]}(B_1) & \boldsymbol{0} & \boldsymbol{0} \\ \boldsymbol{0} & \boldsymbol{h}^{[1]}(B_2) & \boldsymbol{0} \\ \boldsymbol{0} & \boldsymbol{0} & \boldsymbol{h}^{[1]}(B_1) \end{bmatrix} \begin{bmatrix} \boldsymbol{s}(1) \\ \boldsymbol{s}(2) \\ \boldsymbol{s}(2) \end{bmatrix} + \begin{bmatrix} z^{[1]}(1) \\ z^{[1]}(2) \\ z^{[1]}(3) \end{bmatrix}
$$

$$
= \underbrace{\begin{bmatrix} \boldsymbol{h}^{[1]}(B_1) \\ \boldsymbol{h}^{[1]}(B_2) \\ \boldsymbol{0} \end{bmatrix} \boldsymbol{u}^{[1]}}_{\substack{rank=2 \\ \text{desired signal}}} + \underbrace{\begin{bmatrix} \boldsymbol{h}^{[1]}(B_1) \\ \boldsymbol{0} \\ \boldsymbol{h}^{[1]}(B_1) \end{bmatrix} \boldsymbol{u}^{[2]}}_{\substack{rank=1 \\ \text{interference}}} + \begin{bmatrix} z^{[1]}(1) \\ z^{[1]}(2) \\ z^{[1]}(3) \end{bmatrix}, \tag{3.4}
$$

$$
\begin{bmatrix} y^{[2]}(1) \\ y^{[2]}(2) \\ y^{[2]}(3) \end{bmatrix} = \begin{bmatrix} \boldsymbol{h}^{[2]}(B_1) & \boldsymbol{0} & \boldsymbol{0} \\ \boldsymbol{0} & \boldsymbol{h}^{[2]}(B_1) & \boldsymbol{0} \\ \boldsymbol{0} & \boldsymbol{0} & \boldsymbol{h}^{[1]}(B_2) \end{bmatrix} \begin{bmatrix} \boldsymbol{s}(1) \\ \boldsymbol{s}(2) \\ \boldsymbol{s}(3) \end{bmatrix} + \begin{bmatrix} z^{[2]}(1) \\ z^{[2]}(2) \\ z^{[2]}(3) \end{bmatrix}
$$

$$
= \underbrace{\begin{bmatrix} \boldsymbol{h}^{[2]}(B_1) \\ \boldsymbol{h}^{[2]}(B_1) \\ \boldsymbol{0} \end{bmatrix} \boldsymbol{u}^{[1]}}_{\substack{rank=1 \\ \text{interference}}} + \underbrace{\begin{bmatrix} \boldsymbol{h}^{[2]}(B_1) \\ \boldsymbol{0} \\ \boldsymbol{h}^{[2]}(B_2) \end{bmatrix} \boldsymbol{u}^{[2]}}_{\substack{rank=2 \\ \text{desired signal}}} + \begin{bmatrix} z^{[2]}(1) \\ z^{[2]}(2) \\ z^{[2]}(3) \end{bmatrix}, \tag{3.5}
$$

where $\boldsymbol{0}$ is a 1×2 zero vector. Consider user 1: Equation (3.4) reveals that interference from user 2 is aligned in one-dimensional subspace along vector $[1, 0, 1]^T$, leaving a two-dimensional subspace for the designed signal. It is also noted that the third row of the desired signal is zero. Therefore, interference from user 2 can be zero-forced by taking a linear combination of the received signal in the first time slot and the third slot as follows:

$$
\tilde{\boldsymbol{y}}^{[1]} = \begin{bmatrix} y^{[1]}(1) - y^{[1]}(3) \\ y^{[1]}(2) \end{bmatrix} = \underbrace{\begin{bmatrix} \boldsymbol{h}^{[1]}(B_1) \\ \boldsymbol{h}^{[1]}(B_2) \end{bmatrix}}_{\tilde{\boldsymbol{H}}^{[1]}} \boldsymbol{u}^{[1]} + \begin{bmatrix} z^{[1]}(1) - z^{[1]}(3) \\ z^{[1]}(2) \end{bmatrix}, \tag{3.6}
$$

where $\tilde{\boldsymbol{H}}^{[1]}$ is a post-processed 2×2 MIMO-like channel matrix obtained by user 1.

Equation (3.5) shows similar results for user 2, and its interference-free signal is obtained by taking a linear combination of received signals at the first and second time slots, as follows:

$$\tilde{\boldsymbol{y}}^{[2]} = \begin{bmatrix} y^{[2]}(1) - y^{[2]}(2) \\ y^{[2]}(3) \end{bmatrix} = \underbrace{\begin{bmatrix} \boldsymbol{h}^{[2]}(B_1) \\ \boldsymbol{h}^{[2]}(B_2) \end{bmatrix}}_{\tilde{\boldsymbol{H}}^{[2]}} \boldsymbol{u}^{[2]} + \begin{bmatrix} z^{[2]}(1) - z^{[2]}(2) \\ z^{[2]}(3) \end{bmatrix}. \tag{3.7}$$

Using the BIA method, two users obtain a total of 4 DoFs (2 DoFs for each user) through a *Super Symbol* of the length of 3 time slots, and thus 4/3 normalized DoF is achievable in this case. Notice that throughout the BIA procedure, no CSIT is required. However, there is enhancement in noise (see (3.6) and (3.7)).

3.3.2   K-User $N_t \times 1$ MISO BC

From the 2-user 2×1 case, it is noted that the *Super Symbol* (Figure 3.2) contains the information about the number of symbol extensions (time slots) used for data transmission, the staggered beampattern switching manner for each user, and precoding matrices for individual users. Therefore, for the general K-user $N_t \times 1$ MISO BC, we summarize construction of the *Super Symbol* [27]. With this, the BIA procedure is ready.

1) Alignment Block

Before presenting the construction method of the *Super Symbol*, we first give the definition of the *Alignment Block* [27], which is the building unit in the *Super Symbol* used to guarantee that inter-user interference can be aligned into a reduced subspace. Take the *Super Symbol* of the 2-user 2×1 MISO BC as an example (see Figure 3.2): the *Alignment Blocks* of individual users are arranged orthogonal to each other in time, which makes the interference alignment possible.

For the K-user $N_t \times 1$ MISO BC, without loss of generality, we consider user 1. An *Alignment Block* for user 1 consists of N_t time slots. At each time slot, user
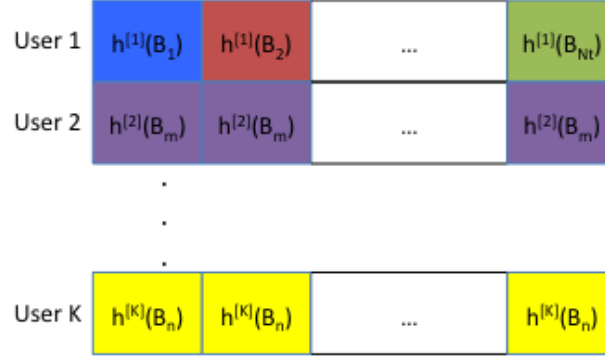
FIGURE 3.3: Alignment Block for user 1 in the K-user $N_t \times 1$ MISO BC.

1 switches its beampattern, so that it goes through N_t beampatterns across an *Alignment Block*. In the meantime, other users (user 2, user 3, $\cdots$ user K) do not switch their beampatterns. Thus, across one *Alignment Block* of user 1, other users listen to N_t transmissions through the same channel. The *Alignment Block* defined for user 1 is shown in Figure 3.3. The *Alignment Blocks* for other users are designed in the same way as that for user 1.

As mentioned earlier, one $N_t \times N_t$ matrix stocked in the precoding matrix is set to be an $N_t \times N_t$ identity matrix $\boldsymbol{I}_{N_t}$, when its corresponding symbol belongs to the *Alignment Block*. For user 1, its signals, transmitted through one *Alignment Block*, are thus given as

$$
\begin{bmatrix} \boldsymbol{s}(1) \\ \boldsymbol{s}(2) \\ \vdots \\ \boldsymbol{s}(N_t) \end{bmatrix} = \begin{bmatrix} \boldsymbol{I}_{N_t} \\ \boldsymbol{I}_{N_t} \\ \vdots \\ \boldsymbol{I}_{N_t} \end{bmatrix}_{N_t^2 \times N_t} \begin{bmatrix} u_1^{[1]} \\ u_2^{[1]} \\ \vdots \\ u_{N_t}^{[1]} \end{bmatrix}. \tag{3.8}
$$

That is, user 1's N_t independent data symbols $u_n^{[1]}, n \in \{1, \cdots, N_t\}$ are repeated N_t times.

Consequently, received signals at user 1 across one *Alignment Block* are (ignoring the noises)

$$
\begin{bmatrix} y^{[1]}(1) \\ y^{[1]}(2) \\ \vdots \\ y^{[1]}(N_t) \end{bmatrix} = \begin{bmatrix} \boldsymbol{h}^{[1]}(B_1) & \boldsymbol{0} & \cdots & \boldsymbol{0} \\ \boldsymbol{0} & \boldsymbol{h}^{[1]}(B_2) & \cdots & \boldsymbol{0} \\ \boldsymbol{0} & \boldsymbol{0} & \ddots & \boldsymbol{0} \\ \boldsymbol{0} & \boldsymbol{0} & \cdots & \boldsymbol{h}^{[1]}(B_{N_t}) \end{bmatrix}_{N_t \times N_t^2} \begin{bmatrix} \boldsymbol{I}_{N_t} \\ \boldsymbol{I}_{N_t} \\ \vdots \\ \boldsymbol{I}_{N_t} \end{bmatrix}_{N_t^2 \times N_t} \begin{bmatrix} u_1^{[1]} \\ u_2^{[1]} \\ \vdots \\ u_{N_t}^{[1]} \end{bmatrix}
$$

$$
= \underbrace{\begin{bmatrix} \boldsymbol{h}^{[1]}(B_1) \\ \boldsymbol{h}^{[1]}(B_2) \\ \vdots \\ \boldsymbol{h}^{[1]}(B_{N_t}) \end{bmatrix}}_{rank = N_t} \begin{bmatrix} u_1^{[1]} \\ u_2^{[1]} \\ \vdots \\ u_{N_t}^{[1]} \end{bmatrix}. \tag{3.9}
$$

It is observed that the N_t data streams cast a N_t-dimensional shadow at receiver 1, and thus N_t DoFs are achievable using one *Alignment Block*.

Now, consider the interference at other users, $k \in \{2, 3, \cdots, K\}$ caused by user 1 through the *Alignment Block*:

$$
\begin{bmatrix} y^{[k]}(1) \\ y^{[k]}(2) \\ \vdots \\ y^{[k]}(N_t) \end{bmatrix} = \begin{bmatrix} \boldsymbol{h}^{[k]}(B_n) & \boldsymbol{0} & \cdots & \boldsymbol{0} \\ \boldsymbol{0} & \boldsymbol{h}^{[k]}(B_n) & \cdots & \boldsymbol{0} \\ \boldsymbol{0} & \boldsymbol{0} & \ddots & \boldsymbol{0} \\ \boldsymbol{0} & \boldsymbol{0} & \cdots & \boldsymbol{h}^{[k]}(B_n) \end{bmatrix}_{N_t \times N_t^2} \begin{bmatrix} \boldsymbol{I}_{N_t} \\ \boldsymbol{I}_{N_t} \\ \vdots \\ \boldsymbol{I}_{N_t} \end{bmatrix}_{N_t^2 \times N_t} \begin{bmatrix} u_1^{[1]} \\ u_2^{[1]} \\ \vdots \\ u_{N_t}^{[1]} \end{bmatrix}
$$

$$
= \underbrace{\begin{bmatrix} \boldsymbol{h}^{[k]}(B_n) \\ \boldsymbol{h}^{[k]}(B_n) \\ \vdots \\ \boldsymbol{h}^{[k]}(B_n) \end{bmatrix}}_{rank = 1} \begin{bmatrix} u_1^{[1]} \\ u_2^{[1]} \\ \vdots \\ u_{N_t}^{[1]} \end{bmatrix}. \tag{3.10}
$$

Since user k's channel state is kept fixed across the *Alignment Block*, the effective channel matrix given in (3.10) has $rank = 1$. Therefore, symbols intended for user 1 are aligned into 1-dimensional reduced subspace at other users. Moreover, it is noticeable that they are aligned along the N_t-dimensional vector $[1, 1, \cdots, 1]^T$, regardless of the channel values.

The *Alignment Block* is shown as the key to achieving interference alignment. Therefore, it is used as the building block for the *Super Symbol*. In other words, the goal is to construct *Alignment Blocks* for individual users in the *Super Symbol*. It is observed that, for the 2-user 2×1 MISO BC case, there is only one *Alignment Block* for each user, and they are constructed in an interleaving way. Specifically, the first two symbols constitute the *Alignment Block* for user 1, while the first and third symbols constitute the *Alignment Block* for user 2. However, in the general K-user $N_t \times 1$ MISO BC, each user may exploit more than one *Alignment Block*.

2) Super Symbol Structure

In the K-user $N_t \times 1$ MISO BC, more than one *Alignment Block* is required for each user. Therefore, the *Super Symbol* structure is more complicated, as it is constructed by interleaving users' *Alignment Blocks*. According to the idea of interference alignment (that is, the signals should be designed to achieve overlapping shadows at the receivers where they constitute interference while remaining distinct at the receivers where they are desired [73]), two problems should be solved in the design of the *Super Symbol*.

The first is the alignment problem, which can be solved by constructing each user's *Alignment Blocks* in a non-overlapping manner. The second problem concerns the linear independence issues, including the linear independence between the desired signals, and the linear independence between the desired signals and interference. For the linear independence between desired signals, it is demonstrated (see Equation (3.9)) that one user's desired signals transmitted through an *Alignment Block* are linearly independent. Thus, the linear independence between desired signals transmitted through different *Alignment Blocks* can be guaranteed by constructing them as non-overlapping in time. On the other hand, the linear independence of the desired signals and interference can be achieved by designing each user's last symbol of one *Alignment Block* to be orthogonal to other users' last symbols of their *Alignment Blocks*. Therefore, the *Super Symbol* is divided into two blocks (referred to as Block 1 and Block 2), where Block 1 is designed to solve the alignment problem, while Block 2 is designed to avoid overlapping between the desired

signals and interference from other users. Details of the design of the *Super Symbol* structure are given in the following two steps.

Step 1: Design of Block 1: For the K-user $N_t \times 1$ MISO BC, each user has a total of $(N_t - 1)^{K-1}$ *Alignment Blocks*, and in Block 1 only the first $N_t - 1$ symbols of an *Alignment Block* are used. Therefore, Block 1 is comprised of $(N_t - 1)^K$ symbols. We would like to remind readers that, across one *Alignment Block*, the desired user's channel state changes at each symbol while other undesired users' channels are kept fixed.

In Block 1, each user's channel state, which is related to beampattern switching at the receiver, is designed to be changed in a periodic manner, where one period is referred to as a *building block*. The *building block* for user $k, k \in \mathcal{K}$ is given in Figure 3.4. It is observed that the *building block* for user k is further divided into $N_t - 1$ sub-blocks of the length of $(N_t - 1)^{k-1}$ symbols each. Therefore, user k's *building block* has a total of $(N_t - 1)^k$ symbols. The channel state is kept the same in a sub-block while it is changed from one sub-block to another, where in the n-th sub-block the channel values are associated with the n-th beampattern, $n \in \{1, 2, \cdots, N_t - 1\}$. By repeating the *building block*, each user can construct its own temporal correlation signature in Block 1. Specifically, user k repeats its *building block* $(N_t - 1)^{K-k}$ times. In this way, Block 1 of the length of $(N_t - 1)^K$ symbols is designed for each of the K users.
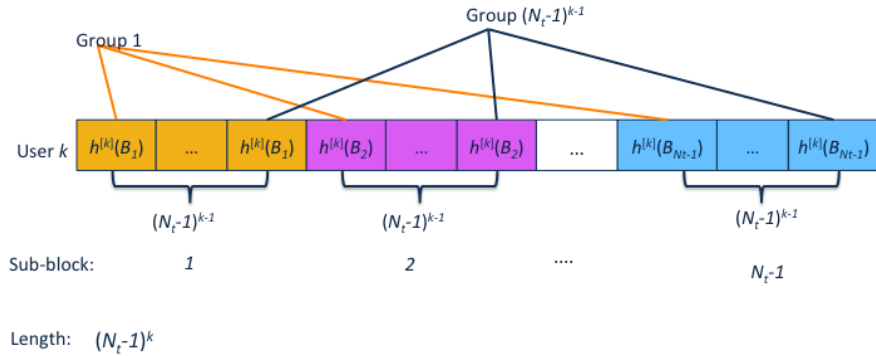
FIGURE 3.4: Building block for user k's Block 1 in K-user $N_t \times 1$ MISO BC.

Step 2: Design of Block 2: Since the first $N_t - 1$ symbols of one *Alignment Block* of each user are used in Block 1, each symbol in Block 2 serves as the last symbol to create the *Alignment Blocks* by grouping with the symbols in Block 1. Recall that each user has $(N_t - 1)^{K-1}$ *Alignment Blocks*, and thus a total of $K(N_t - 1)^{K-1}$ symbols are required for K users in Block 2.

In order to determine the channel values in Block 2, symbols in Block 1 should be first divided into $(N_t - 1)^{K-1}$ groups to create $(N_t - 1)^{K-1}$ *Alignment Blocks* with the last symbols provided in Block 2 for each user. Again, the channel state of the desired user changes at each symbol over an *Alignment Block*, and channels in different sub-blocks within a *building block* are different. Therefore, a group can be constructed by including one symbol from each of the sub-blocks within a *building block*. Consider user k: since there are $(N_t - 1)^{k-1}$ symbols in one sub-block, a total of $(N_t - 1)^{k-1}$ groups can be constructed using symbols in one *building block* (Figure 3.4). Such grouping is repeated through user k's $(N_t - 1)^{K-k}$ *building blocks*.

Then the channel values in Block 2 can be determined as follows. First, Block 2 is divided into K sub-blocks, with a length of $(N_t - 1)^{K-1}$ each. In the k-th sub-block, the symbols serve as the last symbols for user k's *Alignment Blocks*, wherein user k's channel values are equal to $\boldsymbol{h}^{[k]}(B_{N_t})$. For all other users j, $j \in \{1, 2, \cdots, k-1, k+1, \cdots, K\}$, their channel values in the $(N_t - 1)^{K-1}$ symbols should remain fixed, and they are determined to be equal to that of the first symbol of their corresponding groups given in Block 1.

Combining Blocks 1 and 2, the *Super Symbol* structure with the length of $(N_t - 1)^K + K(N_t - 1)^K$ is achieved. There are $(N_t - 1)^{K-1}$ *Alignment Blocks* for each user, and thus each user can achieve $N_t(N_t - 1)^{K-1}$ DoFs by transmitting N_t data streams through these *Alignment Blocks*. Finally, the normalized DoF of the system with K users over the *Super Symbol* is $\frac{KN_t(N_t-1)^{K-1}}{(N_t-1)^K + K(N_t-1)^{K-1}} = \frac{N_t K}{N_t + K - 1}$.

With the *Super Symbol* structure, precoding matrices for K users are straightforward to obtain. In the 2-user 2×1 MISO BC case, there is only one *Alignment Block* for each user, and thus there is one column in the precoding matrix of one

user. However, in the K-user $N_t \times 1$ MISO BC case, there are $(N_t - 1)^{K-1}$ *Alignment Blocks* for each user, and thus there are $(N_t - 1)^{K-1}$ column blocks in the precoding matrix for one user. For each user's precoding matrix, each column block is obtained by stacking the $N_t \times N_t$ identity matrix at the symbol instant belonging to its corresponding *Alignment Block*, otherwise stacking the $N_t \times N_t$ zeros matrix.

3) Example: Two-User 4×1 MIMO BC

Here, the specific case with $K = 2$ and $N_t = 4$ is used as an example to show the *Super Symbol* construction described above. First, consider Block 1 comprised of $(N_t - 1)^K = 9$ symbols. The *building blocks* of users 1 and 2 are given in Figure 3.5 (a). Then, Block 1 is obtained by user 1 repeating its *building block* $(N_t - 1)^{K-1} = 3$ times and user 2 repeating its *building block* $(N_t - 1)^{K-2} = 1$ time (see Figure 3.5 (b)). In Figure 3.5, the different colors are used to represent different channel values for each user. It is noted that, for simplicity, the same colors are used for both user 1 and user 2; however, this does not mean that user 1 and 2 achieve the same channel value. Next, the symbols in Block 1 are divided into 3 groups to create 3 *Alignment Blocks* for each user (see Figure 3.5 (b)). It is observed that in each group the channel of the desired user changes at each of 3 time slots, while the channel of the undesired user is kept the same, satisfying the requirement of the *Alignment Block*.

Then, consider Block 2 comprised of $K(N_t - 1)^{K-1} = 6$ symbols. Block 2 is divided into 2 sub-blocks with 3 symbols each. In the first sub-block, we provide user 1's last symbols of its *Alignment Blocks*: that is, during the 3 time slots user 1's channel values are equal to $\boldsymbol{h}^{[1]}(B_4)$. For user 2, we find the first time slot of each of user 1's groups in Block 1, then set user 2's 3 symbols in the first sub-block to be equal to that at the found time slots. Similarly, in the second sub-block, we provide user 2's last symbols of its *Alignment Blocks*. For user 1, its symbols are set to be equal to that at the first time slots of each of user 2's groups in Block 1. Figure 3.6 shows the designed *Super Symbol* for the 2-user 4×1 MISO BC by combining Block 1 and Block 2.

(a) Building blocks
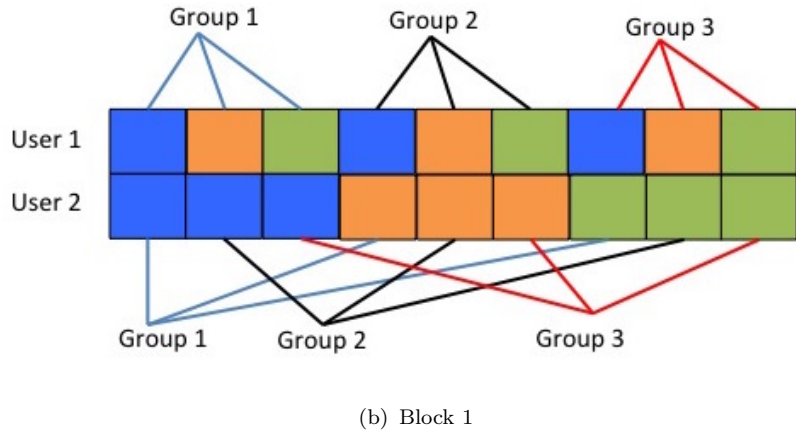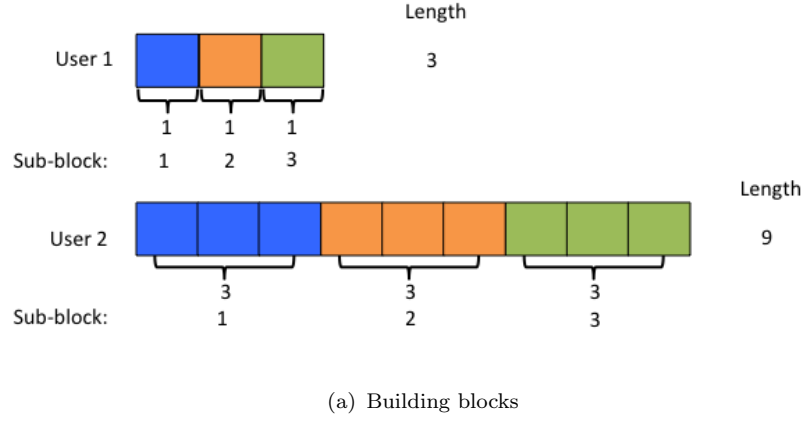
(b) Block 1

FIGURE 3.5: Block 1 for the example of 2-user 4×1 MISO BC.
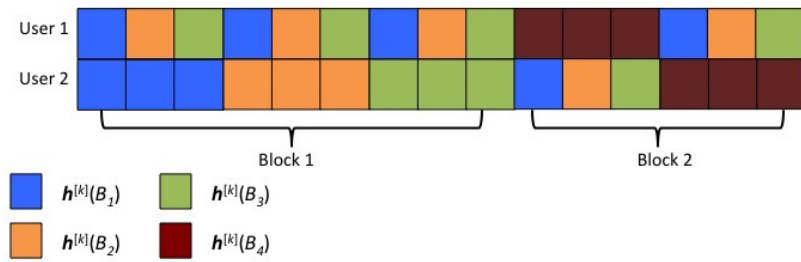
FIGURE 3.6: The *Super Symbol* structure for 2-user 4×1 MISO BC.

According to the *Super Symbol*, precoding matrices for users 1 and 2 are obtained straightforwardly, with 3 column blocks corresponding to 3 *Alignment Blocks*

61

each:

$$
\underbrace{\begin{bmatrix}
\mathbf{I}_4 & \mathbf{0}_4 & \mathbf{0}_4 \\
\mathbf{I}_4 & \mathbf{0}_4 & \mathbf{0}_4 \\
\mathbf{I}_4 & \mathbf{0}_4 & \mathbf{0}_4 \\
\mathbf{0}_4 & \mathbf{I}_4 & \mathbf{0}_4 \\
\mathbf{0}_4 & \mathbf{I}_4 & \mathbf{0}_4 \\
\mathbf{0}_4 & \mathbf{I}_4 & \mathbf{0}_4 \\
\mathbf{0}_4 & \mathbf{0}_4 & \mathbf{I}_4 \\
\mathbf{0}_4 & \mathbf{0}_4 & \mathbf{I}_4 \\
\mathbf{0}_4 & \mathbf{0}_4 & \mathbf{I}_4 \\
\mathbf{I}_4 & \mathbf{0}_4 & \mathbf{0}_4 \\
\mathbf{0}_4 & \mathbf{I}_4 & \mathbf{0}_4 \\
\mathbf{0}_4 & \mathbf{0}_4 & \mathbf{I}_4 \\
\mathbf{0}_4 & \mathbf{0}_4 & \mathbf{0}_4 \\
\mathbf{0}_4 & \mathbf{0}_4 & \mathbf{0}_4 \\
\mathbf{0}_4 & \mathbf{0}_4 & \mathbf{0}_4
\end{bmatrix}}_{\text{User 1}}
\underbrace{\begin{bmatrix}
\mathbf{I}_4 & \mathbf{0}_4 & \mathbf{0}_4 \\
\mathbf{0}_4 & \mathbf{I}_4 & \mathbf{0}_4 \\
\mathbf{0}_4 & \mathbf{0}_4 & \mathbf{I}_4 \\
\mathbf{I}_4 & \mathbf{0}_4 & \mathbf{0}_4 \\
\mathbf{0}_4 & \mathbf{I}_4 & \mathbf{0}_4 \\
\mathbf{0}_4 & \mathbf{0}_4 & \mathbf{I}_4 \\
\mathbf{I}_4 & \mathbf{0}_4 & \mathbf{0}_4 \\
\mathbf{0}_4 & \mathbf{I}_4 & \mathbf{0}_4 \\
\mathbf{0}_4 & \mathbf{0}_4 & \mathbf{I}_4 \\
\mathbf{0}_4 & \mathbf{0}_4 & \mathbf{0}_4 \\
\mathbf{0}_4 & \mathbf{0}_4 & \mathbf{0}_4 \\
\mathbf{0}_4 & \mathbf{0}_4 & \mathbf{0}_4 \\
\mathbf{I}_4 & \mathbf{0}_4 & \mathbf{0}_4 \\
\mathbf{0}_4 & \mathbf{I}_4 & \mathbf{0}_4 \\
\mathbf{0}_4 & \mathbf{0}_4 & \mathbf{I}_4
\end{bmatrix}}_{\text{User 2}} .
$$

It is clear that with the BIA scheme each user achieves 4 DoFs over one *Alignment Block*, and thus a total of 12 DoFs (over 3 *Alignment Blocks*) are achievable through 15 symbol extensions. Therefore, a normalized DoF of $\frac{N_t K}{N_t + K - 1} = \frac{8}{5}$ can be achieved.

4) Interference Zero-Forcing

Let us first reconsider the case of 2-user 2×1 MISO BC. Its interference zero-forcing step is mathematically described in Equation (3.6). The essence of the interference zero-forcing is the use of interference received over the last symbol (time slot) in each user's *Alignment Block* to cancel interference received in the previous time slots in that *Alignment Block*. Notice that, for the general K-user $N_t \times 1$ MISO BC, each user uses more than one *Alignment Block* to construct the *Super Symbol*. And it is worth recalling that the *Alignment Blocks* of each user are designed to be orthogonal to each other in time. Thus, the interference-free data streams can be decoded *Alignment Block*-wise: that is, one user's N_t data streams transmitted

over an *Alignment Block* are decoded by using only N_t symbols corresponding to that *Alignment block*, while ignoring symbols corresponding to other *Alignment Blocks* of that user.

Without loss of generality, consider the decoding of N_t symbols at user k over one *Alignment Block*. In each of the first $N_t - 1$ symbols of the *Alignment Block*, user k encounters interference from other $K - 1$ users, and the interference is the same in each symbol due to the repeating code used in Block 1. Interference is orthogonal to the desired signal received in the last symbol of the *Alignment Block*, since in the last symbol only the signal of the desired user is transmitted. To zero force the interference in each of the $N_t - 1$ symbols, user k needs to do $K - 1$ subtractions to cancel interference from one of the other users each time. Mathematically, consider the following received signal space over one *Alignment Block*:

$$
\begin{bmatrix}
\begin{bmatrix} \boldsymbol{h}^{[k]}(B_1) \\ \vdots \\ \boldsymbol{h}^{[k]}(B_{N_t-1}) \end{bmatrix} & \boldsymbol{I}_{N_t-1} & \boldsymbol{I}_{N_t-1} & \cdots & \boldsymbol{I}_{N_t-1} \\
\boldsymbol{0}_{(N_t-1)\times N_t} & \boldsymbol{I}_{N_t-1} & \boldsymbol{0}_{N_t-1} & \cdots & \boldsymbol{0}_{N_t-1} \\
\boldsymbol{0}_{(N_t-1)\times N_t} & \boldsymbol{0}_{N_t-1} & \boldsymbol{I}_{N_t-1} & \cdots & \boldsymbol{0}_{N_t-1} \\
\vdots & \vdots & \vdots & \ddots & \vdots \\
\boldsymbol{0}_{(N_t-1)\times N_t} & \boldsymbol{0}_{N_t} & \boldsymbol{0}_{N_t-1} & \cdots & \boldsymbol{I}_{N_t-1} \\
\boldsymbol{h}^{[k]}(B_{N_t}) & \boldsymbol{0}_{1\times(N_t-1)} & \boldsymbol{0}_{1\times(N_t-1)} & \cdots & \boldsymbol{0}_{1\times(N_t-1)}
\end{bmatrix}.
$$

The first column block of N_t dimensions is spanned by the desired signal and the last $K - 1$ column blocks of $N_t - 1$ dimensions are occupied by interference from other users. The interference zero-forcing procedure (i.e., $K - 1$ subtractions) is equivalent to designing a projection matrix that projects the received signals onto a subspace orthogonal to the subspace occupied by interference. The projection matrix is designed as

$$
\mathcal{P} = \begin{bmatrix}
\boldsymbol{I}_{N_t-1} & -\boldsymbol{I}_{N_t-1} & -\boldsymbol{I}_{N_t-1} & \cdots & -\boldsymbol{I}_{N_t-1} & 0 \\
\boldsymbol{0}_{1\times(N_t-1)} & \boldsymbol{0}_{1\times(N_t-1)} & \boldsymbol{0}_{1\times(N_t-1)} & \cdots & \boldsymbol{0}_{1\times(N_t-1)} & 1
\end{bmatrix}_{N_t\times(K(N_t-1)+1)}.
$$

Applying the projection matrix on the received signal over one *Alignment Block*, it is easy to obtain the interference-free signal, taking the following form

$$
\tilde{\boldsymbol{y}}^{[k]} = \underbrace{\begin{bmatrix} \boldsymbol{h}^{[k]}(B_1) \\ \boldsymbol{h}^{[k]}(B_2) \\ \vdots \\ \boldsymbol{h}^{[k]}(B_{N_t}) \end{bmatrix}}_{\tilde{\boldsymbol{H}}^{[k]}} \begin{bmatrix} u_1^{[k]} \\ u_2^{[k]} \\ \vdots \\ u_{N_t}^{[k]} \end{bmatrix} + \tilde{\boldsymbol{z}}, \tag{3.11}
$$

where $\tilde{\boldsymbol{z}} \in \mathbb{C}^{N_t \times 1}$ is the post-processed noise with the covariance matrix of the form of:

$$
\boldsymbol{R}_{\tilde{z}} = \begin{bmatrix} K \cdot \boldsymbol{I}_{N_t-1} & \boldsymbol{0} \\ \boldsymbol{0} & 1 \end{bmatrix}. \tag{3.12}
$$

Therefore, with equal power allocation to every data stream, user k's achievable rate by transmitting N_t data streams over one *Alignment Block* is [27]

$$
C^{[k]'} = \mathbb{E}\left\{ \log \det \left(\boldsymbol{I}_{N_t} + \frac{(K + N_t - 1)P_t}{N_t^2 K} \tilde{\boldsymbol{H}}^{[k]} \tilde{\boldsymbol{H}}^{[k]H} \boldsymbol{R}_{\tilde{z}}^{-1} \right) \right\}. \tag{3.13}
$$

Since each user uses $(N_t - 1)^{K-1}$ *Alignment Blocks* in the case of K-user $N_t \times 1$ MISO BC and thus a total of $(N_t - 1)^K + K(N_t - 1)^{K-1}$ time slots (symbol extensions) in the *Super Symbol*, the normalized rate for user k is [27]

$$
\begin{aligned}
C^{[k]} &= \frac{(N_t - 1)^{K-1}}{(N_t - 1)^K + K(N_t - 1)^{K-1}} \mathbb{E}\left\{ \log \det \left(\boldsymbol{I}_{N_t} + \frac{(K + N_t - 1)P_t}{N_t^2 K} \tilde{\boldsymbol{H}}^{[k]} \tilde{\boldsymbol{H}}^{[k]H} \boldsymbol{R}_{\tilde{z}}^{-1} \right) \right\} \\
&= \frac{1}{N_t + K - 1} \mathbb{E}\left\{ \log \det \left(\boldsymbol{I}_{N_t} + \frac{(K + N_t - 1)P_t}{N_t^2 K} \tilde{\boldsymbol{H}}^{[k]} \tilde{\boldsymbol{H}}^{[k]H} \boldsymbol{R}_{\tilde{z}}^{-1} \right) \right\}.
\end{aligned} \tag{3.14}
$$

Finally, the normalized sum-rate achieved by the K-user $N_t \times 1$ MISO BC using the BIA scheme is calculated as [27]

$$
C = \sum_{k=1}^{K} \frac{1}{N_t + K - 1} \mathbb{E}\left\{ \log \det \left(\boldsymbol{I}_{N_t} + \frac{(K + N_t - 1)P_t}{N_t^2 K} \tilde{\boldsymbol{H}}^{[k]} \tilde{\boldsymbol{H}}^{[k]H} \boldsymbol{R}_{\tilde{z}}^{-1} \right) \right\}. \tag{3.15}
$$

3.3.3 Constant Transmit Power Allocation

Although the original BIA scheme described above shows an optimal DoF achievable in the multi-user MISO BC scenario without CSIT, the DoF cannot be translated to rate gains in the low SNR region, due to the noise amplification emerging in the interference zero-forcing step. This will be illustrated via a numerical example later. To reduce the enhanced noise power level, the power allocation methods have been developed in [76]. The main idea of the proposed power allocation methods is to adjust the relative transmit power allocated to symbols in Blocks 1 and 2 of the *Super Symbol*. In the original BIA scheme the equal transmit power is allocated to all data streams transmitted through Blocks 1 and 2.

This work considers the *Constant Transmit Power Allocation* scheme [76], which is the simplest and also an efficient method. To present such a scheme, we also take the case of 2-user 2×1 MISO BC for an example, and it is easy to extend this approach to the general K-user $N_t \times 1$ MISO BC. The transmission strategy of the original BIA uses equal transmit power allocation, represented in Equation (3.3). It is observed that the transmit power in time slot 1 ($\boldsymbol{s}(1)$) is double that in the time slots 2 and 3 ($\boldsymbol{s}(2)$ and $\boldsymbol{s}(3)$). In the constant transmit power allocation scheme, appropriately scaling relative power allocated for symbols in Blocks 1 and 2 ensures that the same transmit power is allocated in all time slots. Mathematically, this is [76]

$$\begin{bmatrix} \boldsymbol{s}(1) \\ \boldsymbol{s}(2) \\ \boldsymbol{s}(3) \end{bmatrix} = \begin{bmatrix} \frac{1}{\sqrt{2}}\boldsymbol{I}_2 \\ \boldsymbol{I}_2 \\ \boldsymbol{0}_2 \end{bmatrix} \boldsymbol{u}^{[1]} + \begin{bmatrix} \frac{1}{\sqrt{2}}\boldsymbol{I}_2 \\ \boldsymbol{0}_2 \\ \boldsymbol{I}_2 \end{bmatrix} \boldsymbol{u}^{[2]}. \tag{3.16}$$

Substitute the above transmission strategy in Equation (3.4), and then user 1's received signals over a *Super Symbol* are as follows:

$$\begin{bmatrix} y^{[1]}(1) \\ y^{[1]}(2) \\ y^{[1]}(3) \end{bmatrix} = \begin{bmatrix} \frac{1}{\sqrt{2}}\boldsymbol{h}^{[1]}(B_1) \\ \boldsymbol{h}^{[1]}(B_2) \\ \boldsymbol{0} \end{bmatrix} \boldsymbol{u}^{[1]} + \begin{bmatrix} \frac{1}{\sqrt{2}}\boldsymbol{h}^{[1]}(B_1) \\ \boldsymbol{0} \\ \boldsymbol{h}^{[1]}(B_1) \end{bmatrix} \boldsymbol{u}^{[2]} + \begin{bmatrix} z^{[1]}(1) \\ z^{[1]}(2) \\ z^{[1]}(3) \end{bmatrix}. \tag{3.17}$$

User 1 can thus take a linear combination of the signal received in the first and third time slots to zero force interference: i.e.,

$$\tilde{\boldsymbol{y}}^{[1]} = \begin{bmatrix} \sqrt{2}y^{[1]}(1) - y^{[1]}(3) \\ y^{[1]}(2) \end{bmatrix} = \underbrace{\begin{bmatrix} \boldsymbol{h}^{[1]}(B_1) \\ \boldsymbol{h}^{[1]}(B_2) \end{bmatrix}}_{\tilde{\boldsymbol{H}}^{[1]}} \boldsymbol{u}^{[1]} + \begin{bmatrix} \sqrt{2}z^{[1]}(1) - z^{[1]}(3) \\ z^{[1]}(2) \end{bmatrix}. \quad (3.18)$$

From (3.18), user 1 obtains the interference-free 2×2 MIMO-like channel $\tilde{\boldsymbol{H}}^{[1]}$, similar to the result derived by the original BIA scheme. Again, user 2 can obtain the same result. Thus, using the constant transmit power allocation scheme, the system can also achieve 4/3 DoF.

As a consequence, the normalized sum-rate for such a system with the general value of N_t and K is given by (proof details can be found in [76])

$$C = \sum_{k=1}^{K} \frac{1}{N_t + K - 1} \mathbb{E}\left\{ \log \det \left(\boldsymbol{I}_{N_t} + \frac{P_t}{N_t} \tilde{\boldsymbol{H}}^{[k]} \tilde{\boldsymbol{H}}^{[k]H} \boldsymbol{R}_{\tilde{z}}^{-1} \right) \right\}, \quad (3.19)$$

where

$$\boldsymbol{R}_{\tilde{z}} = \begin{bmatrix} (2K - 1) \cdot \boldsymbol{I}_{N_t-1} & \boldsymbol{0} \\ \boldsymbol{0} & 1 \end{bmatrix}. \quad (3.20)$$

3.4 ESPAR Beamforming for Implementation of BIA

From the BIA scheme reviewed in the previous section, it is clear that the antenna mode (beampattern) switching at the receiver is the key, unless its DoF benefits will not be achieved. As previously mentioned, beampattern switching might be an easier way to fulfil the BIA scheme (compared to frequency switching and polarization switching). Moreover, it is well known that directional beampattern helps to improve receive SNR by spatial filtering. Therefore, beampattern switching could provide a solution to improving performance of the BIA by reducing the noise amplification level.

The single-RF ESPAR antenna provides a practical solution to beampattern switching at the receiving end for the BIA scheme, since its beampattern is controlled by simply tuning a few easy-to-implement reactance values loaded to parasitic elements. The target of this work is the beampattern design to realize and even improve the BIA scheme. Notice that, as requirements of the BIA, the ESPAR beamforming here is required to provide $N_t(N_t > 1)$ beampatterns at one channel realization (across one *Super Symbol*), unlike the common beamforming where only one beampattern is usually needed. We would emphasize that the receive antenna beamforming at each user is operated in a distributed and uncoordinated way; therefore, in this section, we drop the user index for notation simplicity.

3.4.1 Discussions on the BIA Scheme

Before proposing the ESPAR beamforming strategies, we first discuss some aspects of the BIA scheme related to the channel states generated from the receive antenna mode switching and also the noise amplification problem. Although the beampattern of the ESPAR antenna will be employed to realize the BIA scheme in our work, here we discuss these aspects of the BIA via a simple numerical example using the genetic channel vectors: entries of channel vectors are drawn from a continuous distribution, as is generally assumed in the literature [3, 27, 76]. These examples can provide insights into the beampattern design of the ESPAR antenna for the BIA scheme.

1) Channel Fluctuation Patterns

It is observed from the *Super Symbol* structure (Figures 3.2 and 3.6) that the channel fluctuation patterns created by the receive beampattern switching are critical in the BIA scheme. Recall that it is assumed that the coherence times are long enough to ensure constant channel state across a *Super Symbol*: i.e., $\boldsymbol{G}$ in (3.1) is kept constant. According to (3.1), an ESPAR receiver can only switch between N_t beampatterns defined by $\boldsymbol{w}_n, n \in \{1, \cdots, N_t\}$ to manually create different channel vectors $\boldsymbol{h}(B_n)$. If the assumption of the coherent time does not

hold, a user will see different channel vectors when the same beampattern is formed in different time slots in the *Super Symbol*. Thus, interference from other users cannot be aligned into a reduced subspace. From now on, the above assumption is made throughout this work.

Now, we will consider some numerical examples, examining rate performance of the original BIA scheme (given in (3.15)) under three channel state situations resulting from receive antenna switching. The three situations are listed as follows:

a) The receive beampattern switching fails to create channel diversity, i.e., $\boldsymbol{h}(B_1) = \boldsymbol{h}(B_2) = \cdots = \boldsymbol{h}(B_{N_t})$;

b) The receive beampattern switching results in N_t i.i.d channel vectors $\boldsymbol{h}(B_n), n \in \{1, \cdots, N_t\}$ – an ideal situation usually assumed in the literature;

c) The receive beampattern switching results in channel vectors having the relations $\boldsymbol{h}(B_n) = \gamma_n \cdot \boldsymbol{h}, n \in \{1, \cdots, N_t\}$, where $\boldsymbol{h} \in \mathbb{C}^{N_t \times 1}$ is the vector with elements drawn from i.i.d Gaussian variables with zero-mean and unity variance, and γ_n is a scalar, which may be considered as different but correlated channel vectors.

These examples are depicted in Figure 3.7, where every simulated point is averaged from 1000 Monte-Carlo experiments, and elements of $\boldsymbol{h}(B_1)$, $\boldsymbol{h}$, and only $\boldsymbol{h}(B_n), n \in \{2, \cdots, N_t\}$ in situation b are assumed to be uncorrelated Gaussian variables. In these examples, the single-user MISO BC is used as the baseline for comparison. From the examples, one can make observations as follows.

When the receive beampattern switching fails to provide different channel vectors (situation a), DoFs of the BIA scheme collapse, and its rate is even lower than that of the single-user setting, since in the BIA scheme more time-frequency resources (more time slots) are used to transmit information data to users than with the TDMA technique.

If the i.i.d channel vectors have been achieved (situation b), the BIA scheme achieves the DoF benefits as expected. Study of the DoFs in varying networks is
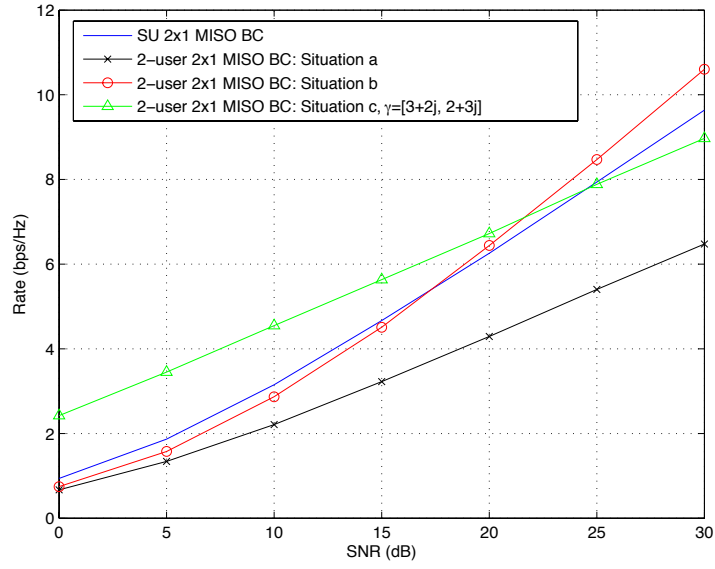
(a) 2-user 2x1 MISO BC
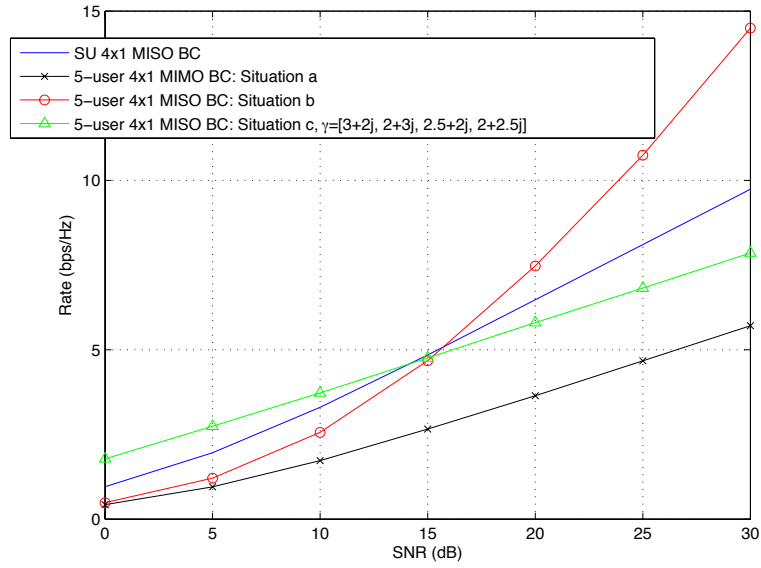
(b) 5-user 4x1 MISO BC

FIGURE 3.7: Original BIA performances in different channel state situations resulting from receive antenna switching.

commonly based on the i.i.d fading model. Many studies on the BIA scheme also assume that the ideal i.i.d channel vectors are associated with different antenna modes. However, if the practical beampattern switching is taken into account at the receiver, it is not necessary for the resulting channel vectors to be identically independent to each other. In this case, the study on the network DoF is intriguing,

and thus we may consider that the DoFs derived from the i.i.d channel vectors are the outer bounds.

Under situation c, it is shown that, when the SNR is lower than 24 dB for the 2-user 2×1 MISO BC and lower than 15 dB for the 5-user 4×1 MISO BC, the BIA outperforms the single-user setting. However, the BIA is inferior to the single-user MISO BC in the high SNR region. The improvement in the low/moderate SNR region mainly results from the increase in the received power (γ_n). Indeed, the facts of the poor performance in the high SNR region and the improvement reduction with larger value of N_t and K demonstrate that, in situation c, the DoFs of the original BIA scheme cannot be translated to rage gains due to channel correlation.

The example suggests that the beampattern design in the ESPAR array is optimal to provide sufficient uncorrelated channel vectors, and receive SNR enhancement can also improve performance, especially in the low/moderate SNR region.

2) Noise Amplification

Next, we examine the noise amplification aspect of BIA. This can be observed from Figure 3.7. Consider the ideal case with i.i.d channel vectors (situation b), where it shows that, if SNR is lower than around 17 dB (for the 2-user 2×1 MISO BC) or 15.5 dB (for the 5-user 4×1 MISO BC), then BIA will lose its superiority to the single-user MISO BC.

One solution to reducing the effects of noise amplification is the power allocation method presented previously. Figure 3.8 illustrates the comparison between the original BIA with equal power allocation to all symbols and that with constant transmit power allocation. The improvement with the use of constant transmit power allocation has been shown, especially with increasing N_t and K. Specifically, the cross point between the multi-user setting and the single-user setting moves from around 15 dB to 7 dB for $N_t = 2, K = 2$. In the case of $N_t = 4, K = 5$, the rate loss is negligible in the low SNR region. However, the benefits of the use of constant transmit power allocation may not be sufficient in the case with small N_t and K. Indeed, the BIA scheme is more suited to the case with small values of
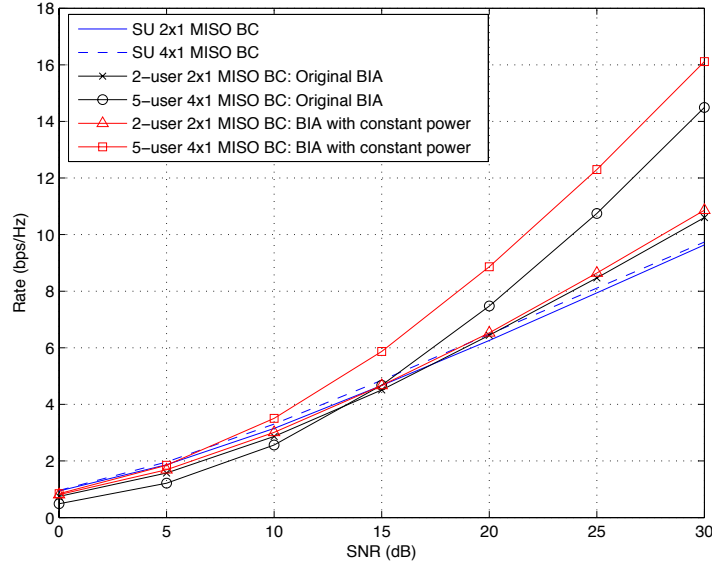
FIGURE 3.8: Comparison between the original BIA and the BIA using constant transmit power allocation.

N_t and K, since the assumption of coherence time is more practical for the *Super Symbol* with shorter length. This suggests that to further improve performance of the BIA, the directional beamforming of the receive antenna should be taken into account.

3.4.2 ESPAR Beamforming for BIA scheme

The above discussions suggest that ESPAR beamforming for BIA schemes should provide N_t different beampatterns at a channel realization (across one *Super Symbol*). Specifically, the resulting channel vectors $\boldsymbol{h}(B_n), n \in \{1, \cdots, N_t\}$ are optimal to be generic (uncorrelated) or they are able to provide SNR gains. To this end, we propose three beamforming methods for the ESPAR array to implement BIA, which may also improve the BIA scheme. In [77–79], the ESPAR antenna has been studied for the BIA scheme, where only sector beampatterns have been exploited, and the studies have been restricted 2-user 2×1 MISO BC.

1) Random Beampattern Method

The channel vectors associated with N_t beampatterns are optimal to be sufficiently uncorrelated (generic) vectors. Since the channel state ($\boldsymbol{G}$ in (3.1)) is kept constant across a *Super Symbol*, the generic channel vectors should be achieved by forming different beampatterns at the receiver. In this context, we may consider that beampatterns formed at one receiver are randomly generated. With this method, the channels seen by the receiver are sufficiently uncorrelated: that is, they are drawn from continuous distribution (not guaranteed to follow the Gaussian distribution). We refer to this method as the *random beampattern method*.

It is known that the beampattern of an ESPAR antenna is controlled by tuning a few analog values loaded to parasitic elements (see Equations (2.6) and (2.7)). Thus, we design each of N_t random beampatterns, by that each reactance load, $x_m \in \{1, \cdots, M\}$, is randomly selected from the variable values uniformly distributed in a practical range; e.g., $[-300, 300](\Omega)$. Store the N_t sets of randomly selected loading values $\hat{\boldsymbol{x}}_n, n \in \{1, \cdots, N_t\}$, and then they are used across a *Super Symbol* according to the BIA scheme. Until the next *Super Symbols*, the random beamforming procedure is repeated.

The random beampattern method is quite simple and is able to provide sufficiently uncorrelated channel vectors for the BIA scheme. However, the beampatterns are formed by randomly selecting reactance loads; therefore they do not take into account beamshapes to increase the receive SNR. Consequently, this beamforming method is unable to improve performance of BIA by suppressing noise amplification. On the other hand, due to the rich scattering propagation model, the use of random beampatterns is feasible. The reason is that a random beampattern nulls out signals from multiple paths with a sufficiently small probability. Moreover, the random beampattern method is ready to be employed in a system with larger values of N_t and K.

2) Sector Beampattern Selection

The random beampattern method is quite simple; however, the issue of BIA related to noise amplification has not been solved. The noise amplification problem may hinder the application of the BIA scheme in a practical network: for example, cellular systems. Thus, we consider a method that exploits different directional beampatterns to reduce the noise enhancement level. The central idea is that a fixed number of directional beampatterns are designed in advance (at the design stage), and then each receiver dynamically selects N_t appropriate beampatterns out of all pre-designed ones.

Recall that an ESPAR array with $M+1$ elements is able to form M sector beampatterns accessing one sector of whole angle space each (Chapter 2, Section 2.3). Let $\mathcal{B}_s = \{B_{s,1}, \cdots, B_{s,M}\}$ denote the set of all potential sector beampatterns that are designed in advance, and their corresponding reactance loads are stored, where $M \geq N_t$.

For one user in the K-user $N_t \times 1$ MISO BC, it is required to dynamically select N_t beampatterns out of the set $\mathcal{B}_s$ across one *Super Symbol*. The beampattern selection decision is made based on the estimated receive power of each sector beampattern. In particular, a receiver selects N_t sector beampatterns with the largest receive powers: that is,

$$B_{s,1}^{\star} = arg \max_{B_{s,m} \in \mathcal{B}_s} P_r(B_{s,m}),$$

$$\vdots \tag{3.21}$$

$$B_{s,N_t}^{\star} = arg \max_{B_{s,m} \in \tilde{\mathcal{B}}_s} P_r(B_{s,m}),$$

where $B_{s,n}^{\star}, n \in \{1, \cdots, N_t\}$ represents the n-th selected beampattern, $\tilde{\mathcal{B}}_s$ is the subset of $\mathcal{B}_s$ by removing the previously selected beampatterns, $P_r(B_{s,m})$ is the receive power when sector beampattern $B_{s,m}$ is formed.

The simplest way to implement the beampattern selection is that a user periodically scans all M sector beampatterns $\mathcal{B}_s$ and evaluates corresponding receive powers. It is noted that due to space limits on mobile terminals, the number of

parasitic elements M, thus the number of achievable sector beampatterns, cannot be large. Therefore, exhaustive searching throughout all sector beampatterns is practical in this system. During a *Super Symbol*, each user performs the beampattern selection and stores N_t sets of corresponding loading values for the BIA scheme, until the next *Super Symbols*. This beamforming method is available for the BIA system with an arbitrary value of K, since the beampattern selection is operated individually at one user. However, there is a limit on the number of transmit antennas, i.e., $N_t \leq M$.

3) SVD-Based Beamforming

In this section, exploiting estimate channel coefficient at receiver to operate ESPAR adaptive beamforming. In the BIA scheme, we assume that perfect CSIR is available. Indeed, the acquiring CSIR is more nature than acquiring CSIT, since the receiver directly observes the signals transmitted through the channel.

SVD beamforming is a common and simple approach to improve system rate, widely used in MIMO networks where the conventional multiple active antenna arrays are used. We would like to exploit it in the EPSAR array to implement the BIA scheme. However, SVD beamforming cannot be directly applied to the ESPAR array, due to the unique configuration of an ESPAR antenna.

First, in the ESPAR array only signal impinging on the active element can be observed and processed, while signals impinging on parasitic elements cannot be observed, but they are electronically combined to the single-RF front-end. Secondly, there is a nonlinear relation between the beampattern and the reactance loads of parasitic elements. To this end, we develop a two-step beamforming strategy based on the SVD beamformer and exploiting the GA (presented in Chapter 2).

Step 1: The SVD beamformer aims to calculate weights based on the channel matrix estimated by the receiver. In a conventional MIMO system with multiple antenna arrays, the receiver estimates channels between transmit antennas and receive antennas, straightforwardly using measurements derived from individual

antenna elements. At an ESPAR receiver, since only signal impinging on the active element can be observed, a MIMO-like channel matrix containing spatial signature of the channels cannot be estimated. Therefore, in the ESPAR array, it is not capable of directly designing the equivalent weight vector $\boldsymbol{w}$ by applying the SVD beamformer to outputs of its individual elements. In this context, the RD technique, which is a signal processing method usually applied for the antenna array with a single-RF front-end [43, 53, 57], is used to obtain a MIMO-like channel matrix analogous to that achievable in conventional antenna arrays.

Specifically, in the RD technique, an ESPAR antenna forms $N_i(N_i \geq N_t)$ initial beampatterns, $\Phi_n(\theta), n \in \mathcal{I} = \{1, \cdots, N_i\}$ on a time division basis, where the same information signal is sent. The initial beampatterns are fixed and known. Using the RD technique, signals received by an ESPAR receiver over N_i initial beampatterns are represented by the N_i-dimensional vector $\boldsymbol{y}$:

$$\boldsymbol{y} = \begin{bmatrix} \boldsymbol{h}(\Phi_1) \\ \vdots \\ \boldsymbol{h}(\Phi_{N_i}) \end{bmatrix} \boldsymbol{s} + \begin{bmatrix} z_1 \\ \vdots \\ z_{N_i} \end{bmatrix} = \boldsymbol{H}_\Phi \boldsymbol{s} + \boldsymbol{z}, \qquad (3.22)$$

where $\boldsymbol{H}_\Phi \in \mathbb{C}^{N_i \times N_t}$ denotes the MIMO-like channel matrix obtained by the RD technique, in which the (i,j)-th entry is the channel coefficient between the i-th initial beampattern formed by the receive ESPAR and the j-th antenna at the transmitter. We assume that $\boldsymbol{H}_\Phi$ is known at the receiver. The vector $\boldsymbol{z} \in \mathbb{C}^{N_i \times 1}$ contains noises corrupted at individual initial beampatterns, and they are assumed to be uncorrelated across the initial beampatterns. Perform singular value decomposition of the channel matrix $\boldsymbol{H}_\Phi$, then one has

$$\boldsymbol{H}_\Phi = \boldsymbol{U} \boldsymbol{\Sigma} \boldsymbol{V}^H, \qquad (3.23)$$

where unitary matrices $\boldsymbol{U} \in \mathbb{C}^{N_i \times N_i}$ and $\boldsymbol{V} \in \mathbb{C}^{N_t \times N_t}$ respectively contain eigenvectors of $\boldsymbol{H}_\Phi \boldsymbol{H}_\Phi^H$ and $\boldsymbol{H}_\Phi^H \boldsymbol{H}_\Phi$, $\boldsymbol{\Sigma} \in \mathbb{R}^{N_i \times N_t}$ is a diagonal matrix with $rank(\boldsymbol{\Sigma}) = \min(N_i, N_t) = N_t$ dominant singular values in a descending order as diagonal entries.

In the BIA K-user $N_t \times 1$ MISO BC system, N_t different beampatterns are required. Thus, the SVD beamformer applies the first N_t column vectors of $\boldsymbol{U}$, denoted by $\boldsymbol{U}_{1:N_t}$, to the received signal vector in (3.22). $\boldsymbol{U}_{1:N_t}$ contains N_t singular vectors corresponding to the N_t dominant singular values. The output of the SVD beamformer is expressed as the following $N_t \times 1$ vector

$$\boldsymbol{y}_{svd} = \boldsymbol{U}_{1:N_t}^H \boldsymbol{y} = \boldsymbol{U}_{1:N_t}^H \boldsymbol{H}_\Phi \boldsymbol{s} + \boldsymbol{U}_{1:N_t}^H \boldsymbol{z}, \tag{3.24}$$

where the noises $\boldsymbol{U}_{1:N_t}^H \boldsymbol{z}$ are still AWGNs, since $\boldsymbol{U}$ is a unitary matrix.

Step 2: The problem then turns to how to calculate N_t sets of parasitic reactance loads to form beampatterns approximating the outputs of the SVD beamformer (3.24). As we emphasized previously, there is a nonlinear relation between the beampattern and parasitic reactance loads. To calculate N_t sets of necessary reactance loads, we resort to the GAs; details of the use of GAs for ESPAR beamforming can be found in Chapter 2. Here, we only give the objective function of the SVD-based beamforming problem. To approximate the outputs of the SVD beamformer, the objective function can be set as the CCC between the outputs of the SVD beamformer $\boldsymbol{y}_{svd}$ and the achievable output of the ESPAR antenna y. Mathematically, it is written as

$$\max f(x_1, \cdots, x_M) = \frac{\mathbb{E}\{y \boldsymbol{y}_{svd}^*(i)\}}{\sqrt{\mathbb{E}\{y y^*\} \mathbb{E}\{\boldsymbol{y}_{svd}(i) \boldsymbol{y}_{svd}^*(i)\}}}, \quad i \in \{1, \cdots, N_t\}, \tag{3.25}$$

where $\boldsymbol{y}_{svd}(i)$ is the i-th element of outputs of the SVD beamformer.

Consequently, using the GA, each receiver can obtain N_t sets of reactance loads for N_t beampatterns approaching outputs of the SVD beamformer. Then, they are used across a *Super Symbol* according to the BIA scheme, until the next *Super Symbols*.

3.5 CSI Estimation Overheads

The greatest benefit of the BIA scheme is the reduction of CSIT overheads while achieving the optimal DoF in the multi-user MISO BC. However, the majority of studies on the multi-user MIMO techniques do not take into account the CSI cost, when the performance evaluation is operated. In order to make a fair comparison between CSIT-based multi-user MIMO techniques and the novel BIA scheme using the ESPAR antenna, in this section we present the CSI (including CSIT and CSIR) cost for a given technique.

In this work, the LZFBF technique [71, 80, 81], which is a simple and common technique exploiting the CSIT to simultaneously transmit data streams to multiple users, is studied as the exemplary CSIT-based MIMO BC transmission scheme for comparison with the BIA scheme. For the LZFBF technique, perfect CSIT is always assumed.

3.5.1 Linear Zero-Forcing Beamforming

In the LZFBF technique, the goal of the beamforming (here digital beamforming, as mentioned in Chapter 2) is to separate users' streams with different beamforming directions, by exploiting available knowledge of CSI. For ease of explanation and for comparison with the BIA scheme, we assume that each user is equipped with a single antenna (it can be the ESPAR antenna due to a single-RF chain), so that the study focuses on the multi-user MISO BC. Moreover, we also assume that $K \leq N_t$ users are simultaneously served by the system.

Let $u^{[k]}$, $\hat{\boldsymbol{v}}^{[k]} \in \mathbb{C}^{N_t \times 1}$ and $P_t^{[k]}$ be, respectively, the information data (single stream), beamforming vector and transmit power scaling factor for user k, $k \in \{1, \cdots, K\}$. The channel between user k and the N_t transmit antennas is denoted by the vector $\boldsymbol{h}^{[k]} \in \mathbb{C}^{1 \times N_t}$, and thus let $\boldsymbol{H} = [\boldsymbol{h}^{[1]T}, \boldsymbol{h}^{[2]T}, \cdots, \boldsymbol{h}^{[K]T}]^T$ denote the system channel matrix by storing channel vectors of all K users as rows. Similarly,

let the $N_t \times K$ matrix $\hat{\boldsymbol{V}} = [\hat{\boldsymbol{v}}^{[1]}, \hat{\boldsymbol{v}}^{[2]}, \cdots, \hat{\boldsymbol{v}}^{[K]}]$ store all K users' beamforming vectors as columns. The signal received by user k is thus given by (dropping the time index for simplicity, since there is no symbol extension in this technique)

$$y^{[k]} = \underbrace{\boldsymbol{h}^{[k]}\hat{\boldsymbol{v}}^{[k]}u^{[k]}}_{\text{Desired signal}} + \underbrace{\sum_{j=1, j\neq k}^{K} \boldsymbol{h}^{[k]}\hat{\boldsymbol{v}}^{[j]}u^{[j]}}_{\text{Interference}} + z^{[k]}, \tag{3.26}$$

where the beamforming vector for each user is unit-norm, i.e., $\|\hat{\boldsymbol{v}}^{[j]}\| = 1, \forall j$.

According to the zero-forcing criterion, the beamforming vector $\hat{\boldsymbol{v}}^{[k]}$ for user k is designed to project $\boldsymbol{h}^{[k]}$ onto the nullspace of $\{\boldsymbol{h}^{[j]}\}_{j\neq k}$: i.e.,

$$\boldsymbol{h}^{[k]}\hat{\boldsymbol{v}}^{[j]} = \boldsymbol{0}, \quad \forall k \neq j, \quad 1 \leq j, k \leq K. \tag{3.27}$$

One easy way to achieve the beamforming matrix $\hat{\boldsymbol{V}}$ under the zero-forcing condition (3.27) is to use the pseudoinverse of $\boldsymbol{H}$, taking the following form:

$$\hat{\boldsymbol{V}} = \boldsymbol{H}^\dagger = \boldsymbol{H}^H(\boldsymbol{H}\boldsymbol{H}^H)^{-1}. \tag{3.28}$$

Using LZFBF and assuming that the transmit power is allocated equally to each of the K users, the signal received by user k is therefore reduced to

$$y^{[k]} = \boldsymbol{h}^{[k]}\hat{\boldsymbol{v}}^{[k]}u^{[k]} + z^{[k]}. \tag{3.29}$$

Finally, the sum-rate achievable for this system is

$$C_{ZF} = \sum_{k=1}^{K} \mathbb{E}\left\{\log\left(1 + \frac{P_t}{KN_t}|\boldsymbol{h}^{[k]}\hat{\boldsymbol{v}}^{[k]}|^2\right)\right\}. \tag{3.30}$$

3.5.2 CSI Estimation and Pilot Costs

Consider a frequency-division duplex (FDD) system using multi-user MIMO techniques. To obtain knowledge of CSIT, first, each user is required to estimate
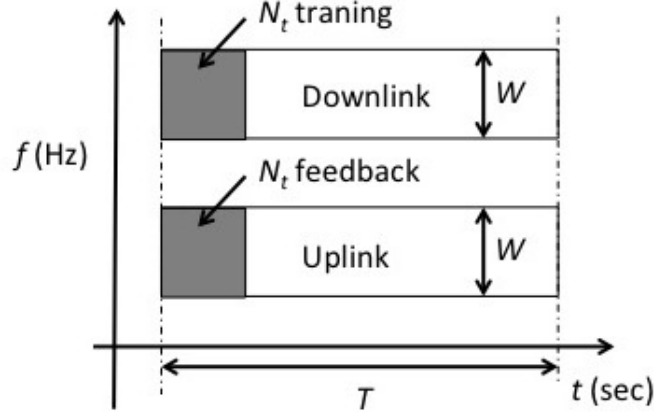
FIGURE 3.9: CSI training and feedback overheads in the FDD system [2].

CSI-based downlink estimation pilots (EPs) transmitted by the BS (transmitter); secondly, users quantize the estimated channel coefficients and then these are fed back via the uplink channel. In addition, dedicated pilot symbols are inserted in training symbols to provide CSIR for coherence detecting (CD) by users [3].

In [2], the authors analyzed the pilot symbol overhead and its effect on the net throughput through a dimensionality count of the resources per time-frequency block that is used for CSI estimation (Figure 3.9). Let ρ_{csi}, ρ_{cd} denote the fraction of the total downlink transmit resource used for EPs per transmit antenna, and for CD per user, respectively. And let ρ_{fd} be the fraction of the total transmit resource used to re-allocate to the uplink supporting the uplink feedback per user per transmit antenna. Thus, overheads related to the EPs, CD and feedback are given by $\Pi_1 \rho_{csi}$, $\Pi_2 \rho_{cd}$ and $\Pi_3 \rho_{fd}$, where $\Pi_i, i = \{1, 2, 3\} \geq 0$ and they are specified at a given system implementation. Here, we consider the multi-user MISO BC using the LZFBF and BIA schemes. Following the discussions in [3], the CSI overheads are summarized in Table 3.1 for the given techniques. Notice that for the ESPAR-based BIA schemes using the random beamforming and sector-beam selection approach, their CSI overheads are the same as those presented for the original BIA scheme. However, for the ESPAR-based BIA scheme using SVD beamforming, the CSI overheads should be N_i times that of the original BIA.

TABLE 3.1: Summary of CSI overheads [3]

Type	LZFBF	Original BIA	ESPAR-based BIA (SVD)
EPs	$N_t\rho_{csi}$	0	0
FB	$K\rho_{fb}$ to $KN_t\rho_{fb}$	0	0
CD	$K\rho_{cd}$	$N_t\rho_{cd}$ to $(N_t)^2\rho_{cd}$	$N_tN_i\rho_{cd}$ to $(N_t)^2N_i\rho_{cd}$

3.6 Simulations

In this section, we evaluate the performance of the proposed BIA schemes employing the ESPAR antenna as a solution to beampattern switching. A comparison between the ESPAR-based BIA and LZFBF is also provided: the metric is the sum-rates calculated by (3.19) and (3.30), respectively. The result of each point is averaged from 1000 Monte-Carlo simulations. In the propagation environment, suppose that there are $N_{sc} = 20$ scatterers.

The transmit antenna array is assumed to be an N_t-element ULA of a $\lambda/2$ inter-element spacing. The simulated ESPAR antenna is composed of $M + 1 = 7$ thin electrical dipoles with a length of $\lambda/2$ each. The inter-element spacing is set to $\lambda/4$. EPSAR's mutual impedance matrix $\boldsymbol{Z}$ is as the same given in Chapter 2, Section 2.4.

We first consider the performance of the BIA schemes using three proposed ESPAR beamforming approaches, without consideration of the CSI overheads. In the following simulations, the single-user MISO BC is considered as the baseline for comparison. It is noted that for fair comparison, in the single-user MISO BC, the ESPAR antenna is also adopted as the receive antenna, and omni-directional beampattern is formed by the ESPAR receive antenna.

To randomly generate N_t different beampatterns across a *Super Symbol*, each receive ESPAR randomly selects N_t sets of reactance loads $\hat{\boldsymbol{x}}_n, n = \{1, \cdots, N_t\}$, in which each element $x_m, m = \{1, \cdots, 7\}$ is uniformly drawn from the practical range $[-300, 300](\Omega)$ with the resolution 1 Ω. The N_t selected reactance loads are then stored and used across the *Super Symbol*, until the next *Super Symbols*.
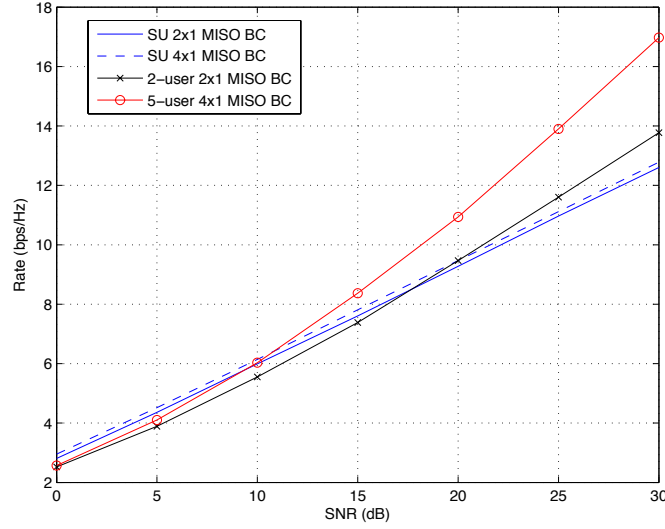
FIGURE 3.10: Simulated results of ESPAR-based BIA with receive antenna switching between random beampatterns.

Figure 3.10 shows sum-rates achieved by the BIA scheme exploiting random beam-patterns of the receive ESPAR antenna across a *Super Symbol*, compared to that of the single-user MISO BC. From the simulated results, we can believe that the use of random beampatterns provides sufficiently uncorrelated channel vectors for one user, since the rate gains achieved by the BIA scheme are larger than that achieved by the single-user MISO BC in the high SNR region. That is, the SNR is larger than 17.5 dB for the 2-user 2×1 MISO, and 10 dB for the 5-user 4×1 MISO BC. This tendency is similar to the numerical example discussed in Section 3.4 (situation b). However, without delicate design on the beamshape for the random beampatterns, the ESPAR-based BIA does not show its benefits in the low SNR region. Figure 3.10 also suggests that rate gains provided by the BIA increase with larger values of N_t and K, where the cross point moves to 10 dB when K increases to 5 and N_t increases to 4. Although performance of the BIA with the random beamforming method may loss its superiority in the low SNR region as the same as the original BIA scheme [27], this beamforming method is simple and with low computational complexity, and it is ready to be extended to the BIA system with the arbitrary values of K and N_t.

The 6 sector beampatterns of a 7-element ESPAR antenna are pre-designed.
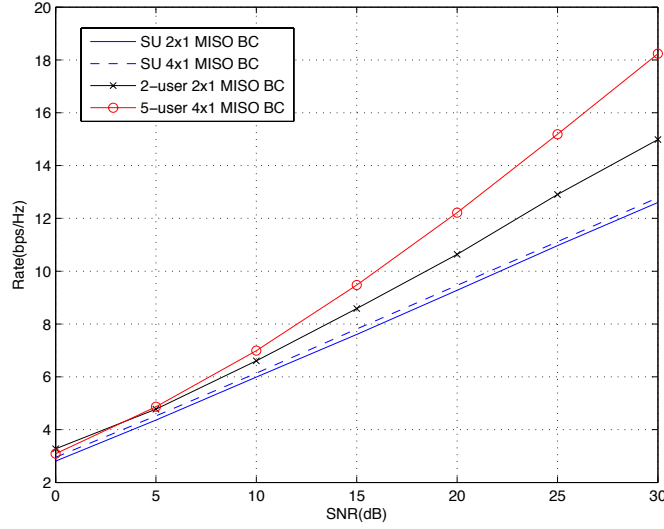
FIGURE 3.11: Simulated results of ESPAR-based BIA with receive antenna switching between dynamically selected sector beampatterns.

Firstly, optimize values of reactance loads $\hat{\boldsymbol{x}}_1 = [x_1, \cdots, x_6]$ to maximize the beam gain to the look direction $0°$. The optimized values are $x_1 = 23.38, x_2 = 41.43, x_3 = -205.09, x_4 = -205.09, x_5 = 41.43, x_6 = 23.38$. Then, the remaining 5 sector beampatterns are obtained circularly shifting elements of $\hat{\boldsymbol{x}}_1$. As there are only 6 sector beampatterns, it is practical for each user to scan all sector beampatterns to identify the $N_t \leq 6$ beampatterns with the largest receive powers.

As shown in Figure 3.11, with the use of sector beampatterns dynamically selected by each receiver, the BIA scheme outperforms the single-user MISO BC over all SNR values, since the directional beampatterns increase the receive SNR. Moreover, rate gains of the BIA with increasing N_t and K are observed over almost all the SNR values, where the loss in the low SNR region is negligible. However, it is clear that this beampattern design method is suited to MISO BC with the number of transmit antennas not exceeding the number of available sector beampatterns.

To operate SVD-based beamforming, an ESPAR receiver first uses a fixed number of initial beampatterns to obtain the estimate of a MIMO-like channel matrix $\boldsymbol{H}_\Phi$ derived from outputs of the initial beampatterns. Here, we simply use the 6 sector beampatterns given above as the initial beampatterns. The conventional SVD beamformer uses $\boldsymbol{H}_\Phi$ to calculate weights applied to outputs of the initial

beampatterns. Finally, N_t sets of necessary reactance loads are optimized by the GAs, where the outputs of the SVD beamformer are used as the reference signals. The parameters for the GA are the same as those summarized in Table 2.1 in Chapter 2.

Figure 3.12 depicts the sum-rates obtained by the BIA using SVD-based beamforming, where we can see that the rate performance of the BIA is superior to that of the single-user MISO BC over most of the SNR region. For the multi-user MISO BC with $N_t = 2$ transmit antennas, the BIA scheme provides large rate gains compared to the achievable rate of the single-user MISO BC over the whole SNR region. However, when the number of transmit antennas increases to $N_t = 4$, rate gains provided by the BIA scheme do not show until the SNR is higher than 5 dB. And the benefit of the BIA with large N_t does not shown until 17 dB. The reason may be that, by increasing the number of transmit antennas N_t, the BIA requires more beampatterns designed by SVD-based beamforming, and SVD-based beamformer designs beampatterns by adaptively weighting outputs of the fixed number of initial beampatterns ($N_i = 6$ here). Given a number of initial beampatterns, when N_t is smaller, a user benefits from more flexible beamforming. If we can provide more initial beampatterns in SVD-based beamforming, the benefits of the BIA may be also shown in the low and moderate SNR region when $N_t = 4$. However, increasing the number of initial beampatterns is not practicable, since CSI overheads and complexity are increased (this will be discussed later). Therefore, SVD-based beamforming is more suitable for the system with a small number of transmit antennas.

Finally, comparing results given in Figures 3.10, 3.11 and 3.12, it is observed that the BIA with SVD-based beamforming outperforms that with random beamforming and sector beampattern selection for the 2-user 2×1 MISO BC; however, when $N_t = 4$, its superiority is shown when SNR is larger than around 13 dB. When the computation complexity is considered, the sector beampattern selection method is a better solution, which can also provide rate gains over most of the SNR region, by enhancing receive SNR.
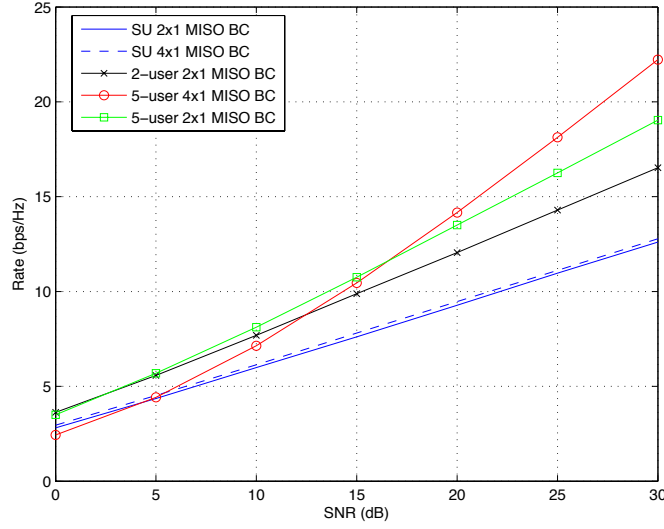
FIGURE 3.12: Simulated results of ESPAR-based BIA with received antenna switching between beampatterns designed based on SVD beamformer.

Next, we compare the performance of the ESPAR-based BIA schemes to that of the LZFBF technique using perfect CIST. For the LZFBF technique, the transmitter is also equipped with N_t-element ULA while each receive is equipped with a 7-element ESPAR, which forms the omni-directional beampattern, as that is assumed for the single-user MISO BC, for fair comparison.

Figure 3.13 (a), (b) and (c) depict the sum-rates achieved by the LZFBF, compared to that of the BIA schemes exploiting three ESPAR beamforming methods respectively, where the simulations do not take into account the CSI overheads. It is not surprising that the rate performance of LZFBF is superior to that of the BIA schemes. Moreover, in the BIA scheme the transmitter can simultaneously serve $K \geq N_t$ users; however, there is a constraint on the number of users $K \leq N_t$ for the LZFBF. From the figures, we can observe that, when the number of users increases to 10, the sum-rates achieved by BIA schemes are higher than those achieved by the LZFBF. In the simulations, it is also seen that, when $K \geq 10$ no significant rate gains are shown in the considered SNR region (i.e., $[0, 30]$ (dB)) compared to the case with $K = 10$. In other words, the BIA scheme could benefit in rate gain with larger values of $K(K \geq 10)$ only when higher transmit power is used. It is suggested that, in a fixed SNR region and given a fixed number of
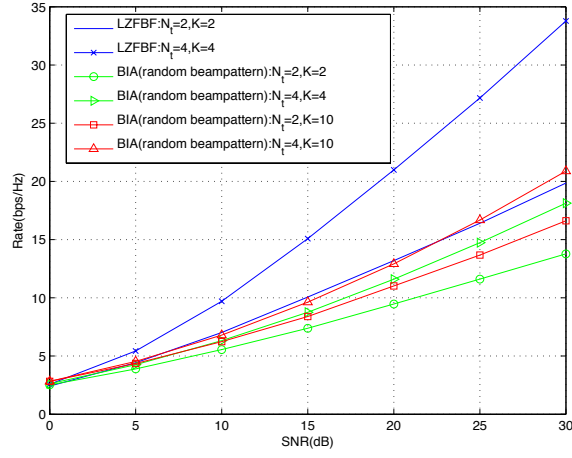
(a) Random beampattern method
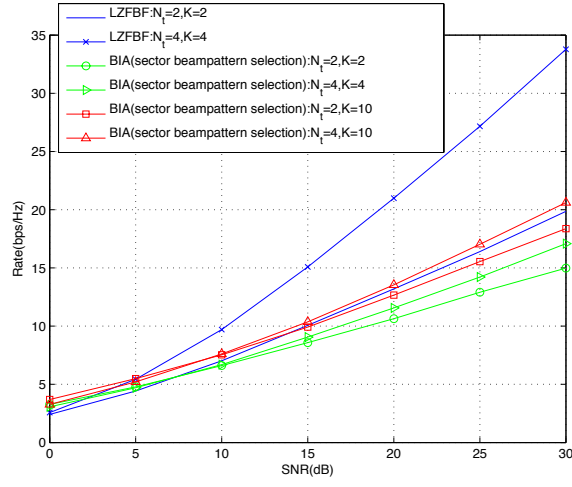
(b) Sector beampattern selection
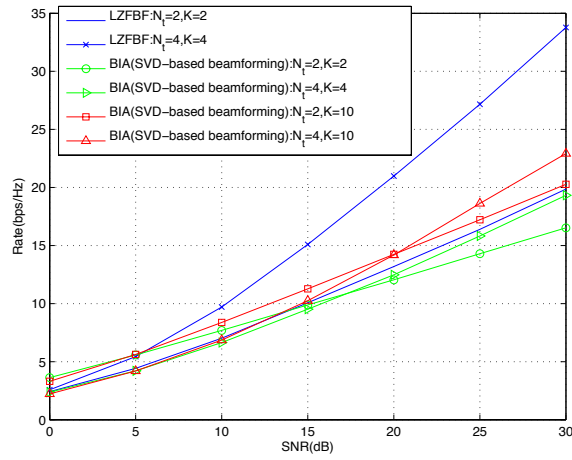
(c) SVD-based beamforming

FIGURE 3.13: Rate performance comparison between LZFBF and ESPAR-based BIA schemes without considering CSI overheads.

transmit antennas, there is a threshold for the number of active users for the BIA system; by exceeding that threshold, the DoFs do not lead to a higher achievable rate.

Indeed, the benefits of the BIA scheme result from the reduction of CSIT overhead, so that the above comparisons (Figure 3.13) are not fair. Therefore, we consider both CSIT and CSIR overheads in the performance comparison between the LZFBF and ESPAR-based BIA schemes. As presented in previous discussions (summarized Table 3.1), two cases are referred to as "OHL" (optimistic CSI overheads) and "OHU" (pessimistic CSI overheads). In particular, for the LZFBF, the overhead cost ratio is $N_t\rho_{cis} + K\rho_{fb} + K\rho_{cd}$ under OHL, and $N_t\rho_{csi} + KN_t\rho_{fb} + K\rho_{cd}$ under OHU; for the ESPAR-based BIA, the overhead cost ratio is $N_t\rho_{cd}$ (or $N_tN_i\rho_{cd}$) under OHL, and $(N_t)^2\rho_{cd}$ (or $(N_t)^2N_i\rho_{cd}$) under OHU. When the CSI overheads are considered, the net-rate of a given scheme (i.e., the LZFBF or ESPAR-based BIA) is the rate without CSI overheads times one minus corresponding overhead cost ratio [2].

Figure 3.14 (a), (b) and (c) show the simulated net-rates of the LZFBF and ESPAR-based BIA employing three proposed beamforming methods for the multi-user 2×1 MISO BC, with $\rho_{csi} = \rho_{cd} = 1\%$ and two distinct ρ_{fd} values 1% and 3%. It is observed that, in the OHL case, the BIA schemes with sector beampattern selection and SVD-based beamforming are superior to the LZFBF in the low SNR region for the system with $K = 2$ users, while the superiority is observed over most of the SNR region when the user number increases to $K = 10$. However, the rate gain of the BIA with random beampatterns is almost negligible. Moreover, the figures reveal that, for BIA schemes with random beampattern method and sector beampattern selection, there is no significant difference between the rate performances under OHL and OHU. Nevertheless, a large rate loss is observed by the BIA scheme with SVD-based beamforming and LZFBF under OHU, suggesting the importance of the CSI overhead designs in both schemes.

Figure 3.15 (a), (b) and (c) depict simulated results for the multi-user 4×1 MISO BC, with the same settings in Figure 3.14. As the figures show, when CSI

overheads are taken into account, net-rates achieved by the BIA schemes with the random beampattern method and sector beampattern selection approach to those achieved by the LZFBF, and they are even superior to the LZFBF in the OHU case with large feedback costs ($\rho_{fd} = 3\%$). However, for the BIA scheme with SVD-based beamforming, its rate gains are lost (especially in the OHU case), suggesting that CSI overhead design is critical to SVD-based beamforming, due to the penalty of the use of the RD technique for channel matrix estimation.

(a) Random beampattern method
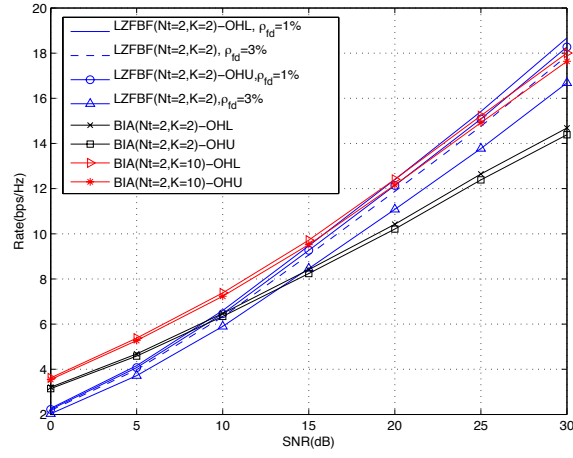
(b) Sector beampattern selection
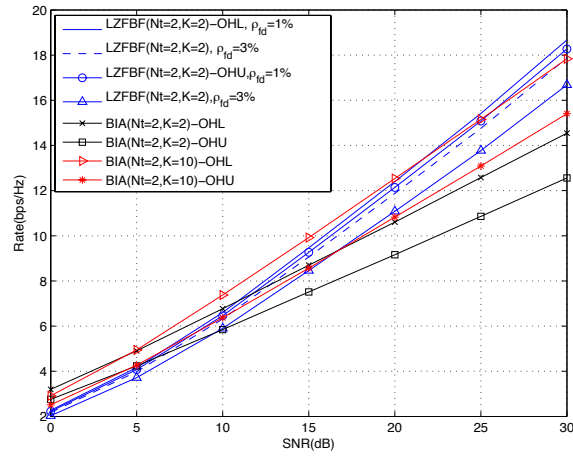
(c) SVD-based beamforming

FIGURE 3.14: Rate performance comparison between LZFBF and ESPAR-based BIA schemes taking CSI overheads into account for the 2×1 MISO BC.
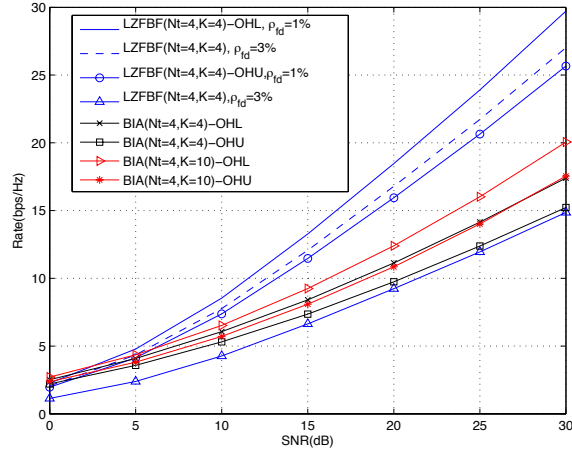
(a) Random beampattern method
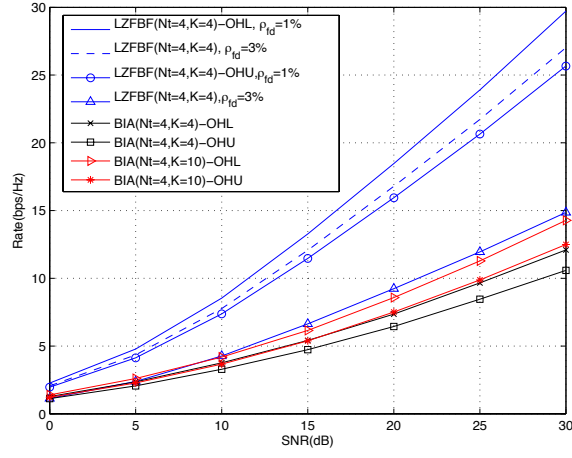
(b) Sector beampattern selection
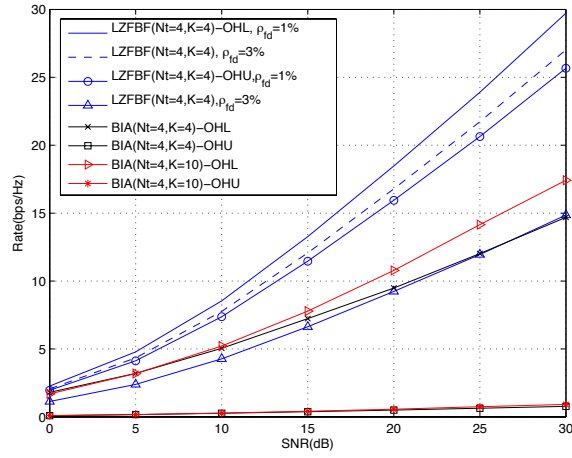
(c) SVD-based beamforming

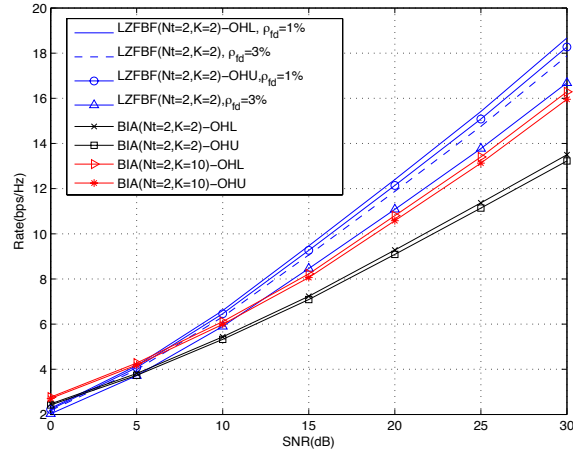FIGURE 3.15: Rate performance comparison between LZFBF and ESPAR-based BIA taking CSI overheads into account for the 4×1 MISO BC.

89

3.7 Summary

In this chapter, we made the first attempt to implement the BIA, using the ES-PAR antenna for the beam switching at the receiving end. First, the general idea of the BIA [27] is simply reviewed. In our work, the key is how to design the required number of beampatterns to fulfil – and even improve – the BIA. We proposed three beampattern design methods. The first is simply the design of random beampatterns with randomly selected reactance loads for each parasitic element from a practical range. The aim of this beamforming approach is to create mimic generic channel vectors seen by a user. The rate gains observed in the simulations illustrate the feasibility of the use of random beampatterns in BIA. However, it only works well in a high SNR regime, since the noise amplification problem has not been addressed by this method. In the second approach, a user dynamically selects beampatterns with the largest receive powers from a fixed number of pre-designed sector beampatterns. The selected directional beampatterns can improve performance of the BIA, especially in the low SNR region, since the received SNR has been enhanced. The last beamforming method is based on the SVD beamformer: this is achieved by two steps, where first the output of the SVD beamformer is obtained by using a fixed number of initial beampatterns, and then the outputs are used as the reference signal input to the GA algorithm. From the simulation results, SVD-based beamforming algorithms can also provide rate gains, even in the low SNR region. However, with the increase in transmit antennas, the performance of the BIA with SVD-based beamforming is degenerated in low SNR region, which suggests that as required beampatterns increase, more initial beampatterns should be used. Due to the complexity limitation, SVD-based beamforming is more suitable for the MU-MISO case with a small number of transmit antennas. Finally, the ESPAR-based BIA is compared with the CSIT-based LZFBF technique, taking account of CSI overheads, where the achievable sum-rates are comparable to those of the LZFBF technique. These results indicate the importance of CSI overheads design in a practical communication system.

Chapter 4

Interference Mitigation in Small Cell Networks

A recent development in small cell networks is femtocells, also known as home BSs, which are user-installed BSs with short range, low cost and low power [82]. They are introduced for better indoor voice and data communications. Femtocells connect to the service provider's network via a broadband connection such as digital subscriber line, cable modem, or a separate RF backhaul channel. In this chapter, we show the ESPAR antenna as a solution to interference mitigation in femtocell networks, while keeping the system complexity and cost at a relative low level compared to the power control and resource allocation methods. The ESPAR-based techniques presented in the previous chapters will be exploited to achieve the goal of reducing interference among femtocells.

In [83–86], it is suggested that the switched multi-element antenna (single RF-chain) can be deployed at the femto-BS as a means of interference suppression, where one directional beampattern or a combination of beampatterns is dynamically selected to the serving user terminal (UT). It is demonstrated that greater capacity gains are obtained by using direction antennas at the femto-BSs than by using single omni-directional antennas. Based on this, we can expect that the

exploitation of directional antennas at both the femto-BS and UT will lead to further capacity gains. This is an ongoing trend in next-generation systems, with the development of smart antenna technology. Thus, we consider the ESPAR antenna being deployed at both the femto-BSs and UTs, and the beamforming methods presented in Chapter 2 are used to suppress inter-cell interference.

In addition, a small number of antennas may be deployed at femto-BSs, providing a chance for exploiting some promising but more complex methods, such as IA or multi-cell processing, to minimize interference [87] to support a multi-user scenario. In this context, we consider the ESPAR antenna as the receive antenna, and thus the ESPAR-based BIA scheme (presented in Chapter 3) is used for interference management for the multi-user MISO BC in multi-femtocell settings. Indeed, the small cell environment is more suitable for implementing BIA algorithms since the practical issues of IA and the assumptions needed for BIA are ameliorated [88]. Specifically, we would like to remind readers that in the BIA technique given in the last chapter, it is assumed that the channel remains constant during one *Super Symbol* to achieve alignment of inter-user interference. However, if one considers traditional macrocell-based cellular networks, where the BS is equipped with a large number of antennas and serves a large number of users, the length of one *Super Symbol* is designed to exploit many symbol periods. In practice, the assumption of a fixed channel across long periods cannot be held. On the other hand, in the femtocell networks, femto-BSs have fewer transmit antennas and serve only a limited number of users. Therefore, the *Super Symbol* is designed to be much shorter and the fixed channel assumption is more practical.

4.1   System Model

4.1.1   System Architecture

This part of the thesis focuses on residential femtocells. As shown in Figure 4.1, the system has a group of N_{fc} rooms spanning an area of 20×20 square meters
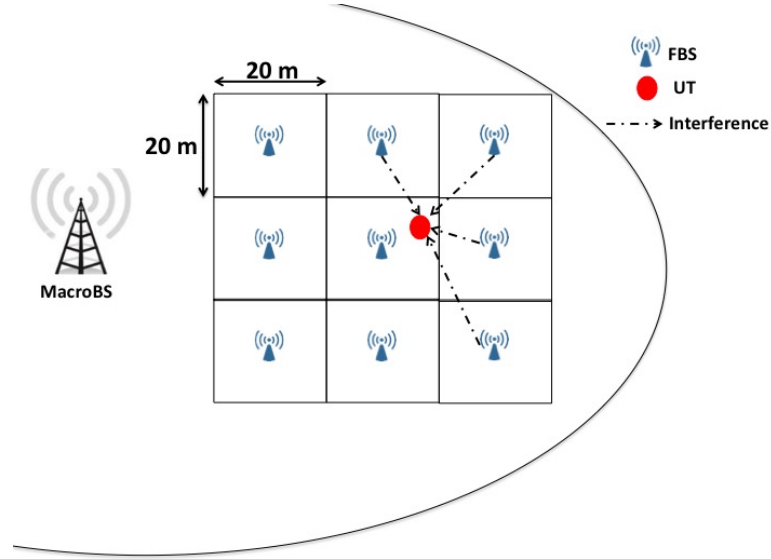
FIGURE 4.1: Femtocell networks architecture.

per room, and they are lying within the coverage of a macrocell. One femto-BS is installed at the center of each room, whose transmit power is adjusted to cover the room. Therefore, a room is a femtocell. All femto-BSs are assumed to be connected to the control unit by the backhaul. It is assumed that each femto-BS simultaneously serves a small number of UTs (up to 2 users here), which are uniformly distributed within a femtocell. In this femtocell system, we consider the exclusive spectrum allocation scheme, which allocates different frequency bands to the macrocell and femtocell. The other scenario is that we may also consider this system as a CR system, where the femtocells work as SUs, while the macrocell is the PU. In the context of the CR, SUs communicate when the PU is silent. Neither the exclusive spectrum scheme nor the CR system results in cross-tier interference (i.e., macrocell-to-femtocell interference). Based on these assumptions, we focus on the interference among femtocells (i.e., co-tier interference).

We further classify this femtocell system by two scenarios based on interferences seen by UTs:

- Scenario 1: The ESPAR antenna is deployed at both the femto-BS and UT. After scheduling, each femto-BS serves one UT randomly located within the room, for a single time slot. Consequently, UTs suffer from inter-cell

interference only. This is the downlink of a single-input-single-output (SISO) system.

- Scenario 2: Each femto-BS is equipped with a 2-element ULA, while each UT is equipped with an ESPAR antenna. After scheduling, each femto-BS simultaneously serves two UTs randomly located within the room, for a single time slot. Consequently, UTs suffer from both intra-cell and inter-cell interferences. This is the multi-user MISO BC system.

4.1.2 Channel Model

For the residential femtocells, we consider a model of indoor wireless channels, taking into account the clustered-wave propagation and detailed environment model. The concept of a clustering phenomenon of impinging waves was first introduced by Saleh and Valenzuela for indoor multipath channels [89]. Their measurements suggest that the multipath channel can be modelled as multiple clusters, each of which is associated with a set of rays.

Spencer et al. [90] extended the work of Saleh and Valenzuela to include the AoA statistics of a cluster in the channel model (see Figure 4.2). In particular, the AoA statistic is expressed by a power angular spread (PAS) which represents the angular distribution of impinging rays within a cluster. The PAS, denoted by $\mathcal{A}(\theta)$, can be parameterized by a mean AoA $(\bar{\theta})$ and an angular spread σ_θ. It was found to closely match the Laplacian distribution, expressed as [91]

$$\mathcal{A}(\theta) = \frac{1}{\sqrt{2}\sigma_\theta} e^{\frac{-\sqrt{2}|\theta - \bar{\theta}|}{\sigma_\theta}}. \tag{4.1}$$

Furthermore, in [92], the authors extended Spencer's model by taking into account the spatial statistics at both receive and transmit sides for the indoor MIMO channel.

In the presence of angular distribution of an impinging wave described by the PAS $\mathcal{A}(\theta)$, the calculation of the directivity gain of an ESPAR antenna is related to
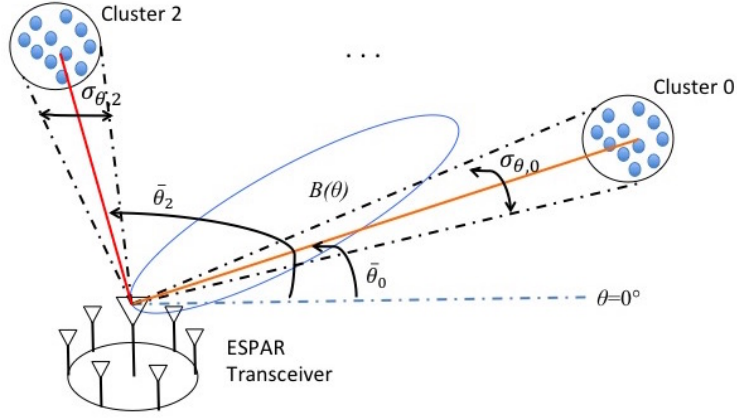
FIGURE 4.2: An illustration of the AoA statistic of clusters impinging on an ESPAR antenna.

compute the distributed directivity gain (DDG), taking the following form [44, 93, 94]

$$G(\theta) = \eta \int_0^{2\pi} g(\theta) \mathcal{A}(\theta - \bar{\theta}), \tag{4.2}$$

where $g(\theta)$ is the normalized directional beampattern, of the form

$$g(\theta) = \frac{|B(\theta)|^2}{\frac{1}{2\pi} \int_0^{2\pi} B(\theta) B(\theta)^* d\theta}. \tag{4.3}$$

For multiple clusters (e.g., two clusters), the PAS can be rewritten as

$$\mathcal{A}(\theta) = \frac{1}{2\sqrt{\sigma_\theta}} \left(e^{-|\sqrt{2}(\theta - \bar{\theta}_0)/\sigma_\theta|} + e^{-|\sqrt{2}(\theta - \bar{\theta}_1)/\sigma_\theta|} \right), \tag{4.4}$$

where the angular spreads of the two clusters are assumed to be the same: i.e., $\sigma_{\theta,0} = \sigma_{\theta,1} = \sigma_\theta$. Thus, the DDG is given as [94]

$$G(\theta) = \frac{1}{2} G_0(\theta, \bar{\theta}_0) + \frac{1}{2} G_1(\theta, \bar{\theta}_1), \tag{4.5}$$

where $G_0(\theta, \bar{\theta}_0)$ is the DDG calculated when only cluster 0 is present using (4.2). Similarly, $G_1(\theta, \bar{\theta}_1)$ can be calculated using (4.2).

The above DDG calculation is given at one side (the transmitter or receiver). When both the transmit and receive sides are assumed to exploit the directional

beampattern of the ESPAR antenna, the joint directivity gain should be considered by incorporating the directivity gains at both link ends. Here, the AoD statistics are assumed to follow the same distribution of AoA (i.e., Laplacian distribution). It is noted that in this work we focus on analysis with one cluster. Alternatively, it can be considered that the beams are steered towards one cluster, and thus the impact of other clusters can be ignored because of spatial filtering. The directional channel is thus given by [92, 94]

$$
\begin{aligned}
h &= \sqrt{g_r(\theta_r)} * h(\theta_r, \theta_t) * \sqrt{g_t(\theta_t)} \\
&= \sqrt{G_r(\theta_r)}\sqrt{G_t(\theta_t)}\alpha,
\end{aligned}
\tag{4.6}
$$

where α is the complex gain of the cluster assumed to follow the Rayleigh fading, and $G_r(\theta)$, $G_t(\theta)$ are DDGs of receive antenna and transmit antenna, respectively.

For scenario 2, where 2-element ULA (omni-directional) is exploited at the transmit side while the ESPAR antenna is equipped at the receive side, the directional channel $\boldsymbol{h} \in \mathbb{C}^{1\times2}$ is modified as [92, 94]

$$
\begin{aligned}
\boldsymbol{h} &= \sqrt{g_r(\theta_r)} * h(\theta_r, \theta_t) * \boldsymbol{a}_t(\theta_t) \\
&= \sqrt{G_r(\theta_r)}\boldsymbol{h}_\alpha,
\end{aligned}
\tag{4.7}
$$

where $\boldsymbol{h}_\alpha \in \mathbb{C}^{1\times2}$ follows the Rayleigh fading, with elements $\mathbb{E}\{|\boldsymbol{h}_\alpha(i)|^2\} = 1, i = 1, 2$.

However, the above channel model is merely a statistical model. Therefore, we include some effects resulting from the geometry of the simulated indoor environment, listed as follows [83]:

- Path loss: The path loss is modelled as $38.5 + 20log_{10}(\underline{d}) + L_{wall}$, where $\underline{d}$ in meters is the distance between a femto-BS and a UT, L_{wall} denotes the penetration loss of the wall set to 5 dB per wall for indoor links.

- Shadowing: Shadow fading is modelled as a log-normal random variable ξ (dB) with a mean of 0 dB and a standard deviation of $\sigma_s = 4$ dB for the indoor femtocells.

- Receiver noise: The receiver noise power is calculated as $10log_{10}(kTNFW_b)$, where W_b is the effective noise bandwidth in Hz, $kT = 1.3804 \times 10^{-23} \times 290$ (Watt/Hz), and NF (dB) is the noise figure at the UT.

4.2 Interference Mitigation by Analog Beamforming

In scenario 1, there is only inter-cell interference. Without loss of generality, we consider the UT in the i-th femtocell, where $i \in \{1, \cdots, N_{fc}\}$. Its received signal is given by

$$y_i(t) = \underbrace{\sqrt{P_{r,i}}h_i s_i(t)}_{\text{desired signal}} + \underbrace{\sum_{j=1, j\neq i}^{N_{fc}} \sqrt{P_{r,j}}h_j s_j(t)}_{\text{inter-cell interference}} + z_i(t), \tag{4.8}$$

where $P_{r,j} = P_t \cdot 10^{(\xi - L(\underline{d}_j))/10}$ is the receive power from femto-BS j with a distance of $\underline{d}_j$, h_j is the channel coefficient between femto-BS j and UT i expressed in (4.6) taking into account the directional beampatterns at both link ends, $s_j(t)$ is the signal transmitted by femto-BS j, and $z_i(t)$ is the additive noise. Thus, the SINR achieved by UT i is given by

$$SINR_i = \frac{P_{r,i}|h_i|^2}{\sum_{j=1, j\neq i}^{N_{fc}} P_{r,j}|h_j|^2 + N_0}, \tag{4.9}$$

where N_0 represents the noise power. The achievable sum-rate of the system is thus given as

$$C = \sum_{i=1}^{N_{fc}} log(1 + SINR_i). \tag{4.10}$$

It is well known that the use of directional beampatterns is beneficial in nulling interference while improving quality of the receive signal, thereby enhancing SINR. For scenario 1, we exploit the analog beamforming of the ESPAR antenna to mitigate interference from other femtocells [95].

4.2.1 Beam Switching for Femtocells

We first consider a simple method, where the ESPAR antenna is exploited as a switched-beam antenna. We would remind readers that an $(M + 1)$-element ESPAR is able to form M sector beampatterns $B_m(\theta), m = \{1, \cdots, M\}$ which divide the whole angle space of the ESPAR transmitter/receiver into M sectors.

In general, the femto-BS and UT in the i-th femtocell individually select one beampattern from the M sector beampatterns to maximize the receive SINR, i.e.,

$$\max_{B_m^{t,i}, B_m^{r,i}} \quad SINR_i, \quad m \in \{1, \cdots, M\}, \tag{4.11}$$

where $B_m^{t,i}$ and $B_m^{r,i}$ represent the beampatterns selected by the femto-BS and UT in the i-th femtocell, respectively. Here, we assume that every femto-BS has knowledge of the direction of its UT, which can be achieved by using the direction estimation method (to be discussed in the next chapter). Similarly, every UT also knows the direction of its anchor femto-BSs. Under this assumption, femto-BS i simply selects a sector beampattern accessing the angular sector containing the direction of UT i. In the same way, UT i is able to choose an appropriate sector beampattern for communication. The beam switching method is quite simple and practical, without message exchange, cooperation across femtocells, or requirement of CSI. However, the beam switching is less flexible compared to the adaptive beamforming solution.

4.2.2 Adaptive Beamforming for Femtocells

Now, we consider the adaptive beamforming method for interference mitigation in femtocells. Although it increases computation complexity compared to the beam switching method, adaptive beamforming provides a better solution for interference mitigation. We assume that UTs only know the directions of their anchor

femto-BSs, since UTs do not exchange messages. However, femto-BSs are assumed to have knowledge of the directions of all UTs in the networks, which can be achieved by exchanging their measurement results through backhaul.

Based on these assumptions, the femto-BS uses a fast beamforming algorithm developed for the ESPAR array [45], since the desired direction as well as interfering directions are available. Suppose that femto-BS i wants to design a beampattern placing nulls at N_{int} interfering directions, denoted by the vector $\boldsymbol{\theta}_{null} = [\theta_1, \cdots, \theta_{N_{int}}]$. Let the matrix $A_{null} = [\boldsymbol{a}(\theta_1), \cdots, \boldsymbol{a}(\theta_{N_{int}})]$ store steering vectors corresponding to N_{int} interfering directions. The desired direction is denoted by θ_d. The beampattern is designed by solving the following problem

$$\boldsymbol{w}_{opt} = arg \min_{\boldsymbol{w}} \mu_1 \|\boldsymbol{A}_{null}^T \boldsymbol{w}\|^2 + \mu_2 |\boldsymbol{a}^T(\theta_d)\boldsymbol{w} - 1|^2, \qquad (4.12)$$

where μ_1 and μ_2 are weights on the importance of the nulls and desired direction magnitudes. This is analogous to the pattern synthesis problem in a conventional DBF array. Again, there is no closed-form solution to (4.12) for parasitic reactance loads with pure imaginary components. Fortunately, it is clear that (4.12) is a convex problem. Therefore, the beamforming algorithm can be modified as the method iterating between a convex problem and a simple projector, similar to MVDR beamforming. For simplicity, we do not repeat the detailed convex problem reformulation of (4.12), taking into account reactance loads design. The convex problem is given as [45]:

$$\min_{\mu_1, \mu_2, \boldsymbol{w}} \quad \beta_1\mu_1 + \beta_2\mu_2, \qquad (4.13a)$$

$$s.t. \quad \|\boldsymbol{A}_{null}^T\boldsymbol{w}\|^2 \leq \mu_1, \qquad (4.13b)$$

$$|\boldsymbol{a}^T(\theta_d)\boldsymbol{w} - 1|^2 \leq \mu_2, \qquad (4.13c)$$

$$\|\bar{\boldsymbol{Z}}_L\boldsymbol{w}\|^2 \leq \epsilon, \qquad (4.13d)$$

$$[\boldsymbol{Z}\boldsymbol{w}](1) + Z_s\boldsymbol{w}(1) = 1. \qquad (4.13e)$$

For UT i, since it knows only the desired direction, we use MVDR beamforming. The MVDR beamforming algorithm for an ESPAR antenna has been presented

in Chapter 2, where we do not repeat it here. It is worth noting that we need to replace the LOS channel model in (2.12) by

$$
\begin{aligned}
y_i(t_1) &= \sum_{j=1}^{N_{fc}} \sqrt{P_{r,j}} h_j(B_1) s_i(t_1) + z(t_1) \\
&\vdots \\
y_i(t_N) &= \sum_{j=1}^{N_{fc}} \sqrt{P_{r,ij}} h_j(B_N) s_j(t_1) + z(t_N),
\end{aligned}
\tag{4.14}
$$

$h_j(B_n)$ is the channel coefficient between femto-BS j and the n-th initial beampattern of UT i, where $n = \{1, \cdots, N\}$ and N is the total number of initial beampatterns used for signal measurements. According to the RD technique, (4.14) can be rewritten in vector form

$$
\boldsymbol{y}_i = \underbrace{\begin{bmatrix} \tilde{h}_{1,1} & \cdots & \tilde{h}_{1,N_{fc}} \\ \vdots & \ddots & \vdots \\ \tilde{h}_{N,1} & \cdots & \tilde{h}_{N,N_{fc}} \end{bmatrix}}_{\boldsymbol{H}} \begin{bmatrix} s_1 \\ \vdots \\ s_{N_{fc}} \end{bmatrix} + \begin{bmatrix} z_1 \\ \vdots \\ z_N \end{bmatrix},
\tag{4.15}
$$

where $\tilde{h}_{n,j} = \sqrt{P_{r,j}} h_j(B_n)$. Thus, a number of measurement vectors is used to calculate the estimate correlation matrix for use in the MVDR algorithm.

4.3 Interference Mitigation by Blind Interference Alignment

We exploit the ESPAR-based BIA scheme presented in Chapter 3 to mitigate interference in system scenario 2. However, it is noted that the original BIA scheme is designed to cancel intra-cell interference. Thus, its direct application in the multi-cell setting will not help to suppress inter-cell interference. In this section, we first review two BIA code structures – synchronized and non-synchronized code structures – via a simple two-cell system, then present the design of the BIA scheme suited to multiple femtocells.
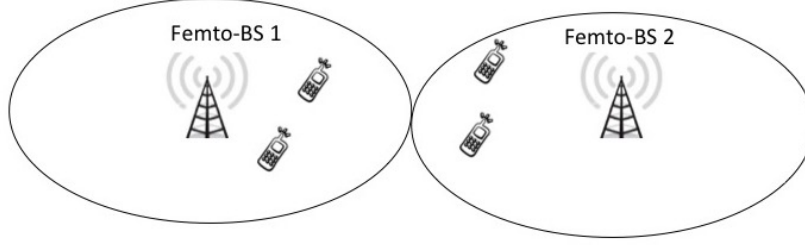
FIGURE 4.3: The two-cell MU-MISO system.

4.3.1 BIA Code Structures

As a prelude to examining the BIA code structures in the presence of interferences from the other cells, we consider the simplest two-cell system (Figure 4.3). Again, the case with $N_t = 2, K = 2$ is used as the driving example; i.e., each BS in the two cells is equipped with $N_t = 2$ antennas, and $K = 2$ users are simultaneously served in each cell.

Without loss of generality, consider cell 1 as the cell of interest. Femto-BS 1 exploits the transmit signal structure defined by the BIA scheme (see (3.16)) to deliver streams $\boldsymbol{u}^{[1]}, \boldsymbol{u}^{[2]}$ to its two users. At the same time, femto-BS 2 applies the BIA code to deliver streams $\boldsymbol{u}_I^{[1]}, \boldsymbol{u}_I^{[2]}$ to its two users, where the subscript denotes that they are interfering data streams from the other cell. Let γ_k be the SIR at user k in cell 1. For simplicity of discussion, here we assume that receive powers at users in cell 1 from femto-BS 1 is normalized to unity; thus, the quantity $-10log_{10}(\gamma)$ is a measure of the SIR in dB. Each user follows the staggered beampattern switching process defined by the BIA scheme. Then, received signal at user k in cell 1 at time t, when B_n is formed by the receive ESPAR antenna, is given by

$$y^{[k]} = \boldsymbol{h}^{[k]}(B_n)\boldsymbol{s}(t) + \sqrt{\alpha_k}\boldsymbol{h}_I^{[k]}(B_n)\boldsymbol{s}_I(t) + z^{[k]}(t), \quad k = 1, 2, \qquad (4.16)$$

where $\boldsymbol{h}_I^{[k]}(B_n) \in \mathbb{C}^{1 \times N_t}$ is the channel vector between antennas at BS 2 and user k in cell 1 associated with beampattern B_n.

The performance of the BIA scheme in the cell of interest (cell 1) will be examined for two different BIA code structures. They are presented as follows.

1) Synchronized BIA Code Structure

In the synchronized BIA code structure, femto-BS 1 and femto-BS 2 synchronize their transmission across one *Super Symbol* in time, at the mean time, users in each cell using the corresponding beampattern switching manner defined in the *Super Symbol* structure. Consider user 1 in cell 1: according to (3.16), its received signals across one *Super Symbol* are

$$
\begin{bmatrix} \boldsymbol{y}^{[1]}(1) \\ \boldsymbol{y}^{[1]}(2) \\ \boldsymbol{y}^{[1]}(3) \end{bmatrix} = \begin{bmatrix} \frac{1}{\sqrt{2}}\boldsymbol{h}^{[1]}(B_1) \\ \boldsymbol{h}^{[1]}(B_2) \\ \boldsymbol{0} \end{bmatrix} \boldsymbol{u}^{[1]} + \begin{bmatrix} \frac{1}{\sqrt{2}}\boldsymbol{h}^{[1]}(B_1) \\ \boldsymbol{0} \\ \boldsymbol{h}^{[1]}(B_1) \end{bmatrix} \boldsymbol{u}^{[2]} + \begin{bmatrix} z^{[1]}(1) \\ z^{[1]}(2) \\ z^{[1]}(3) \end{bmatrix}
$$
$$
+ \sqrt{\gamma_1} \begin{bmatrix} \frac{1}{\sqrt{2}}\boldsymbol{h}_I^{[1]}(B_1) \\ \boldsymbol{h}_I^{[1]}(B_2) \\ \boldsymbol{0} \end{bmatrix} \boldsymbol{u}_I^{[1]} + \sqrt{\gamma_1} \begin{bmatrix} \frac{1}{\sqrt{2}}\boldsymbol{h}_I^{[1]}(B_1) \\ \boldsymbol{0} \\ \boldsymbol{h}_I^{[1]}(B_1) \end{bmatrix} \boldsymbol{u}_I^{[2]}. \tag{4.17}
$$

Then user 1 in cell 1 cancels interference from user 2 in the same cell (intra-cell interference), using the post-processing step represented in (3.18). Therefore, user 1 achieves the following receive model

$$
\tilde{\boldsymbol{y}}^{[1]} = \underbrace{\begin{bmatrix} \boldsymbol{h}^{[1]}(B_1) \\ \boldsymbol{h}^{[1]}(B_2) \end{bmatrix}}_{\tilde{\boldsymbol{H}}^{[1]}} \boldsymbol{u}^{[1]} + \sqrt{\gamma_1} \underbrace{\begin{bmatrix} \boldsymbol{h}_I^{[1]}(B_1) \\ \boldsymbol{h}_I^{[1]}(B_2) \end{bmatrix}}_{\tilde{\boldsymbol{H}}_I^{[1]}} \boldsymbol{u}_I^{[1]} + \underbrace{\begin{bmatrix} \sqrt{2}z^{[1]}(1) - z^{[1]}(3) \\ z^{[1]}(2) \end{bmatrix}}_{\tilde{\boldsymbol{z}}^{[1]}} \tag{4.18}
$$

where $\tilde{\boldsymbol{z}}^{[1]} \sim \mathcal{CN}(\boldsymbol{0}, \boldsymbol{R}_{\tilde{z}})$ is the post-processed noise vector, with $\boldsymbol{R}_{\tilde{z}}$ given by (3.20).

As Equation (4.18) reveals, when the same BIA code is used across two cells in a synchronized way, a user is able to cancel the intra-cell interference and leave only one user's interference from the other cell. It is easy to verify that, when the synchronized BIA code structure is applied in the general K-user $N_t \times 1$ MISO BC case, the same result can be achieved for each user [76].

Assuming that the instantaneous interference-plus-noise covariance matrix is known, and treating the remaining inter-cell interference as noise, the achievable rate for user k in the cell of interest (cell 1) is thus given by

$$C_{syn}^{[k]} = \frac{1}{N_t + K - 1} \mathbb{E} \left\{ \log \det \left(\boldsymbol{I}_{N_t} + \frac{P_t}{N_t} \tilde{\boldsymbol{H}}^{[k]} \tilde{\boldsymbol{H}}^{[k]H} (\boldsymbol{R}_{v,syn}^{[k]})^{-1} \right) \right\}, \qquad (4.19)$$

where $\boldsymbol{R}_{v,syn}^{[k]}$ represents the instantaneous covariance matrix of the interference plus noise experienced by user k in the cell of interest, i.e.,

$$\boldsymbol{R}_{v,syn} = \boldsymbol{R}_{\tilde{z}} + \frac{P_t \gamma_k}{N_t} \tilde{\boldsymbol{H}}_I^{[k]} \tilde{\boldsymbol{H}}_I^{[k]H}. \qquad (4.20)$$

2) Non-synchronized BIA Code Structure

Again, femto-BS 1 and femto-BS 2 use the same standard BIA code given in (3.16). However, they are not synchronized in time. Thus, femto-BS 1 and femto-BS 2 transmit the data streams intended for two users in different time slots across one *Super Symbol*. We also consider cell 1 as the cell of interest. Given a block of three time slots, assume that signals transmitted by femto-BS 1 have the exactly same structure as that given in (3.16), while signals transmitted by femto-BS 2 are shifting by one symbol (or two symbols) of the original signal structure given in (3.16). Mathematically, signals transmitted by femto-BS 2 across the block of three time slots are represented as

$$\begin{bmatrix} \boldsymbol{s}_I(1) \\ \boldsymbol{s}_I(2) \\ \boldsymbol{s}_I(3) \end{bmatrix} = \begin{bmatrix} \boldsymbol{0}_2 \\ \frac{1}{\sqrt{2}} \boldsymbol{I}_2 \\ \boldsymbol{I}_2 \end{bmatrix} \boldsymbol{u}_I^{[1]} + \begin{bmatrix} \boldsymbol{I}_2 \\ \frac{1}{\sqrt{2}} \boldsymbol{I}_2 \\ \boldsymbol{0}_2 \end{bmatrix} \boldsymbol{u}_I^{[2]}. \qquad (4.21)$$

Comparing (4.21) with (3.16), the signals are shifted by one symbol. Indeed, one-symbol shifted signals and two-symbol shifted signals are equivalent from the point of view of ergodic rate performance.

Without loss of generality, user 1 in cell 1 is considered here. With the signal structure given in (4.21) and corresponding beampattern switching manner defined in the *Super Symbol* (Figure 3.2), receive signals at user 1 across a block of three

time slots are given by

$$
\begin{bmatrix} y^{[1]}(1) \\ y^{[1]}(2) \\ y^{[1]}(3) \end{bmatrix} = \begin{bmatrix} \frac{1}{\sqrt{2}} \boldsymbol{h}^{[1]}(B_1) \\ \boldsymbol{h}^{[1]}(B_2) \\ \boldsymbol{0} \end{bmatrix} \boldsymbol{u}^{[1]} + \begin{bmatrix} \frac{1}{\sqrt{2}} \boldsymbol{h}^{[1]}(B_1) \\ \boldsymbol{0} \\ \boldsymbol{h}^{[1]}(B_1) \end{bmatrix} \boldsymbol{u}^{[2]} + \begin{bmatrix} z^{[1]}(1) \\ z^{[1]}(2) \\ z^{[1]}(3) \end{bmatrix}
$$
$$
+ \sqrt{\gamma_1} \begin{bmatrix} \boldsymbol{0} \\ \frac{1}{\sqrt{2}} \boldsymbol{h}_I^{[1]}(B_2) \\ \boldsymbol{h}_I^{[1]}(B_1) \end{bmatrix} \boldsymbol{u}_I^{[1]} + \sqrt{\gamma_1} \begin{bmatrix} \boldsymbol{h}_I^{[1]}(B_1) \\ \frac{1}{\sqrt{2}} \boldsymbol{h}_I^{[1]}(B_2) \\ \boldsymbol{0} \end{bmatrix} \boldsymbol{u}_I^{[2]}. \tag{4.22}
$$

Again, user 1 follows the zero-forcing post-processing step (3.18) to cancel intra-cell interference. Substituting (4.22) to (3.18) yields the following post-processed measurements at user 1 in cell 1

$$
\tilde{\boldsymbol{y}}^{[1]} = \underbrace{\begin{bmatrix} \boldsymbol{h}^{[1]}(B_1) \\ \boldsymbol{h}^{[1]}(B_1) \end{bmatrix}}_{\tilde{\boldsymbol{H}}^{[1]}} \boldsymbol{u}^{[1]} + \underbrace{\begin{bmatrix} \sqrt{2}z^{[1]}(1) - z^{[1]}(3) \\ z^{[1]}(2) \end{bmatrix}}_{\tilde{\boldsymbol{z}}^{[1]}}
$$
$$
+ \sqrt{\gamma_1} \begin{bmatrix} \sqrt{2}\boldsymbol{h}_I^{[1]}(B_1)\boldsymbol{u}_I^{[2]} - \boldsymbol{h}_I^{[1]}(B_1)\boldsymbol{u}_I^{[1]} \\ \frac{1}{\sqrt{2}} \boldsymbol{h}_I^{[1]}(B_2)(\boldsymbol{u}_I^{[1]} + \boldsymbol{u}_I^{[2]}) \end{bmatrix} \tag{4.23}
$$
$$
= \tilde{\boldsymbol{H}}^{[1]} \boldsymbol{u}^{[1]} + \sqrt{\gamma_1} \bar{\boldsymbol{H}}_I^{[1]} \boldsymbol{u}_I + \tilde{\boldsymbol{z}}^{[1]},
$$

where $\boldsymbol{u}_I = \begin{bmatrix} \boldsymbol{u}_I^{[1]T}, \boldsymbol{u}_I^{[2]T} \end{bmatrix}^T$, and $\bar{\boldsymbol{H}}_I^{[1]}$ is expressed as

$$
\bar{\boldsymbol{H}}_I^{[1]} = \begin{bmatrix} \boldsymbol{h}_I^{[1]}(B_1) & \boldsymbol{0}_{1\times 2} \\ \boldsymbol{0}_{1\times 2} & \boldsymbol{h}_I^{[1]}(B_2) \end{bmatrix} \boldsymbol{B}_I^{[1]}, \tag{4.24}
$$

where the 4×4 matrix $\boldsymbol{B}_I^{[1]}$ is user specific, i.e.,

$$
\boldsymbol{B}_I^{[1]} = \begin{bmatrix} -\boldsymbol{I}_2 & \frac{1}{\sqrt{2}} \boldsymbol{I}_2 \\ \sqrt{2} \boldsymbol{I}_2 & \frac{1}{\sqrt{2}} \boldsymbol{I}_2 \end{bmatrix}. \tag{4.25}
$$

With the same BIA code structure and procedure, user 2 in cell 1 obtains similar post-processed measurements taking the following form

$$\tilde{\boldsymbol{y}}^{[2]} = \tilde{\boldsymbol{H}}^{[2]}\boldsymbol{u}^{[2]} + \sqrt{\gamma_2}\bar{\boldsymbol{H}}_I^{[2]}\boldsymbol{u}_I + \tilde{\boldsymbol{z}}^{[2]}, \qquad (4.26)$$

where

$$\bar{\boldsymbol{H}}_I^{[2]} = \begin{bmatrix} \boldsymbol{h}_I^{[2]}(B_1) & \boldsymbol{0}_{1\times2} \\ \boldsymbol{0}_{1\times2} & \boldsymbol{h}_I^{[2]}(B_2) \end{bmatrix} \boldsymbol{B}_I^{[2]}, \qquad (4.27)$$

with the 4×4 matrix $\boldsymbol{B}_I^{[2]}$ given by

$$\boldsymbol{B}_I^{[2]} = \begin{bmatrix} -\frac{1}{\sqrt{2}}\boldsymbol{I}_2 & \frac{1}{\sqrt{2}}\boldsymbol{I}_2 \\ \boldsymbol{I}_2 & \boldsymbol{0}_2 \end{bmatrix}. \qquad (4.28)$$

It is noted that similar results can be derived for the general K-user $N_t \times 1$ MISO BC, where the matrix $\boldsymbol{B}_I^{[k]}$ is user specific, given K and N_t. When the instantaneous interference-plus-noise covariance matrix is known at the desired user (user k in cell 1), then treat the inter-cell interference as noise. User k's achievable rate is expressed as

$$C_{nsyn}^{[k]} = \frac{1}{N_t + K - 1}\mathbb{E}\left\{\log\det\left(\boldsymbol{I}_{N_t} + \frac{P_t}{N_t}\tilde{\boldsymbol{H}}^{[k]}\tilde{\boldsymbol{H}}^{[k]H}(\boldsymbol{R}_{v,nsyn}^{[k]})^{-1}\right)\right\}, \qquad (4.29)$$

where the interference plus noise covariance matrix $\boldsymbol{R}_{v,nsyn}^{[k]}$ is represented as

$$\boldsymbol{R}_{v,nsyn}^{[k]} = \boldsymbol{R}_{\tilde{z}} + \frac{P_t\gamma_k}{N_t}\bar{\boldsymbol{H}}_I^{[k]}\bar{\boldsymbol{H}}_I^{[k]H}. \qquad (4.30)$$

From the point of view of the ergodic rate, the performance of the synchronized BIA code structure is superior to that of the non-synchronized BIA code structure, especially when N_t and K are large. Since non-synchronized BIA code is being used, the interference from the other cell cannot be reduced. We illustrate this as the numerical results given in Figure 4.4, where, for simplicity, we use the generic channel vectors, instead of the directional channel vector related to the EPSAR antenna beampatterns. It is clear that the observations will hold in the case where
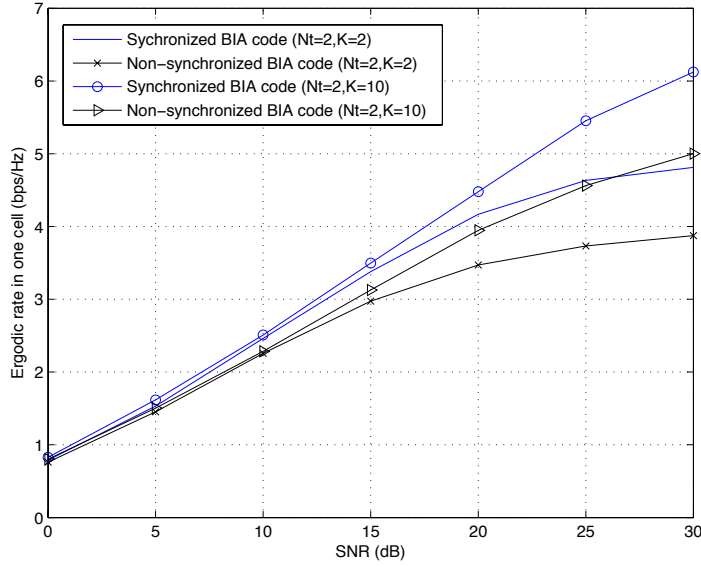
FIGURE 4.4: Ergodic rate versus SNR, SIR $= 10$ dB.

the ESPAR antenna is considered. Thus, in the following study, we will always assume that the BIA code structure used across femtocells is synchronized, in order to minimize inter-cell interference.

4.3.2 Synchronized BIA and Virtual BIA for Femtocells

When multiple users are simultaneously served by each femto-BS, a UT suffers from both intra-cell and inter-cell interference. Let $\boldsymbol{h}_j^{[k,i]}(B_m) \in \mathbb{C}^{1\times 2}$ denote the channel between the j-th femto-BS and UT k in femtocell i associated with beampattern B_m, where $k \in \{1, \cdots, K\}$ and $i, j \in \{1, \cdots, N_{fc}\}$. Then, the received signal at user k in the i-th femtocell is represented as

$$y^{[k,i]}(t) = \underbrace{\sqrt{P_{r,i}}\boldsymbol{h}_i^{[k,i]}(B_m)\boldsymbol{s}_i(t)}_{\substack{\text{desired signal plus} \\ \text{intra-cell interference}}} + \underbrace{\sum_{j=1, j\neq i}^{N_{fc}} \sqrt{P_{r,j}}\boldsymbol{h}_j^{[k,i]}(B_m)\boldsymbol{s}_j(t)}_{\text{inter-cell interference}} + z^{[k,i]}(t), \quad (4.31)$$

where $\boldsymbol{s}_j(t) \in \mathbb{C}^{2\times 1}$ is signal transmitted by femto-BS j, and $z^{[k,i]}(t) \sim \mathcal{CN}(0, \sigma_z^2)$ is the additive white noise.
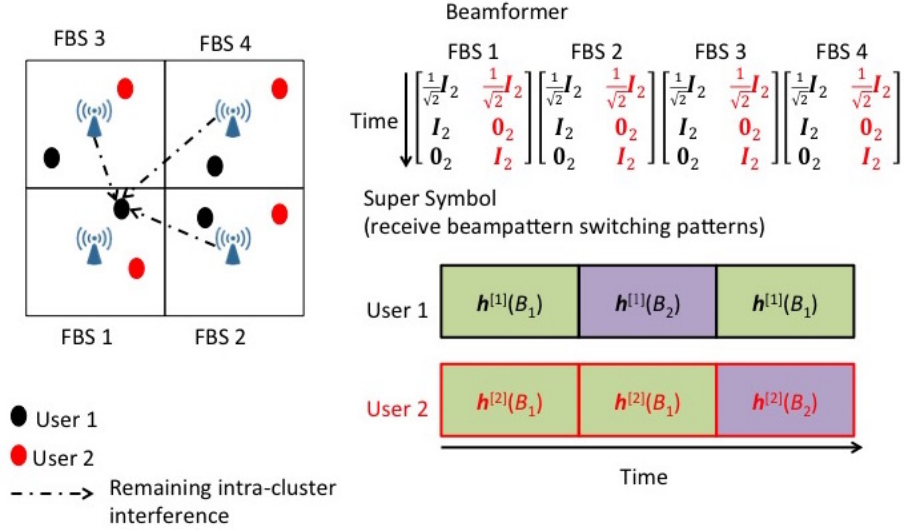
FIGURE 4.5: Synchronized BIA code structure applied across a group of four femtocells, each of which serves two UTs.

In particular, we will consider two BIA schemes – synchronized BIA and virtual BIA – for the multi-cell setting, to deal with both intra-cell and inter-cell interference.

1) Synchronized BIA Scheme

The simplest way to exploit BIA in the femtocell network is to apply the same BIA code structure across femtocells in a synchronized manner, as we described previously via a simple two-cell system. Specifically, each femto-BS uses the same beamformer for transmission. For individual UTs, the same receive beampattern switching patterns given in the single-cell setting are employed. The idea is illustrated in an environment where there are four femtocells, each of which simultaneously serves two UTs across one *Super Symbol*, as shown in Figure 4.5. Consider user 1 (colored as black) in femtocell 1, with synchronized BIA. We know that after user 1 cancels the interference from user 2 (colored as red) in the same cell, inter-cell interference from femtocells 2, 3 and 4 related to the data intended for red users can also be cancelled out, while interference related to data meant for black users in the neighboring cells remains. Normalized rate achievable at user k in i-th femtocell is thus given by

$$C_{synbia}^{[k,i]} = \frac{1}{N_t + K - 1} \mathbb{E}\left\{ \log \det \left(\boldsymbol{I}_{N_t} + \frac{P_{r,i}}{N_t} \tilde{\boldsymbol{H}}_i^{[k,i]} \tilde{\boldsymbol{H}}_i^{[k,i]H} \boldsymbol{R}_v^{-1} \right) \right\}, \qquad (4.32)$$

where $\boldsymbol{R}_v \in \mathbb{C}^{N_t \times N_t}$ is the covariance matrix of noise plus interference of the following form

$$\boldsymbol{R}_v = \boldsymbol{R}_{\tilde{z}} + \sum_{j=1, j\neq i}^{N_{fc}} \frac{P_{r,j}}{N_t} \tilde{\boldsymbol{H}}_j^{[k,i]} \tilde{\boldsymbol{H}}_j^{[k,i]H}, \qquad (4.33)$$

$$\tilde{\boldsymbol{H}}_j^{[k,i]} = \left[\boldsymbol{h}_j^{[k,i]T}(B_1) \quad \boldsymbol{h}_j^{[k,i]T}(B_2) \quad \cdots \quad \boldsymbol{h}_j^{[k,i]T}(B_{N_t}) \right]^T, \qquad (4.34)$$

$\boldsymbol{R}_{\tilde{z}}$ is given in (3.20).

2) Virtual BIA Scheme

Using the synchronized BIA scheme in the multiple cell setting, there is still residual interference from the other cells. In order to completely cancel inter-cell interference, we consider a group of N_{fc} femtocells as one virtual cell, simultaneously serving a total number of $N_{fc} \cdot K$ users. In this context, inter-cell interference is thus seen as "intra-cell" interference. Therefore, the original BIA scheme derived for the single-cell setting can be directly applied to the virtual cell to cancel all kinds of interference. This is referred to as a *virtual BIA scheme* or an *extended BIA scheme* [88].

The idea is illustrated via an environment with four femtocells, each of which serves two users (Figure 4.6). In the virtual BIA scheme, this femtocell system is considered as a single virtual cell having one virtual femto-BS equipped with two transmit antennas and simultaneously serving eight active UTs. According to the original BIA scheme [27], the *Super Symbol* structure for the 8-user 2×1 MISO is given as Figure 4.6 (b).
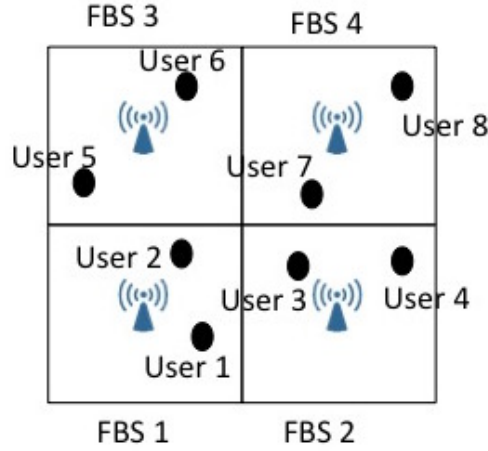
(a) Virtual femtocell example.

$h_j^{[k]}(B_1), k \in \{1, \cdots, 8\}, j \in \{1, \cdots, 4\}$

$h_j^{[k]}(B_2), k \in \{1, \cdots, 8\}, j \in \{1, \cdots, 4\}$
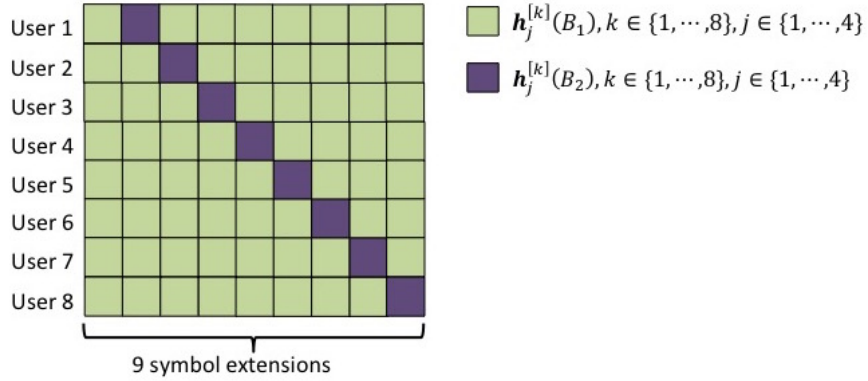
(b) *Super Symbol* for the virtual femtocell

FIGURE 4.6: Illustration of virtual BIA scheme for a group of four femtocells, each of which serves two UTs.

To avoid data exchange across the four femto-BSs in the virtual BIA scheme, we assume that data streams intended for each user are transmitted by its anchor femto-BS, using the precoding matrix defined in the *Super Symbol*. The precoding matrices for 8 users used by four femto-BSs are given by

$$
\begin{array}{cc} user1 & user2 \end{array} \quad \begin{array}{cc} user3 & user4 \end{array} \quad \begin{array}{cc} user5 & user6 \end{array} \quad \begin{array}{cc} user7 & user8 \end{array}
$$

$$
\begin{pmatrix} \frac{1}{\sqrt{8}}\boldsymbol{I}_2 & \frac{1}{\sqrt{8}}\boldsymbol{I}_2 \\ \boldsymbol{I}_2 & \boldsymbol{0}_2 \\ \boldsymbol{0}_2 & \boldsymbol{I}_2 \\ \boldsymbol{0}_2 & \boldsymbol{0}_2 \\ \boldsymbol{0}_2 & \boldsymbol{0}_2 \\ \boldsymbol{0}_2 & \boldsymbol{0}_2 \\ \boldsymbol{0}_2 & \boldsymbol{0}_2 \\ \boldsymbol{0}_2 & \boldsymbol{0}_2 \\ \boldsymbol{0}_2 & \boldsymbol{0}_2 \end{pmatrix} \begin{pmatrix} \frac{1}{\sqrt{8}}\boldsymbol{I}_2 & \frac{1}{\sqrt{8}}\boldsymbol{I}_2 \\ \boldsymbol{0}_2 & \boldsymbol{0}_2 \\ \boldsymbol{0}_2 & \boldsymbol{0}_2 \\ \boldsymbol{I}_2 & \boldsymbol{0}_2 \\ \boldsymbol{0}_2 & \boldsymbol{I}_2 \\ \boldsymbol{0}_2 & \boldsymbol{0}_2 \\ \boldsymbol{0}_2 & \boldsymbol{0}_2 \\ \boldsymbol{0}_2 & \boldsymbol{0}_2 \\ \boldsymbol{0}_2 & \boldsymbol{0}_2 \end{pmatrix} \begin{pmatrix} \frac{1}{\sqrt{8}}\boldsymbol{I}_2 & \frac{1}{\sqrt{8}}\boldsymbol{I}_2 \\ \boldsymbol{0}_2 & \boldsymbol{0}_2 \\ \boldsymbol{0}_2 & \boldsymbol{0}_2 \\ \boldsymbol{0}_2 & \boldsymbol{0}_2 \\ \boldsymbol{0}_2 & \boldsymbol{0}_2 \\ \boldsymbol{I}_2 & \boldsymbol{0}_2 \\ \boldsymbol{0}_2 & \boldsymbol{I}_2 \\ \boldsymbol{0}_2 & \boldsymbol{0}_2 \\ \boldsymbol{0}_2 & \boldsymbol{0}_2 \end{pmatrix} \begin{pmatrix} \frac{1}{\sqrt{8}}\boldsymbol{I}_2 & \frac{1}{\sqrt{8}}\boldsymbol{I}_2 \\ \boldsymbol{0}_2 & \boldsymbol{0}_2 \\ \boldsymbol{0}_2 & \boldsymbol{0}_2 \\ \boldsymbol{0}_2 & \boldsymbol{0}_2 \\ \boldsymbol{0}_2 & \boldsymbol{0}_2 \\ \boldsymbol{0}_2 & \boldsymbol{0}_2 \\ \boldsymbol{0}_2 & \boldsymbol{0}_2 \\ \boldsymbol{I}_2 & \boldsymbol{0}_2 \\ \boldsymbol{0}_2 & \boldsymbol{I}_2 \end{pmatrix} .
$$

$$
\underbrace{}_{\text{FBS 1}} \quad \underbrace{}_{\text{FBS 2}} \quad \underbrace{}_{\text{FBS 3}} \quad \underbrace{}_{\text{FBS 4}}
$$

With this strategy, UT k in cell i, $k \in \{1, \cdots, 8\}$ and $i \in \{1, \cdots, 4\}$, is able to completely cancel both intra-cell and inter-cell interference with a simple zero-forcing processing step: i.e.,

$$
\begin{aligned}
\tilde{\boldsymbol{y}}^{[k,i]} &= \begin{bmatrix} \sqrt{8}y^{[k,i]}(1) - y^{[k,i]}(k+1) \\ y^{[k,i]}(k) \end{bmatrix} \\
&= \begin{bmatrix} \boldsymbol{h}_i^{[k,i]}(B_1) \\ \boldsymbol{h}_i^{[k,i]}(B_2) \end{bmatrix} \boldsymbol{u}^{[k,i]} + \begin{bmatrix} \sqrt{8}z^{[k,i]}(1) - z^{[k,i]}(k+1) \\ z^{[k,i]} \end{bmatrix} .
\end{aligned} \tag{4.35}
$$

It is noted that the virtual BIA scheme uses more symbol extensions than does the synchronized BIA scheme. It is easy to extend this virtual BIA scheme to the case with arbitrary values of K and N_t. However, large values of K and N_t are not practical, due to the requirement for a longer *Super Symbol*. Consequently, the achievable normalized rate of user k in cell i is

$$
C_{virbia}^{[k,i]} = \frac{1}{N_t + N_{fc}K - 1} \mathbb{E}\left\{ \log \det \left(\boldsymbol{I}_{N_t} + \frac{P_{r,i}}{N_t} \tilde{\boldsymbol{H}}_i^{[k,i]} \tilde{\boldsymbol{H}}_i^{[k,i]H} \boldsymbol{R}_{\tilde{z}}^{-1} \right) \right\}. \tag{4.36}
$$

Notice that the inter-cell interference is completely cancelled by the virtual BIA

scheme at the cost of increasing the length of the *Super Symbol*. Thus, the scheme is more suitable to be employed in a scenario with a high interference power level; that is, where users are mainly located at the cell-edge. In contrast, in the scenario where users are mainly located in the cell-center, directly applying the synchronized BIA code structure may be superior to the virtual BIA strategy, since the interference power level is weak here and the longer *Super Symbol* leads to a smaller achievable rate at each user.

4.4   Simulations

In this section, we evaluate the interference mitigation performance of the proposed methods by employing the ESPAR antenna. Here, the 7-element ESPAR antenna is adopted again as the simulated ESPAR antenna, whose parameters are given in Chapter 2. For the ESPAR-based BIA scheme, each femto-BS is equipped with 2-element ULA with inter-element spacing of $\lambda/2$. Table 4.1 summarizes some key parameters used in simulations. The simulated results are averaged from 1000 Monte-Carlo experiments.

TABLE 4.1: Simulation Parameters

Symbol	Description	Value
N_{fc}	Number of femtocells	1-9
R_f	Femtocell radius	10 m
P_t	FBS's transmit power	20 dBm
L_{wall}	Penetration loss of wall	5 dB
σ_s	Shadowing standard deviation	8 dB
W_b	Noise effective bandwidth	3.84 MHz
NF	Noise figure at UT	7 dB
B_{omni}	Beampattern gain of omni-directional antenna	5 dB
σ_θ	Angular spread in PAS	10°

4.4.1 ESPAR analog beamforming for scenario 1

We first consider the interference mitigation for scenario 1, where the ESPAR antenna is deployed at both the femto-BS and UT, and a single user is scheduled to be served by each femto-BS for one time slot. We examine two proposed approaches: beam switching and adaptive beamforming. For the beam switching, a 7-element ESPAR antenna is able to form 6 sector beampatterns. One femto-BS/UT dynamically selects an appropriate beampattern out of the 6 sector beampatterns, according to knowledge of direction of the desired UT/femto-BS. For the adaptive beamforming, the convex optimization problems (see (4.13) and (2.26)) were solved using the free optimization software SeDuMi [65] and modelling language YALMIP [64]. In the convex problem (4.13), we limit the number of nulls to 3; i.e., directions of UTs in the 3 nearest neighboring femtocells. The iteration number is set to 20. The single omni-directional antenna is used as a baseline for comparison, where its antenna gain is set to 5 dB in all directions. In each femtocell, we generate 200 realizations of the UT locations.

Figure 4.7 (a) shows the cumulative distribution function (CDF) of SINRs of UTs in the 9-femtocell network. It is observed that the increment of the average SINR (i.e., the SINR value corresponding to the CDF of 0.5) is about 8.9 dB by ESPAR beam switching (compared to the omni-directional antenna), and the increment is around 11.7 dB by ESPAR adaptive beamforming. In addition to the mean SINR, we would like to check the worst 5-percentile of users' performance, which is important information for the operator. According to Figure 4.7 (a), the worst 5-percentile users' SINR is improved by 8.9 dB using the ESPAR antenna. However, the difference between beam switching and adaptive beamforming can be ignored here. Finally, we check the 95-percentile users' SINR. It is illustrated in Figure 4.7 (a) that the 95-percentile users' SINR is 16.1 dB for omni-directional antennas, 25.9 dB for ESPAR beam switching, and 30.4 dB for ESPAR adaptive beamforming. Overall, adaptive beamforming is superior to the beam switching scheme at the cost of computational complexity. Correspondingly, similar trends
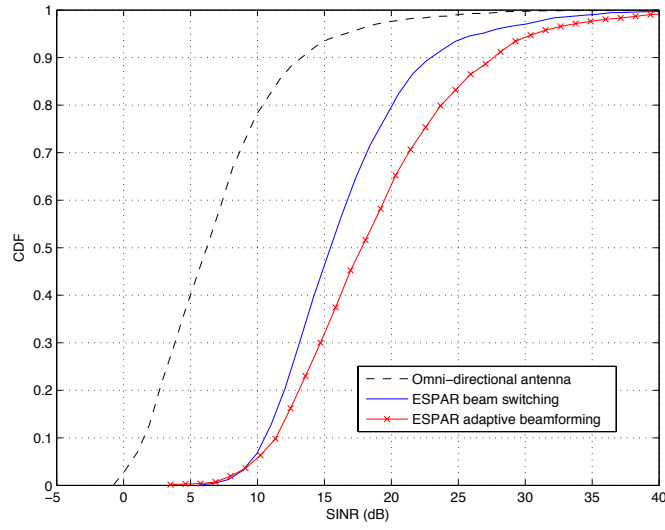
(a) CDF of users' SINR
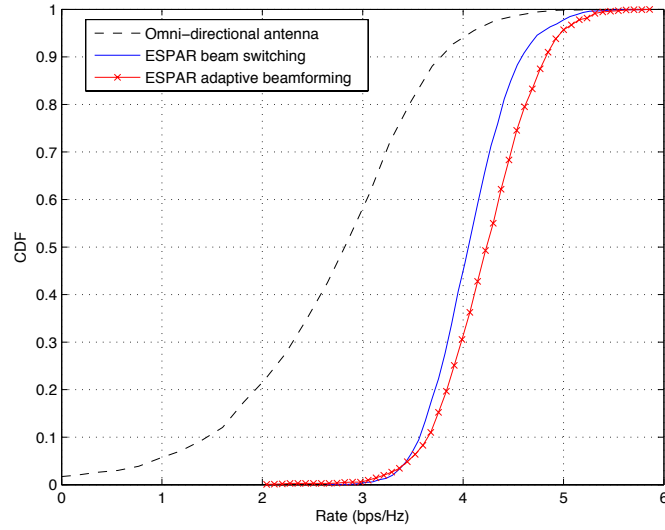
(b) CDF of users' achievable rates

FIGURE 4.7: Performance gain of ESPAR scheme over omni-directional antenna in a 9-femtocell network.

are observed in the CDF of the rates of UTs in the 9 femtocells (see Figure 4.7 (b)).

In the femtocell networks, the smart antenna system is generally assumed to be suitable only for small BSs: for example, switched-beam antennas are used at the femto-BSs in the literature [83–86]. Here, we also evaluate the performance where the ESPAR antenna is deployed only at the femto-BSs, while the UTs are equipped
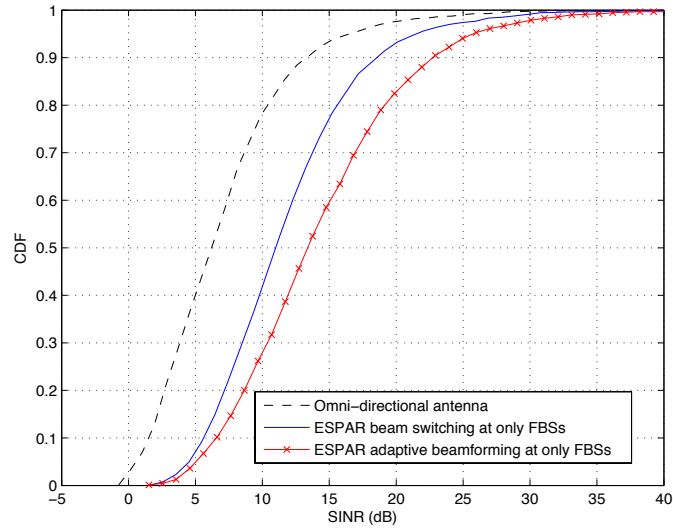
(a) CDF of users' SINR
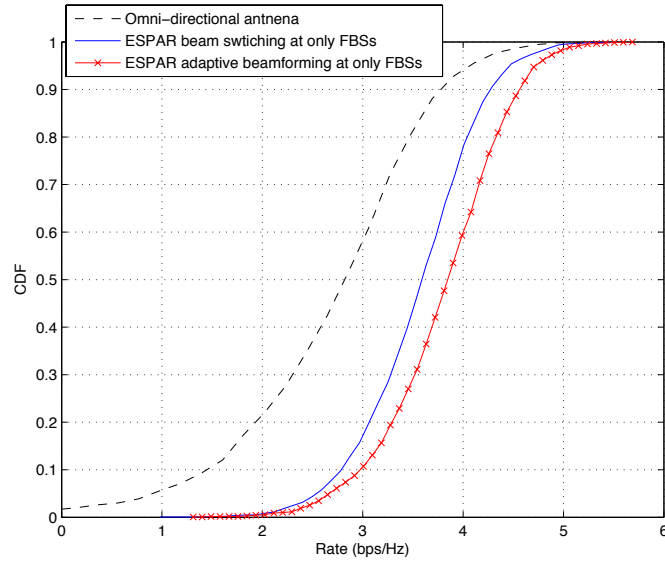
(b) CDF of users' achievable rates

FIGURE 4.8: Performance gain of ESPAR antenna only adopted by FBSs in a 9-femtocell network.

with a single omni-directional antenna, as illustrated in Figure 4.8. From Figure 4.8 (a), we can see that the increment of the mean SINR is about 4.8 dB by ESPAR beam switching (compared to the omni-directional antenna), and the increment is around 6.8 dB by ESPAR adaptive beamforming. The mean SINRs are reduced to a half of that when the ESPAR antenna is deployed at both link ends. The worst 5-percentile users' SINR is 4.5 dB with ESPAR beam switching, and 5.59 dB with

ESPAR adaptive beamforming. These values are again reduced to half of that given in Figure 4.7 (a). Nevertheless, comparing these two cases, the 95-percentile users SINR has not been doubled. The reason is that for UTs located at the center and with low interference power, the effects of the directional beampattern are less sensitive than for the cell-edge UTs. Similar trends are observed in the CDF of the rates of UTs in Figure 4.8 (b). Overall, these results suggest that, with the compact deployment of smart antennas at both small BSs and UTs in future networks, the performance gains will be significant, while system costs and complexity will be reduced.

Figure 4.9 depicts the achievable sum-rate for the system with a varying number of femtocells. We can observe, from the case using omni-directional antennas (no interference mitigation), that the system sum-rate is degraded with increasing femtocell numbers when $N_{fc} \leq 5$, due to higher interference power level. For the cases using ESPAR antennas (at both the femto-BSs and UTs), the system sum-rate has been significantly improved. Again, the performance gains achieved by adaptive beamforming outperform that by beam switching, at the cost of increased computational complexity.
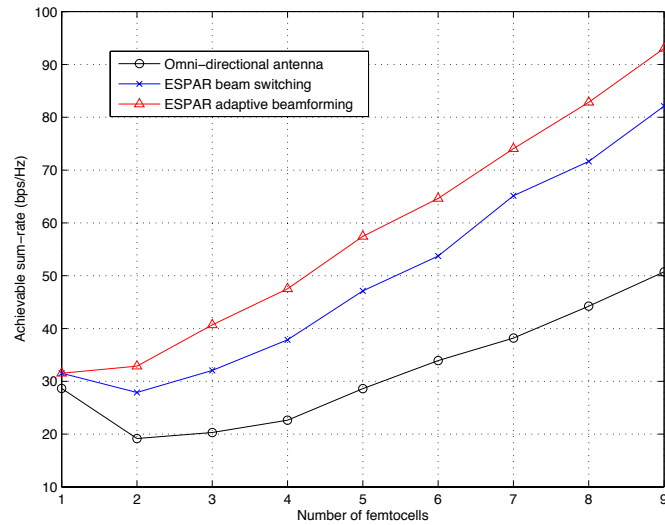
FIGURE 4.9: System sum-rate vs. femtocell number.

4.4.2   ESPAR-based BIA for scenario 2

In this part, we examine the performance of the proposed ESPAR-based BIA schemes for scenario 2, where each femto-BS is equipped with a 2-element ULA while two UTs served by each femtocell have a 7-element ESPAR antenna each. We consider a 9-femtocell network. In particular, we evaluate the achievable sum-rate in the center cell, which encounters the highest number of interferences from the neighboring cells. Moreover, the performance of the ESPAR-based BIA schemes is compared with that of the LZFBF described in Chapter 3, Section 3.5.1.

In order to analyze the effect of the inter-cell interference, we first assume that two UTs in the center cell move from cell center to cell edge, while UTs in other cells are fixed, as shown in Figure 4.10. The achievable sum-rate in the center femtocell is calculated for the synchronized BIA and virtual BIA schemes, given respectively by (4.32) and (4.36), where we consider three ESPAR beamforming methods (random beamforming, sector beampattern selection and SVD-based beamforming, described in Chapter 3). For SVD-based beamforming, we assume that the receiver only knows the channels from its serving BS; therefore, the SVD beamformer uses this knowledge to design beampatterns.

The results are shown in Figure 4.11. As expected, the synchronized BIA outperforms the virtual BIA when users are located near the femto-BS. The cross points are about 2.3 m with the random beampatterns, and around 3.6 m with the selected sector beampattern and the SVD-based beamforming. Since the femtocell system is an interference-limited system with cell-size reduction, performance of the virtual BIA scheme is better than that of the synchronized BIA scheme in most of the distance range from the cell-edge to the cell-center, through completely cancelling inter-cell interference. Although the ESPAR-based BIA schemes are inferior to the LZFBF in the cell-center, their rate gains are larger than the LZFBF at the cell-edge. The other observation is that the BIA schemes using selected sector beampatterns, and beampatterns designed based on SVD beamforming, provide higher sum-rates compared to those using random beampatterns, since the directional beampatterns are selected/designed to enhance the receive SINR/SNR.
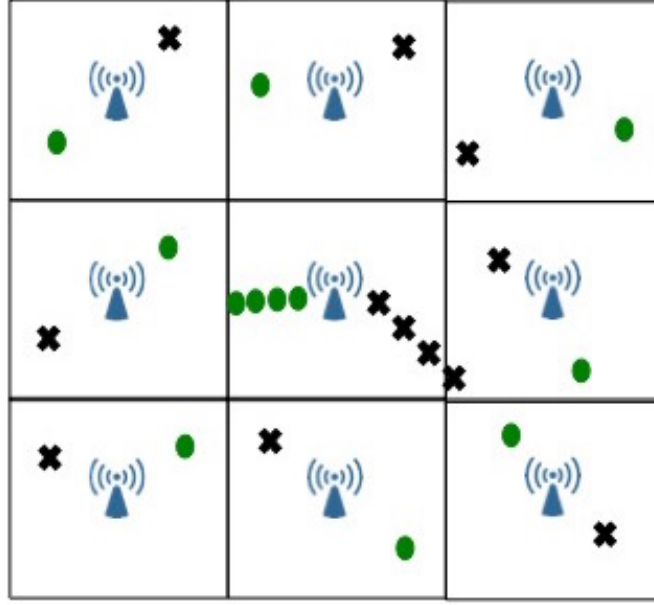
FIGURE 4.10: The 9-cell network used for simulations.

However, the difference between the SVD beamforming and sector beampattern selection is not significant. The reason may be that, with SVD beamforming, the beampatterns are only designed to enhance receive SNR using the CSIR from the desired femto-BS, without suppressing the inter-cell interference. However, the computational complexity of SVD-based beamforming is higher than that of the other two methods. In the next simulations, we only consider the performance of the BIA scheme, using random beampatterns and selected sector beampatterns.

Now, we simulate the CDF of the sum-rate of two users in the center cell, where 200 realizations of users' locations are generated and for each location realization is averaged from 1000 Monte-Carlo simulations. Figure 4.12 shows the simulated results, from which one can make the following observations. With respect to the mean sum-rate as well as the worst 5-percentile users' performance, the ESPAR-based BIA schemes provide significant rate gains compared to the LZFBF, where the increment of mean sum-rate is up to 3.6 dB , and the increment of worst 5-percentile users' sum-rate is up to 4.2 dB employing virtual BIA with selected
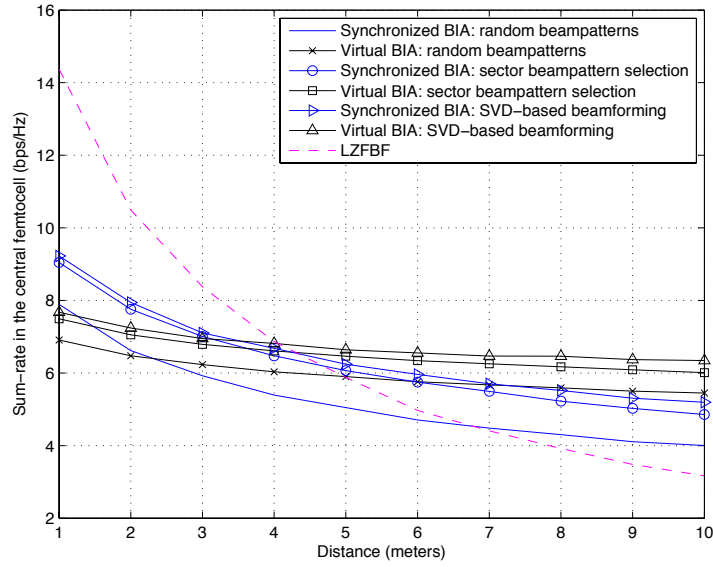
FIGURE 4.11: Achievable sum-rate in the center femtocell versus users' distance to the femto-BS.
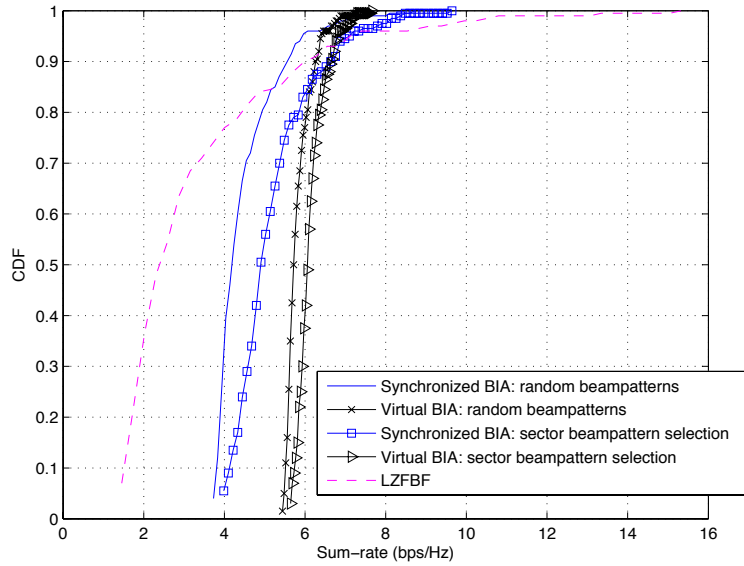
FIGURE 4.12: CDR of the sum-rate in the center femtocells.

sector beampatterns. From the comparison between the BIA schemes, the virtual BIA scheme outperforms the synchronized BIA scheme, since the inter-cell interference has been completely cancelled.

4.5   Summary

This chapter employs the ESPAR antenna as a solution for interference mitigation in the residential femtocells, thereby improving system rate. In particular, the interference mitigation approaches are proposed under two scenarios.

- Scenario 1: one user is scheduled to communicate in each femtocell for one time slot, where users are subject only to inter-cell interference. For this scenario, we adopt the ESPAR antenna at both the femto-BSs and UTs, and then ESPAR's capability of beamforming is exploited to enhance the receive SINR. In particular, the switched-beam antenna and the adaptive beamforming algorithm proposed in Chapter 2 are exploited in the femtocell networks, to show their feasibility in mitigation interferences from other cells. This indicates the importance role of deployment of the smart antenna system for compactness applications in future networks.

- Scenario 2: two users are scheduled to communicate in each femtocell at one time slot, where users are subject to both intra-cell and inter-cell interference. For this scenario, we consider that the ESPAR antenna is deployed at the UTs, while the femto-BSs are equipped with a 2-element ULA each. Thus, the ESPAR-based BIA scheme, presented in Chapter 3, is considered as a means to address both intra-cell and inter-cell interference. In order to extend the BIA scheme in the multi-cell setting, the synchronized and non-synchronized BIA code structures are studied. It is demonstrated that only the synchronized BIA code structure is able to minimize inter-cell interference. Based on this, two BIA schemes are considered in the femtocell networks: synchronized BIA scheme and virtual BIA scheme. Since the femtocell system is an interference-limited system due to cell size reduction, in general, the virtual BIA scheme is superior to the synchronized BIA scheme, especially at the cell-edge. Moreover, the BIA schemes perform better than the LZFBF at the cell-edge, by minimizing inter-cell interference.

Chapter 5

ESPAR Antennas for Spatial Spectrum Sensing in Cognitive Radios

In this chapter, the cognitive radio (CR) system is considered. CR is a novel technology: a wireless communication system intended to enable a secondary user (SU) to operate in the same frequency subband as that originally allocated to the primary user (PU), thereby addressing the problem of underutilization of the limited spectral resource [34]. As we mentioned in Chapter 4, the CR technology can be introduced in the SCNs to mitigate cross-tier interference (i.e., macrocell-to-femtocell interference), where the macrocell can be considered as the primary link, while the femtocells are the secondary links. Thus, the femtocells communicate without causing harmful interference to the macrocell. In particular, this work focuses on the CR system with the interweave paradigm, in which the SU exploits knowledge of the PU's activity in the spectrum to identify transmission opportunity [34]. In this context, spectrum sensing is the most important component for establishing the CR system.

Conventionally, spectrum sensing is a task to gain awareness of PU activity in a brand of frequencies at a particular time in a particular geographic area. It

takes into account only three dimensions of the spectrum space: frequency, time and geographic space. Besides these dimensions, the angle dimension can also be introduced in spectrum space to further efficient use of the spectral resource [35]. With the development of smart antenna technology (beamforming), the SU transmitter is able to transmit its data over a subband of frequency (even with the presence of the PU in the same geographical area and without interfering with the PU), by steering its beampattern in different angular directions. To exploit the new angle dimension, the SU is required not only to sense conventional three-dimensional spectrum space but also to estimate the AoA of the existing PU. This is referred to as *spatial spectrum sensing*. Indeed, *spatial spectrum sensing* has not attracted attention for small CR terminal applications, since, in most of the literature, multi-active antenna arrays are assumed to operate the *spatial spectrum sensing* function.

This chapter employs the ESPAR antenna to perform spatial spectrum sensing at compact CR terminals. In Section 5.1, the CR system model is presented, and a two-stage spectrum sensing method is also described. At the first stage, the ESPAR receiver performs *Temporal spectrum sensing* to detect whether a subband of frequency is occupied by the PU. If the decision is made that the PU is absent, the sensing procedure finishes; otherwise, at the second stage, the ESPAR receiver detects the AoA of the existing PU. *temporal spectrum sensing* is referred to as traditional spectrum sensing in terms of 3-directional spectrum space without angle dimension. Sensing methods, including the energy detector and eigenvalue-based detection, have been studied for ESPAR cognitive radio terminals in [44, 45], and are exploited in the first stage of our strategy (Section 5.2). However, in [44, 45], the authors have not considered the high resolution AoA estimation method for *spatial spectrum sensing* with the ESPAR array.

Our work thus includes the study of the high-resolution AoA estimation algorithms for ESPAR-based CR terminals at the second stage to fulfil *spatial spectrum sensing*. For the ESPAR antenna, some subspace algorithms such as RD-MUSIC [43, 96] and RD-ESPRIT [53, 54] have been developed, which are able to provide

high-resolution estimation performance. It is noted that these subspace methods require Nyquist-rate sampling of the received signals to estimate directions of a small number of source signals, which may be very expensive in some applications. Moreover, the unique configuration of the ESPAR antenna with a single active element requires that its signal processing operates in the reactance-domain (or beamspace) instead of the element-domain. Thus, an AoA estimation method with reduction of sampling numbers is more important for the ESPAR receiver in order to reduce complexity. Recently, the emerging field of compressive sensing (CS) [97] has provided an alternative solution to the AoA estimation problem with super resolution, while exploiting only a small number of samples. In Section 5.3, we study the sparse signal representation problem for a solution to direction finding for the ESPAR antenna; this will be compared with the subspace method – RD-MUSIC. We begin with proposing the sparse signal representation of the AoA estimation problem for the ESPAR array. Since the model of a small number of signals impinging on a receive antenna array implies a sparse spectrum in the spatial domain, we use an overcomplete dictionary which is constructed by discretizing the angle space and then synthesizing array outputs for each discrete angle. As the outputs of the parasitic elements cannot be observed, instead they are electronically combined and collected from the sole active element. To this end, the sparse signal in the ESPAR array is considered to be projected on to a set of directional beampatterns; that is equivalent to introducing a projection matrix in the sparse signal representation. Finally, the recovery of the sparse signal spectrum can be solved by the l_1-SVD multiple measurement vectors (MMV) problem [11], which combines the SVD of the subspaces algorithms with the l_1-norm relaxation for sparse spectrum recovery and can be reformulated as a SOCP problem.

5.1 Two-Stage Spatial Spectrum Sensing with ESPAR Antennas

5.1.1 System Model

In the CR system, an ESPAR antenna with $M+1$ elements is considered as the transceiver for a cognitive radio (i.e., SU), so the SU transmitter is capable of adaptive beamforming. Consequently, this CR system is ready to apply the new angle dimension in the spectrum resource. In this chapter, the ESPAR antenna works as a switched-beam antenna, as described in Chapter 2, Section 2.3. Recall that an $(M+1)$-element ESPAR antenna is able to form M sector beampatterns dividing the whole angle space into M sectors.

Here, we focus on the far-field narrowband scenario; thus, source signals can be modeled as point sources. Assume that there are $P(P \leq M)$ PUs in the geographic area under consideration, where signal $s_p(t)$ is from the direction θ_p, $p \in \{1, \cdots, P\}$. During the sensing period, the ESPAR receiver scans its whole angle space via M sector beampatterns formed on a time division basis. The M sector beampatterns are denoted by $B_m(\theta) = \boldsymbol{w}_m^T \boldsymbol{a}(\theta)$, with the maximum beam gain at $\phi_m = (m-1)2\pi/M$, $m = \{1, \cdots, M\}$. Thus, the receiver obtains measurements via M sector beampatterns written in the M-dimensional $\boldsymbol{y} = [y_1, \cdots, y_m, \cdots, y_M]^T$. The signal received over the m-th sector beampattern is given by

$$
\begin{aligned}
y_m(t) &= \sum_{p=1}^{P} B_m(\theta_p) s_p(t) + e_m(t) \\
&= \sum_{p=1}^{P} \boldsymbol{w}_m^T \boldsymbol{a}(\theta_p) s_p(t) + e_m(t), \quad m = \{1, \cdots, M\},
\end{aligned}
\tag{5.1}
$$
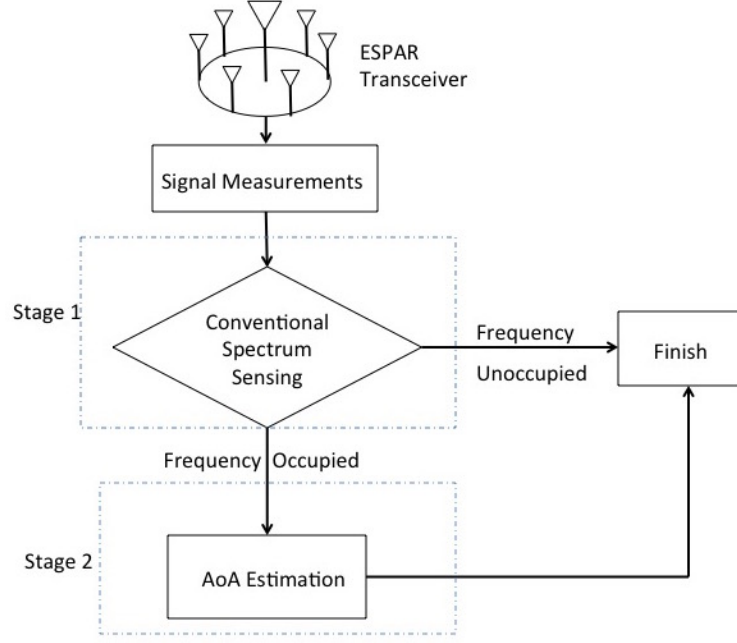
FIGURE 5.1: Diagram for two-stage spatial spectrum sensing.

where $e_m(t)$ $(e_m(t) \sim \mathcal{CN}(0, \sigma_e^2))$ are additive noises assumed to be uncorrelated to source signals $s_p(t)$. The receive SNR at the m-th beampattern is given as

$$SNR_m = \frac{1}{\sigma_e^2} \left(\sum_{p=1}^{P} P_{t,p} |B_m(\theta_p)|^2 \right), \tag{5.2}$$

where $P_{t,p}$ is the power of the p-th source signal.

5.1.2 Two-Stage Spatial Spectrum Sensing

In this CR system, we employ a two-stage *spatial spectrum sensing* method based on the ESPAR antenna, which is used in [98, 99]. The diagram of the two-stage sensing method is shown in Figure 5.1. At the first stage, the ESPAR receiver senses the channel to detect whether the frequency subband is occupied by PUs at a certain time in a given region, using conventional spectrum sensing algorithms which are referred to as *temporal spectrum sensing*. In particular, the energy detector and the eigenvalue-based detectors are considered at the first stage. If the decision is made that primary signals are absent, sensing is finished; otherwise, we go to the next stage. At the second stage, the ESPAR estimates the AoAs of the

existing primary signals using the high-resolution algorithms. The AoA estimation method via the sparse signal reconstruction, especially, is studied for the ESPAR antenna, and is compared to the RD-MUSIC algorithm. As a result, the spectrum white space is found to be all directions in the absence of the PUs, or the different directions causing no interference to the PUs when the PUs are present.

5.2   Temporal Spectrum Sensing

At the first stage of *spatial spectrum sensing*, the ESPAR receiver detects occupancy by the PU over a specific subband at a certain time in a geographic area. A number of different sensing approaches have been developed for *temporal spectrum sensing*. Each method has its own performance advantages and disadvantages for the sensing scenario [35].

In [44, 45, 99], sensing methods (including energy detector and eigenvalue-based techniques) have been studied for the switched-beam ESPAR receiver. It is demonstrated that the switched-beam ESPAR antenna is suited to be an alternative for spectrum sensing applied by compact CR terminals. Furthermore, the use of directional beampatterns helps to improve sensing performance (when compared to that using isotropic beampattern), by increasing receive SNR. Here, we simply review these *temporal spectrum sensing* methods for use at the first stage of *spatial spectrum sensing*.

5.2.1   Problem Formulation

In the *temporal spectrum sensing* problem, the decision on the occupancy of a frequency subband can be made by comparing the test statistics $\mathcal{T}$ (also called the decision metric) against a fixed threshold κ. This is equivalent to distinguishing between two hypotheses: $\mathcal{H}_0$, absence of primary signals; $\mathcal{H}_1$, presence of primary signals. For the CR receiver exploiting M sector beampatterns, the two hypotheses

are mathematically written as

$$\mathcal{H}_0: \quad y_m(t) = e_m(t), \quad m = \{1, \cdots, M\}, \tag{5.3a}$$

$$\mathcal{H}_1: \quad y_m(t) = \sum_{p=1}^{P} B_m(\theta_p)s_p(t) + e_m(t), \quad m = \{1, \cdots, M\}. \tag{5.3b}$$

The performance of a specific sensing algorithm is summarized by two probabilities: probability of detection P_D and probability of false alarm P_F. P_D is the probability of deciding that the frequency subband is occupied when the primary signals are truly present (under $\mathcal{H}_1$). Thus, a large value of P_D is desired. P_D is formulated as

$$P_D = Prob\{\mathcal{T} > \kappa | \mathcal{H}_1\} = \int_{t_0}^{\infty} f_1(t)dt, \tag{5.4}$$

where $f_1(t)$ is the PDF of the test statistics $\mathcal{T}$ under $\mathcal{H}_1$. P_F is the probability of deciding that the frequency subband is occupied when the primary signals actually are absent (under $\mathcal{H}_0$). Thus, P_F is required to be as small as possible. P_F can be written as

$$P_F = Prob\{\mathcal{T} > \kappa | \mathcal{H}_0\} = \int_{t_0}^{\infty} f_0(t)dt, \tag{5.5}$$

where $f_0(t)$ is the PDF of the test statistics $\mathcal{T}$ under $\mathcal{H}_0$.

In the following sections, we summarize the test statistics $\mathcal{T}$ and thresholds κ for energy detector and eigenvalue-based algorithms based on the switched-beam ESPAR receiver, which are proposed in [44, 45, 99].

5.2.2 Energy Detector

In the energy detector, the test statistic is formulated as the received power over one sector beampattern (e.g., $B_m(\theta)$) integrated over the observation time interval $[0, T]$, which can be approximated as [44]

$$\mathcal{T}_m = \int_0^T |y_m(t)|^2 dt \approx \sum_{i=1}^{N_s} |y_m(i)|^2, \tag{5.6}$$

where $y_m(i)$ is the i-th sample of $y_m(t)$ and N_s is the number of samples.

When the primary signals are absent (under $\mathcal{H}_0$), $\mathcal{T}_m$ is the sum of N_s squared AWGNs, i.e., Gaussian variables with zero-mean and variance σ_e^2. Thus, the test statistic follows a central chi-square distribution with $2N_s$ DoFs. According to the CDF of $\mathcal{T}_m$, the probability of false alarm is given by [100]

$$P_{F,m} = Prob\{\mathcal{T}_m > \kappa | \mathcal{H}_0\} = \frac{\Gamma(\frac{N_s}{2}, \frac{\kappa}{2\sigma_e^2})}{\Gamma(\frac{N_s}{2})}, \tag{5.7}$$

where $\Gamma(\cdot)$ and $\Gamma(\cdot, \cdot)$ are the Gamma function and the unregularized upper incomplete Gamma function, respectively [101]. Similarly, when the primary signals are present (under $\mathcal{H}_1$), the test statistic $\mathcal{T}_m$ follows a chi-square distribution with a non-centrality parameter $N_s \cdot SNR_m$ (SNR_m is given in (5.2)), and thus, according to the CDF of the test statistic, the probability of detection is calculated as [100]

$$P_{D,m} = Prob\{\mathcal{T}_m > \kappa | \mathcal{H}_1\} = Q_{N_s/2}\left(\sqrt{N_s \cdot SNR_m}, \sqrt{\frac{\kappa}{\sigma_e^2}}\right), \tag{5.8}$$

where $Q_a(\cdot, \cdot)$ is the generalized Marcum Q-function [101].

It is observed that $P_{F,m}$ given in (5.7) is not related to the receive SNR, since primary signals are not present. On the contrary, $P_{D,m}$ is a function of SNR_m. Therefore, using the sector beampattern can increase the receive SNR for some directions, thereby improving the sensing performance. Indeed, in the energy detector, only one sector beampattern is needed to fulfil sensing function, since there is no requirement for the correlation matrix to receive signals in the algorithm. However, since the M sector beampatterns access different angular sectors, sensing performance obtained via only one sector beampattern may be poor when the directions of primary signals do not occur in that angular sector. Here, the CR receiver is assumed to scan the whole angle space via M sector beampatterns, and to perform energy detection over each sector beampattern to obtain the probabilities of detection $P_{D,m}, m = \{1, \cdots, M\}$. Finally, the probability of detection is

the largest one, i.e.,

$$P_D = \max_{m \in \{1, \cdots, M\}} P_{D,m}. \tag{5.9}$$

The threshold κ can be selected for finding an optimum balance between P_D and P_F [35]. In practice, κ is selected to achieve a certain false alarm rate [102].

5.2.3 Eigenvalue-Based Detection

In the eigenvalue-based technique, the correlation matrix of the receive signal is required. Thus, the RD technique is used to ensure that each of P primary signals is correlated across M sector beampatterns. The statistical correlated matrix of signals obtained by the switched-beam ESPAR receiver under two hypotheses can be expressed as

$$\boldsymbol{R}_{yy} = \mathbb{E}\{\boldsymbol{y}\boldsymbol{y}^H\} = \begin{cases} \boldsymbol{B}(\boldsymbol{\theta})\boldsymbol{\Sigma}\boldsymbol{B}^H(\boldsymbol{\theta}) + \sigma_e^2 \boldsymbol{I}_M & \mathcal{H}_1 \\ \sigma_e^2 \boldsymbol{I}_M & \mathcal{H}_0 \end{cases} \tag{5.10}$$

where the (m,p)-th element of the matrix $\boldsymbol{B}(\boldsymbol{\theta}) \in \mathbb{C}^{M \times P}$ is $B_m(\theta_p) = \boldsymbol{w}_m^T \boldsymbol{a}(\theta_p)$, i.e., the farfield response of the m-th beampattern due to the p-th source signal. $\boldsymbol{\Sigma} \in \mathbb{R}^{P \times P}$ is a diagonal matrix containing powers of P primary signals as diagonal entries. The matrix $\boldsymbol{B}(\boldsymbol{\theta})$ can be considered as the *manifold matrix* as that in the conventional DBF array.

Note that the above correlation matrix $\boldsymbol{R}_{yy}$ is the ideal asymptotic representation for the infinite sample case. In practice, we can only obtain finite samples during a sensing period. Therefore, the estimate correlation matrix denoted by $\hat{\boldsymbol{R}}_{yy}$ is used to replace the ideal correlation matrix $\boldsymbol{R}_{yy}$ in the following description. Let the receiver collect N_s sample vectors, $\boldsymbol{y}(1), \boldsymbol{y}(2), \cdots, \boldsymbol{y}(N_s)$, each with M elements sampled via M sector beampatterns. Then, we have the estimate correlation matrix, as follows:

$$\hat{\boldsymbol{R}}_{yy} = \frac{1}{N_s} \sum_{i=1}^{N_s} \boldsymbol{y}(i)\boldsymbol{y}(i)^H. \tag{5.11}$$

For the noise only case (under $\mathcal{H}_0$), the estimate correlation matrix of the received signals becomes the complex Wishart matrix, represented by

$$\hat{\boldsymbol{R}}_{ee} = \frac{1}{N_s} \sum_i^{N_s} \boldsymbol{e}(i)\boldsymbol{e}(i)^H, \tag{5.12}$$

where the M-dimensional vector $\boldsymbol{e}(i) = [e_1(i), e_2(i), \cdots, e_M(i)]^T$ contains noises seen by M sector beampatterns, which are assumed to be uncorrelated across beampatterns. Let $\boldsymbol{E} \in \mathbb{C}^{M \times N_s}$ be the matrix with $\boldsymbol{e}(i)$ as columns (i.e., $\boldsymbol{E} \sim \mathcal{CN}(\boldsymbol{0}, \sigma_e^2 \boldsymbol{I}_M \otimes \boldsymbol{I}_{N_s})$), and thus (5.12) is rewritten as [45]

$$N_s \hat{\boldsymbol{R}}_{ee} = \boldsymbol{E}\boldsymbol{E}^H = \boldsymbol{\mathcal{W}}, \tag{5.13}$$

where $\boldsymbol{\mathcal{W}}$ is the complex central Wishart matrix and its distribution is denoted by $\mathcal{CW}_M(N_s, \sigma_e^2 \boldsymbol{I}_M)$ [103].

Under $\mathcal{H}_0$, the eigenvalues of $\hat{\boldsymbol{R}}_{yy}$, $\lambda_{max} = \lambda_1 > \lambda_2 > \cdots > \lambda_M = \lambda_{min}$, are all equal to noise power, i.e., $\lambda_{i|\mathcal{H}_0} = \sigma_e^2, \forall i$. Under $\mathcal{H}_1$, the eigenvalues become

$$\lambda_{i|\mathcal{H}_1} = \begin{cases} \sigma_i^2 + \sigma_e^2 & 1 \leq i \leq P \\ \sigma_e^2 & P+1 \leq i \leq M, \end{cases} \tag{5.14}$$

where $\sigma_p^2, p = \{1, \cdots, P\}$ represents the received power of the p-th primary signal. It is clear that the eigenvalues of $\hat{\boldsymbol{R}}_{yy}$ are suitable to be employed as a test statistic for distinguishing the two hypotheses $\mathcal{H}_1$ and $\mathcal{H}_0$.

A number of eigenvalue-based detection algorithms have been developed, including the maximum eigenvalue (MAX), maximum-minimum eigenvalue (MME), energy to minimum eigenvalue detector (EME) and blind general likelihood ratio test method (BGLRT) [4, 5]. We summarize their test statistics and estimation thresholds in Table 5.1. It is noted that, in the thresholds presented, only κ_{MAX} is related to the noise power, whereas the other eigenvalue-based algorithms are insensitive to noise uncertainty.

TABLE 5.1: Test statistics and thresholds for eigenvalue-based detectors [4, 5]

Algorithm	Test statistics	Thresholds
MAX	$\mathcal{T}_{MAX} = \lambda_1 \begin{cases} = \sigma_e^2, & \mathcal{H}_0 \\ > \sigma_e^2, & \mathcal{H}_1 \end{cases}$	$\kappa_{MAX} = \sigma_e^2$
MME	$\mathcal{T}_{MME} = \frac{\lambda_1}{\lambda_M} \begin{cases} = 1, & \mathcal{H}_0 \\ > 1, & \mathcal{H}_1 \end{cases}$	$\kappa_{MME} = 1$
EME	$\mathcal{T}_{EME} = \frac{\sum_{i=1}^{M} \lambda_i}{\lambda_M} \begin{cases} = M, & \mathcal{H}_0 \\ > M, & \mathcal{H}_1 \end{cases}$	$\kappa_{EME} = M$
BGLRT	$\mathcal{T}_{BGLRT} = \frac{\lambda_1}{\sum_{i=1}^{M} \lambda_i} \begin{cases} = \frac{1}{M}, & \mathcal{H}_0 \\ > \frac{1}{M}, & \mathcal{H}_1 \end{cases}$	$\kappa_{BGLRT} = \frac{1}{M}$

5.3 Angle-of-Arrival Estimation

Although study of the AoA estimation based on the ESPAR antenna is not suffi-cient, there has been increasing interest in this field. The earliest attempt at AoA estimation with a seven-element ESPAR antenna is discussed in [104]: a power maximizing method is proposed. Twelve directional beampatterns are predeter-mined by means of different sets of reactance values, then an AoA is estimated as the look direction of the beampattern with the highest output power. However, with twelve beam-steering angles equally distributed in the full azimuth plane, this simple method is able to detect only one incoming signal with a coarse precision of 30°. To improve precision of the AoA estimation without increasing receiver complexity in the ESPAR array, Taillefer et al. [105] proposed a power pattern cross-correlation method, exploiting the correlation between a number of mea-sured beampatterns and the corresponding power outputs of the antenna. Similar to the power maximizing method, the power pattern cross-correlation method is only applicable for the scenario with one source signal; moreover, if the antenna cannot form narrower beampatterns, this method still suffers from low precision capabilities.

In [106], the authors investigated the possibility of employing the high-resolution MUSIC algorithm for the switched parasitic antenna, where directional beampat-terns, formed by switching the short circuits connected to the parasitic elements, are used. As mentioned earlier, the ESPAR antenna, which is reactance-assisted,

is more flexible in beamforming than the switched parasitic antenna [107, 108]. The RD technique allows an ESPAR antenna to obtain a correlation matrix from the single-port output. Based on this, the conventional subspace algorithms such as MUSIC and ESPRIT are thus modified as RD-MUSIC [43, 96] and RD-ESPRIT [53, 54] for the ESPAR antenna, estimating directions of multiple incoming signals. Although RD-MUSIC and RD-ESPRIT have been demonstrated to be high-resolution AoA estimation methods applicable for the ESPAR array, they rely on the statistical properties of the data, and thus need a sufficiently large number of samples for accurate estimation. Moreover, in order to obtain the correlation matrix, in the RD-MUSIC and RD-ESPRIT algorithms, the same data information is required to be repeated as often as the number of beampatterns used, thereby reducing the transmission rate.

Recently, the emerging field of CS has provided an alternative solution to the AoA estimation problem with super resolution, while using only a small number of samples. In [109], the authors proposed a recursive weighted minimum-norm algorithm termed "FOCUSS" to achieve the sparse representation of the AoA estimation problem. Cotter [110] combines the multiple measurement vectors (MMV) and matching pursuit (MP) as a solution to a joint-sparse recovery problem in AoA estimation. The l_1-SVD algorithm developed by Mlioutov et al. [11] is one popular sparsity recovery method for AoA estimation. It combines the SVD of the subspace algorithms with the l_1-norm relaxation for sparse spectrum recovery. It is noted that these studies consider a DBF array as the sensor array.

To reduce the cost for AoA estimation in the ESPAR array, while providing high-resolution and robust performance, we study the AoA estimation problem via the sparse signal representation problem for the ESPAR antenna. Moreover, this method does not reduce transmission rate, as the RD-based subspace methods do. In this part, we first summarize the RD-MUSIC algorithm as the representative of the subspace direction sensing method for the ESPAR antenna. Then, we present the sparse signal representation for the AoA estimation with the ESPAR antenna.

5.3.1 Problem Formulation

The goal of AoA estimation with an antenna array is to find the directions of the source signals impinging on the array. Since we are familiar with the array signal processing in a DBF array, we can consider the switched-beam ESPAR antenna, switching between M sector beampatterns as a virtual array with M active elements in the beam domain (equivalent to reactance domain). Under the condition that the presence of P primary signals (from directions $\boldsymbol{\theta} = [\theta_1, \cdots, \theta_P]$) have been detected at the first stage, we have the measurements on the virtual M-element array taking the following form

$$\boldsymbol{y}(t) = \boldsymbol{B}(\boldsymbol{\theta})\boldsymbol{s}(t) + \boldsymbol{e}(t), \tag{5.15}$$

where $\boldsymbol{y}(t) = [y_1(t_1), \cdots, y_M(t_M)]^T$, and similarly $\boldsymbol{s}(t) = [s_1(t), \cdots, s_P(t)]^T$ and $\boldsymbol{e}(t) = [e_1(t_1), \cdots, e_M(t_M)]^T$. The matrix $\boldsymbol{B}(\boldsymbol{\theta}) \in \mathbb{C}^{M \times P}$ is analogous to the *manifold matrix*, whose (m, p)-th element represents the delay and gain information from the p-th source to the m-th virtual element. The columns $\boldsymbol{a}_{rd}(\theta_p), p = \{1, \cdots, P\}$, of $\boldsymbol{B}(\boldsymbol{\theta})$, are thus the *steering vectors* in reactance domain. $\boldsymbol{B}(\boldsymbol{\theta})$ is unknown, since it depends on unknown source directions $\boldsymbol{\theta}$. Given the measurements $\boldsymbol{y}(t)$ and the mapping $\boldsymbol{\theta} \to \boldsymbol{B}(\boldsymbol{\theta})$, the goal is to find $\theta_p, \forall p$. This is a nonlinear parameter estimation problem. In this work, we assume that the number P (the number of the existing PUs) is known.

5.3.2 Reactance-Domain MUSIC Algorithm

The MUSIC algorithm [9] utilizes the eigenstructure of the array correlation matrix of the form

$$\hat{\boldsymbol{R}}_{yy} = \frac{1}{N_s} \sum_{i=1}^{N_s} \boldsymbol{y}(i)\boldsymbol{y}^H(i) = \boldsymbol{B}(\boldsymbol{\theta})\boldsymbol{\Sigma}\boldsymbol{B}^H(\boldsymbol{\theta}) + \sigma_e^2 \boldsymbol{I}_M. \tag{5.16}$$

The underlying idea is to separate the signal and noise subspaces spanned by their corresponding eigenvectors. Performing the eigenvalue decomposition of $\hat{\boldsymbol{R}}_{yy}$, we

obtain

$$\hat{\boldsymbol{R}}_{yy} = \boldsymbol{Q}\boldsymbol{\Lambda}\boldsymbol{Q}^H$$
$$= \boldsymbol{Q}_s\boldsymbol{\Lambda}\boldsymbol{Q}_s^H + \sigma_e^2\boldsymbol{Q}_e\boldsymbol{Q}_e^H, \tag{5.17}$$

where $\boldsymbol{Q}$ and $\boldsymbol{\Lambda}$ form the eigenvalue decomposition of $\hat{\boldsymbol{R}}_{yy}$. Similarly, $\boldsymbol{Q}_s$ and $\boldsymbol{\Lambda}_s$ represent the eigen-space spanned by the primary signals, while the eigen-space spanned by noise is expressed by $\boldsymbol{Q}_e$ and $\boldsymbol{\Lambda}_e = \sigma_e^2\boldsymbol{I}_{(M-P)}$. Since $M \geq P$ and providing non-singular $\boldsymbol{\Sigma}$, the matrix $\boldsymbol{B}(\boldsymbol{\theta})\boldsymbol{\Sigma}\boldsymbol{B}^H(\boldsymbol{\theta})$ has a rank of P. Consequently, the first P eigenvalues of $\hat{\boldsymbol{R}}_{yy}$ result from the combined signal plus noise subspace, and the remaining $M - P$ eigenvalues result from the noise subspace alone. Mathematically, this is represented as

$$\hat{\boldsymbol{R}}_{yy} = \sum_{m=1}^{P}(\hat{\lambda}_m + \sigma_e^2)\boldsymbol{q}_m\boldsymbol{q}_m^H + \sigma_e^2\sum_{m=P+1}^{M}\boldsymbol{q}_m\boldsymbol{q}_m^H, \tag{5.18}$$

where $\hat{\lambda}_m, m = \{1, \cdots, P\}$ is the eigenvalues of the signal subspace, i.e., the diagonal entries of $\boldsymbol{\Lambda}_s$, and $\boldsymbol{q}_m$ is the eigenvector, that is, the m-th column of the matrix $\boldsymbol{Q}$. This information is used to separate two eigen-subspaces spanned by the signal and noise, respectively.

Once the noise subspace has been found, the signal directions can be computed according to the orthogonality between the noise subspace and the *manifold matrix,* i.e., $\boldsymbol{B}^H(\boldsymbol{\theta})\boldsymbol{Q}_e = 0$. Notice that the *steering vector* contained in $\boldsymbol{B}(\boldsymbol{\theta})$ is equivalent to that in the RD technique $\boldsymbol{a}_{rd}(\theta_p)$ (see Chapter 2). Thus, the spectrum of the RD-MUSIC is computed as

$$P_{MU}(\theta) = \frac{1}{\boldsymbol{a}_{rd}^H(\theta)\boldsymbol{Q}_e\boldsymbol{Q}_e^H\boldsymbol{a}_{rd}(\theta)}. \tag{5.19}$$

The directions of the present primary signals are estimated as peaks in the computed MUSIC spectrum $P_{MU}(\theta)$.

5.3.3 Compressive Sensing-based AoA Estimation

Compressive sensing deals with the recovery of a high-dimensional sparse signal vector from a low-dimensional linear measurement vector [97, 111]. We begin by proposing the sparse signal representation of the AoA estimation problem based on an ESPAR antenna. We then present a numerical solution to recovery of the sparse signal spectrum.

1) Overcomplete Representation for a Single Snapshot

In compressive sensing theory, a different framework is used. We begin by formulating the AoA estimation problem as a sparse representation problem for a single snapshot. The single-snapshot formulation in this section modifies the one in [11, 109], which was presented based on the DBF array, where the sparse signal is represented in terms of an overcomplete dictionary.

For a conventional DBF array with M elements (e.g., an M-element ULA), the overcomplete dictionary is constructed as follows. First, discretize the whole azimuth plane of the receive antenna into a sampling grid of all potential AoAs denoted as the vector $\tilde{\boldsymbol{\theta}} = [\tilde{\theta}_1, \tilde{\theta}_2, \cdots, \tilde{\theta}_{N_\theta}]$, where the number of all AoAs of interest (N_θ) is typically much larger than the number of source signals and the number of sensors, i.e., $N_\theta \gg P$ and $N_\theta \gg M$. The overcomplete dictionary is thus constructed as a matrix composed of steering vectors corresponding to N_θ potential AoAs, i.e., $\tilde{\boldsymbol{A}} = [\boldsymbol{a}(\tilde{\theta}_1), \boldsymbol{a}(\tilde{\theta}_2), \cdots, \boldsymbol{a}(\tilde{\theta}_{N_\theta})]$. In this framework, $\tilde{\boldsymbol{A}}$ is known and does not depend on the true source AoAs $\boldsymbol{\theta} = [\theta_1, \cdots, \theta_P]$.

The sparse signal field is presented as an N_θ-dimensional vector $\tilde{\boldsymbol{s}}(t)$, whose n-th element is nonzero and equal to the p-th source signal when it occurs for that potential direction; that is,

$$\tilde{s}_n(t) = \begin{cases} s_p(t) & \tilde{\theta}_n = \theta_p, \\ 0 & otherwise, \end{cases} \tag{5.20}$$

where $n = \{1, 2, \cdots, N_\theta\}$, and $p = \{1, 2, \cdots, P\}$. Thus, the vector $\tilde{\boldsymbol{s}}(t)$ is P-sparse. For a single snapshot, the problem is reduced to

$$\boldsymbol{y} = \tilde{\boldsymbol{A}}\tilde{\boldsymbol{s}} + \boldsymbol{e}, \tag{5.21}$$

where $\boldsymbol{y} \in \mathbb{C}^{M \times 1}$ represent measurements from the M-element DBF array, and $\boldsymbol{e} \in \mathbb{C}^{M \times}$ is the additive noise vector. Consequently, in a conventional DBF array, the use of the overcomplete dictionary $\tilde{\boldsymbol{A}}$ allows one to transform the problem of parameter estimation of $\boldsymbol{\theta}$ to the problem of sparse spectrum estimation of $\tilde{\boldsymbol{s}}$.

Note that the equality $\tilde{\theta}_n = \theta_p$ may not occur in practice from $n \in \{1, \cdots, N_\theta\}$. In other words, the angle grid $\tilde{\boldsymbol{\theta}}$ cannot include all potential AoAs, so source direction might be off grid. To solve the problem, one approach is to make the angle grid in $\tilde{\boldsymbol{A}}$ dense enough to ensure $\tilde{\theta}_n \approx \theta_p$ closely. The remaining modelling error is assumed to be included in $\boldsymbol{z}$. However, this method will increase computation complexity. Another approach is the adaptive grid refinement developed in [11]. The main idea of this method is that the refinement of the grid is only performed around the regions where source signals are presented; where the source signals positions are estimated, using an original rough grid.

Unlike a DBF array, in the ESPAR array, signals impinging on the parasitic elements cannot be observed and processed. Instead, they are electronically combined to the sole active element. Our goal is thus to recreate the spatial diversity with a single-active ESPAR antenna analogous to that derived from outputs of individual elements in a DBF array. The ESPAR antenna possesses M tunable reactances. It is known that, when we specify a set of reactance loads $\hat{\boldsymbol{x}}_1$ (thus a directional beampattern defined by $\boldsymbol{w}_1$), one corresponding measurement $y_1(t)$ is obtained (see the signal model (5.1) and ESPAR modelling (2.6)). Then, we can change to a different set of reactance loads $\hat{\boldsymbol{x}}_2$ (thus $\boldsymbol{w}_2$) to obtain a measurement $y_2(t)$. By repeating this process M times, we can obtain M measurements where spatial diversity is recreated. To avoid noise enhancement resulting from fast switching between M directional beampatterns within a symbol period, here we exploit each of the M directional beampatterns in one sampling period. Unlike the RD-MUSIC

algorithm, a receive signal is not required to be correlated across the used directional beampatterns. Therefore, in this method the same information data is not required to be repeated during scanning throughout M beampatterns. We only assume that, during the block of M sampling periods, the directions of the P source signals are unchanged.

The above procedure is mathematically equal to introducing a projection matrix $\boldsymbol{W} = [\boldsymbol{w}_1, \cdots, \boldsymbol{w}_M]^T \in \mathbb{C}^{M \times (M+1)}$, where each row is an equivalent weight vector defining one directional beampattern. Thus, the sparse representation of the AoA estimation problem in the ESPAR antenna is given by

$$\boldsymbol{y} = \boldsymbol{W}\tilde{\boldsymbol{A}}\tilde{\boldsymbol{s}} + \boldsymbol{e}. \tag{5.22}$$

It is noted that, although we express the sparse representation problem (5.22) as a "single snapshot" form for simplicity, it indeed requires a total of M periods to achieve. Thus, the latency of the estimation of an ESPAR antenna increases with M, when compared with the conventional DFB array.

In a sparse representation problem, the sparsity of $\tilde{\boldsymbol{s}}$ is significant, unless this problem is ill-posed. An ideal measure of the sparsity is the count of the number of nonzero elements in $\tilde{\boldsymbol{s}}$, which is denoted by the l_0-norm ($\|\tilde{\boldsymbol{s}}\|_0$). Mathematically, recovering the sparse spectrum $\tilde{\boldsymbol{s}}$ is to find the sparest solution by solving the following optimization problem:

$$(P_0) \quad \min_{\tilde{\boldsymbol{s}}} \|\tilde{\boldsymbol{s}}\|_0 \quad s.t. \quad \|\boldsymbol{y} - \boldsymbol{W}\tilde{\boldsymbol{A}}\tilde{\boldsymbol{s}}\|^2 \le \epsilon, \tag{5.23}$$

where ϵ is a parameter determining the level of the acceptable error. However, problem (P_0) is in general NP-hard, since solving this problem essentially requires exhaustive searching over all subsets of columns of $\boldsymbol{W}\tilde{\boldsymbol{A}}$, which is intractable for even a moderately sized problem [112].

Over the past decades, many approximations have been developed for alternative solutions to the problem (P_0), including greedy approximations (e.g., matching

pursuit [113], stepwise regression [114] and their variants) and the l_1-norm and l_p-norm ($p < 1$) relaxations [115, 116]. It has been verified that if $\tilde{s}$ is "sparse enough" with respect to the overcomplete dictionary/orthogonal basis, the approximations are able to provide the exact solutions.

In many researches, the l_1-norm relaxation is of interest, since the optimization problem is a convex and global optimum, and there is no initialization in this approximation. The objective function of the l_p-norm relaxation is nonconvex, and its convergence to a global minimum is thus not guaranteed. The unconstrained objective of the l_1-norm relaxation is expressed as [117, 118]

$$(P_1) \quad \min_{\tilde{s}} \quad \|\boldsymbol{y} - \boldsymbol{W}\tilde{\boldsymbol{A}}\tilde{\boldsymbol{s}}\|^2 + \beta\|\tilde{\boldsymbol{s}}\|_1. \qquad (5.24)$$

The l_2-norm forces the residual $\boldsymbol{y} - \boldsymbol{W}\tilde{\boldsymbol{A}}\tilde{\boldsymbol{s}}$ to be small, whereas the l_1-norm ($\|\tilde{\boldsymbol{s}}\|_1 = \sum_{n=1}^{N_\theta} |\tilde{s}_n|$) enforces sparsity of the representation. The parameter β controls the trade-off between the residual norm and the sparsity of the spectrum. This l_1-norm minimization problem is also known as the basis pursuit (BP) or basis pursuit denoise (BPDN) problem.

For real-valued data, a numerical solution to (5.24) can be readily found by quadratic programming [115, 119]. For complex data, the problem (P_1) can be reformulated as a SOCP problem, as presented in [11, 116].

2) Projection Matrix

The early work on CS assumes that the projection matrix is drawn at random, e.g., Gaussian and Bernoulli (binary) matrices; this has been proved for exact recovery of sparse spectrum with overwhelming probability [120–123]. However, the projection matrix in our work has a specific meaning: $\boldsymbol{W}$ is comprised of M equivalent weight vectors corresponding to M directional beampatterns (or M different sets of reactance loads). With regard to the relation between the reactance loads and the equivalent weight vector (see (2.6)), it is a complicate work to construct a matrix $\boldsymbol{W}$ whose elements are drawn from the i.i.d Gaussian

entries or ± 1, by tuning the reactance loads of the parasitic elements. This imposes difficulty for the employment of a random projection matrix in this work.

For the projection matrix $\boldsymbol{W}$, we known that it is related to M directional beampatterns formed by the ESPAR antenna. Thus, the use of the matrix $\boldsymbol{W}$ projects the sparse signal into measurement outputs of directional beampatterns: that is, it projects the sparse signal into beamspace. Therefore, design of the projection matrix $\boldsymbol{W}$ is the same as designing M beampatterns of the ESPAR antenna by adjusting reactance loads.

We design the directional beampatterns (thus $\boldsymbol{W}$) as follows. First, the reactance loads of parasitic elements are optimized for directivity in a look direction. Then, due to the symmetrical antenna structure, circular permutations of the optimized reactance loads rotate the beampattern to different angular positions, dividing the whole angle space around the ESPAR receiver into several angular sectors. An $(M + 1)$-element ESPAR possesses M reactance variables; the permutation can be performed $M - 1$ times. As a consequence, it is able to form M directional beampatterns, each corresponding to one angular sector, that is, sector beampatterns. Therefore, the projection matrix $\boldsymbol{W}$ defined by the M sector beampatterns is used to enable an ESPAR antenna to scan its whole angle space; moreover, the use of directional beampatterns helps to enhance the receive SNR.

3) AoA Estimation with Multiple Snapshots

Although single snapshot processing has been widely discussed in some CS systems, in the DoA estimation problem, signal processing with multiple snapshots is more practical.

Repeating the procedure to obtain a single snapshot (described in the previous section) N_s times, we can obtain N_s measurement vectors denoted by the $M \times N_s$ matrix $\boldsymbol{Y} = [\boldsymbol{y}(1), \boldsymbol{y}(2), \cdots, \boldsymbol{y}(N_s)]$, taking the following form

$$\boldsymbol{Y} = \boldsymbol{W}\tilde{\boldsymbol{A}}\tilde{\boldsymbol{S}} + \boldsymbol{E}, \tag{5.25}$$

where $\tilde{\boldsymbol{S}} = [\tilde{\boldsymbol{s}}(1), \tilde{\boldsymbol{s}}(2), \cdots, \tilde{\boldsymbol{s}}(N_s)]$ with each column containing P primary signals as non-zero elements, and similarly $\boldsymbol{E} = [\boldsymbol{e}(1), \boldsymbol{e}(2), \cdots, \boldsymbol{e}(N_s)]$. In this multi-snapshot model, we assume that the directions of primary signals $\boldsymbol{\theta}$ are time invariant; that is, during the N_s "snapshots", the locations of the existing primary signals do not change. Therefore, supports of $\tilde{\boldsymbol{s}}$ are fixed for all N_s snapshots. In other words, only P rows of $\tilde{\boldsymbol{S}}$ are dominant peaks. Such a matrix is called a jointly P-sparse matrix. In this context, the AoA estimation problem is transformed to the multiple measurement vectors (MMV) problem, which aims to recover $\tilde{\boldsymbol{S}}$ given $\boldsymbol{Y}$.

The MMV problem is generally solved by the mixed norm problem, expressed by

$$
\begin{aligned}
\min_{\tilde{\boldsymbol{S}}} \quad & \|\tilde{\boldsymbol{S}}\|_{p,q}, \\
s.t. \quad & \|\boldsymbol{Y} - \boldsymbol{W}\tilde{\boldsymbol{A}}\tilde{\boldsymbol{S}}\|_F^2 \le \epsilon,
\end{aligned}
\tag{5.26}
$$

where for some integers p, q the mixed norm $\|\tilde{\boldsymbol{S}}\|_{p,q}$ is defined as follows

$$
\|\tilde{\boldsymbol{S}}\|_{p,q} = \left[\sum_{i=1}^{M} \left(\sum_{j=1}^{N_s} \left| \tilde{\boldsymbol{S}}(i,j) \right|^p \right)^{q/p} \right]^{1/q}.
\tag{5.27}
$$

A number of numerical solutions to the above mixed norm problem have been sufficiently studied in the literature. Cotter et al. [124] use $p = 2, q \le 1$; Trop [125] works on $p = 1, q = \infty$; Eladar et al. [126] use $p = 2, q = 1$; in [127], the authors study $p = 2, q = 0$. These methods all show good recovery performance for the sparse spectrum.

In [11], a numerical method termed l_1-SVD is developed. In essence, it uses the mixed $l_{1,2}$ norm. In particular, the SVD of the measurements are operated before computing sparse signal spectrum, in order to reduce the dimensionality of the multiple measurement vectors. The, the reconstruction of the processed sparse signal model is formulated as l_1-norm relaxation problem, i.e., the l_1-norm is used to enforce sparsity while the Frobenius norm is used to minimize the error. This is a popular method widely used in CS systems for numerical solutions, since it

is convex, and it reduces the computation complexity. Therefore, we adopt this method as the numerical solution to the CS-based AoA estimation problem.

First, perform SVD of the measurement matrix $\boldsymbol{Y}$:

$$\boldsymbol{Y} = \boldsymbol{U}\boldsymbol{\Sigma}\boldsymbol{V}^H, \tag{5.28}$$

where $\boldsymbol{U} \in \mathbb{C}^{M \times M}$ and $\boldsymbol{V} \in \mathbb{C}^{N_s \times N_s}$ contain eigenvectors of $\boldsymbol{Y}\boldsymbol{Y}^H$ and $\boldsymbol{Y}^H\boldsymbol{Y}$, respectively. $\boldsymbol{\Sigma} \in \mathbb{R}^{M \times N_s}$ is a diagonal matrix with singular values as entries in a descending order. Then, one can construct a reduced $M \times P$ matrix given as $\boldsymbol{Y}_{svd} = \boldsymbol{U}\boldsymbol{\Sigma}\boldsymbol{D}_P = \boldsymbol{Y}\boldsymbol{V}\boldsymbol{D}_P$, where $\boldsymbol{D}_P = [\boldsymbol{I}_P, \boldsymbol{0}]^T$ with $P \times (N_s - P)$ zero matrix $\boldsymbol{0}$. Similarly, let $\tilde{\boldsymbol{S}}_{svd} = \tilde{\boldsymbol{S}}\boldsymbol{V}\boldsymbol{D}_P$ and $\boldsymbol{E}_{svd} = \boldsymbol{E}\boldsymbol{V}\boldsymbol{D}_P$. Thus, the reduced measurements are [11]

$$\boldsymbol{Y}_{svd} = \boldsymbol{W}\tilde{\boldsymbol{A}}\tilde{\boldsymbol{S}}_{svd} + \boldsymbol{E}_{svd}. \tag{5.29}$$

Define $\tilde{s}_i^{l_2} = \|[\tilde{\boldsymbol{S}}_{svd}(i,1), \tilde{\boldsymbol{S}}_{svd}(i,2), \cdots, \tilde{\boldsymbol{S}}_{svd}(i,N_s)]\|, i \in \{1, \cdots, N_\theta\}$, which is the Euclidean norm of the i-th row of the matrix $\tilde{\boldsymbol{S}}_{svd}$. As a result, one has the N_θ-dimensional vector $\tilde{\boldsymbol{s}}^{l_2} = [\tilde{s}_1^{l_2}, \tilde{s}_2^{l_2}, \cdots, \tilde{s}_{N_\theta}^{l_2}]^T$. It is clear that $\tilde{\boldsymbol{S}}_{svd}$ is still P-jointly sparse. Thus, the l_1 penalty can be imposed on the vector $\tilde{\boldsymbol{s}}^{l_2}$, and then recovering $\tilde{\boldsymbol{s}}^{l_2}$ is achieved by minimizing

$$\min \quad \|\boldsymbol{Y}_{svd} - \boldsymbol{W}\tilde{\boldsymbol{A}}\tilde{\boldsymbol{S}}_{svd}\|_F^2 + \beta\|\tilde{\boldsymbol{s}}^{l_2}\|_1. \tag{5.30}$$

The optimization problem given in (5.30) can be reformulated as the SOC programming, given in Appendix B.

5.4 Simulations

In this section we consider the *spatial spectrum sensing* performance using an ESPAR antenna with seven elements (one active element and six parasitic elements). The elements are assumed to be thin electrical dipoles with the length of a half-wavelength, and the array radius is set to a quarter-wavelength. As a consequence,

the mutual impedance matrix $\boldsymbol{Z}$ is calculated as given in Appendix A. To operate sensing function, a 7-element ESPAR antenna switches across 6 sector beampatterns for signal sampling. There are 6 DoF in this antenna array. The reactance loads for parasitic elements to form sector beampattern are chosen as table 5.2. Therefore, we compare performance of the ESPAR array to that of a 6-element UCA with a radius of $\lambda/2$. It is noted that the 7-element ESPAR antenna must perform spectrum sensing across 6 sector beampatterns sequentially, thus $6 \times N_s$ detection periods are required. In contrast, for the 6-element UCA to get $6 \times N_s$ samples N_s detection periods are sufficient because the 6 antennas in the array can simultaneously measure the signals in a single detection period. Therefore, the latency of the ESPAR sensing increases with 6.

TABLE 5.2: Reactance loads for a 7-element ESPAR antenna to form 6 sector beampatterns

Beam index	Look direction	Reactance loadings $\hat{\boldsymbol{x}}$
B_1	$0°$	$[-33.4, -160.7, 80.7, -160.1, -33.2, -71.9]$
B_2	$60°$	$[-71.9, -33.4, -160.7, 80.7, -160.1, -33.2]$
B_3	$120°$	$[-33.2, -71.9, -33.4, -160.7, 80.7, -160.1]$
B_4	$180°$	$[-160.1, -33.2, -71.9, -33.4, -160.7, 80.7]$
B_5	$240°$	$[80.7, -160.1, -33.2, -71.9, -33.4, -160.7]$
B_6	$300°$	$[-160.7, 80.7, -160.1, -33.2, -71.9, -33.4]$

5.4.1 Performance of Temporal Spectrum Sensing

In this section, we evaluate the performance of the *temporal spectrum sensing* used at the first stage. The following simulations consider two scenarios: 1) one PU in vicinity of the ESPAR receiver from the AoA $20°$; 2) there are two PUs presenting around the ESPAR receiver and their AoAs are $20°$ and $50°$, respectively. In the simulations in this section, each result is averaged from 1000 Monte-Carlo experiments.

We first consider the performance using the energy detector (ED) with varying SNR values under scenario 1, where the test threshold is chosen to achieve a target

$P_F = 0.1$. The results are depicted in Figure 5.2. It is observed that, in general, the ESPAR antenna outperforms the UCA, because the use of the sector beampatterns enhances the receive SNR, compared to that using the omni-directional antenna elements in the UCA. In the simulations, we consider the energy detector with noise power uncertainty, following the approach proposed in [128], where the noise uncertainty is uniformly distributed over an interval $[-\log_{10}(b), \log_{10}(b)]$, and is randomly generated at each Monte Carlo experiment. The bounds $(\log_{10}(b))$ on the noise uncertainty are set to 0.5 dB, 1 dB and 1.5 dB, respectively. We can see that the performance of the energy detector with both the ESPAR and UCA is affected significantly by the noise uncertainty. Moreover, the reduction of the sampling numbers N_s also decreases the values of P_D for both the ESPAR and UCA.

In Figure 5.3 we show the probability of detection of the eigenvalue-based detectors versus varying SNRs, under scenario 1. Again, the results suggest the superiority of the ESPAR antenna over the UCA, using the eigenvalue-based detectors. The reason for this is the same as with the use of the energy detector. However, the performance gains provided by the ESPAR antenna using the eigenvalue-based detectors are smaller than those using the energy detector without noise uncertainty, since the probability of detection by the energy detector (given in equation (5.8)) is directly related to the receive SNR. It is also seen from the figure that the reduction of sampling numbers affects the sensing performance. In Figure 5.4, we evaluate the performance of the MAX and MME detectors with the noise uncertainty as described for the energy detector. It demonstrates that the MAX detector is susceptible to noise uncertainty, while the MME detector is not affected, because its test statistic form cancels the noise uncertainty parameter (see Table 5.1). It is clear that the EME and BLGRT detectors have the same property as the MME algorithm.

Finally, we evaluate the performance of the energy detector and MME detector (as the representative of the eigenvalue-based techniques) under scenario 2, where SNRs for both source signals are equal and $P_F = 0.1$. It is observed from Figure 5.5 that when 2 PUs are present the sensing performance has trends similar to
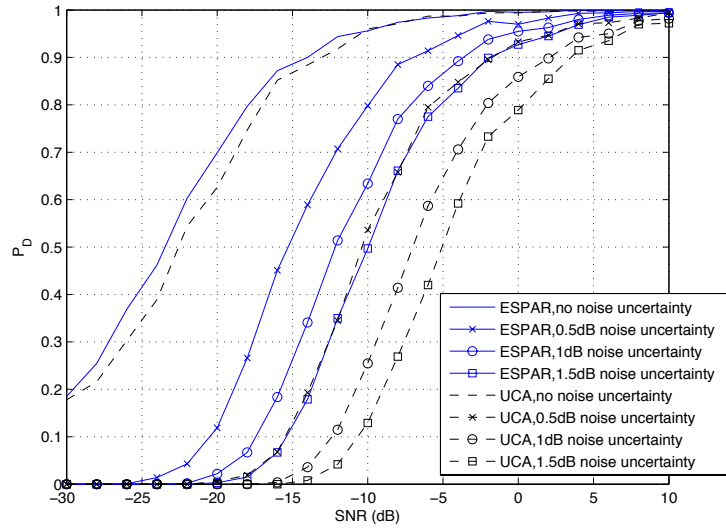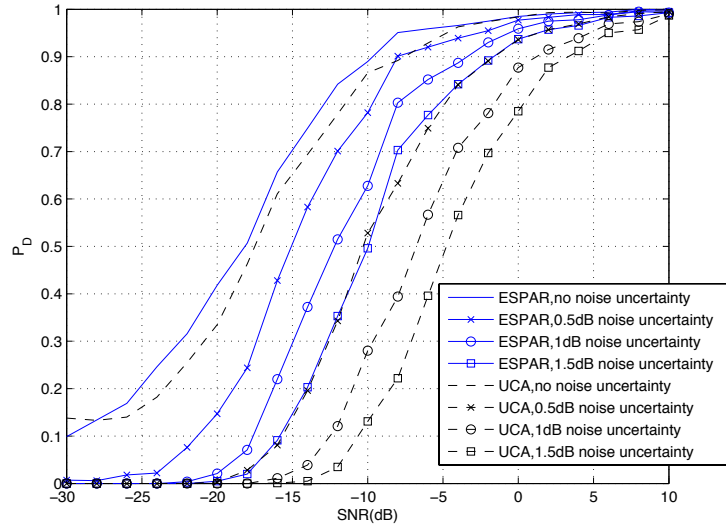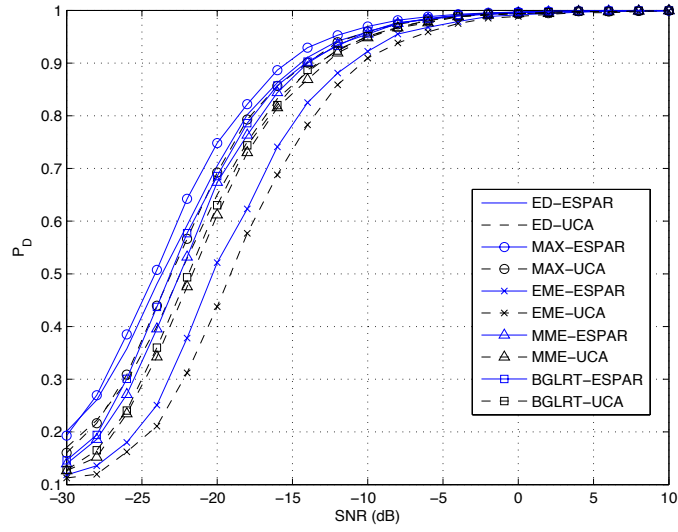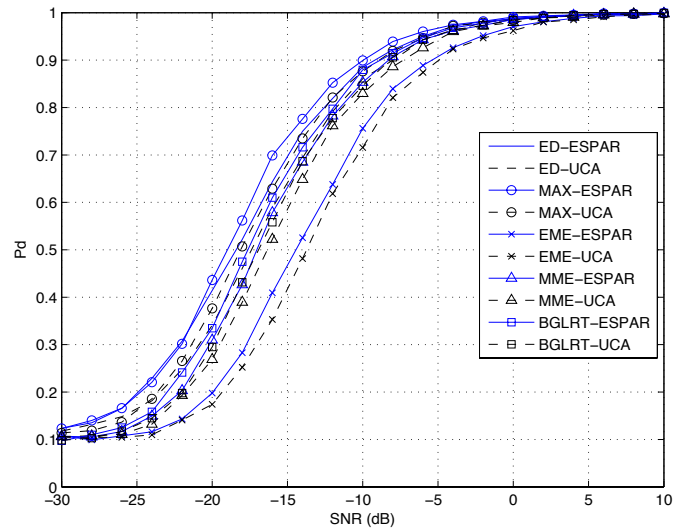
(a) $N_s = 1000$ samples

(b) $N_s = 200$ samples

FIGURE 5.2: Probability of detection using the energy detector, $P_F = 0.1$ (scenario 1).

that with 1 PU present. Specifically, the ESPAR antenna outperforms the UCA, and the reduction of the sampling numbers decreases the probability of detection.

(a) $N_s = 1000$ samples

(b) $N_s = 200$ samples

FIGURE 5.3: Probability of detection using the eigenvalue-based detectors, $P_F = 0.1$ (scenario 1).
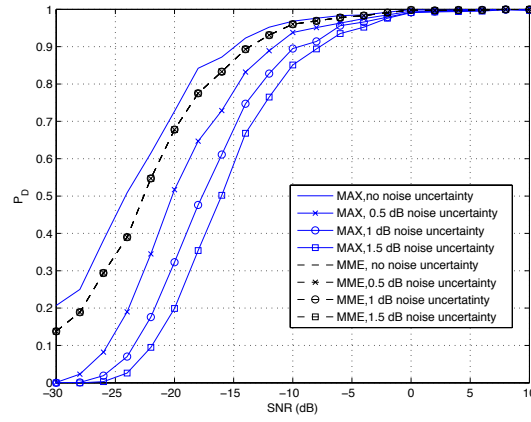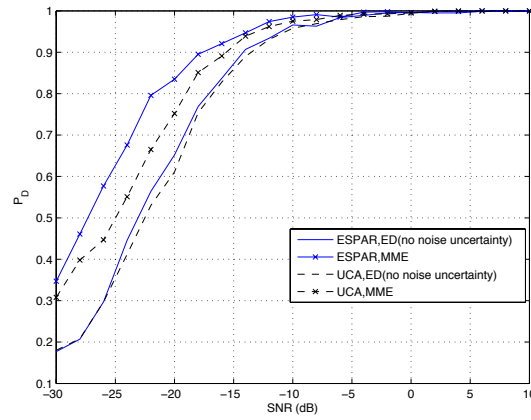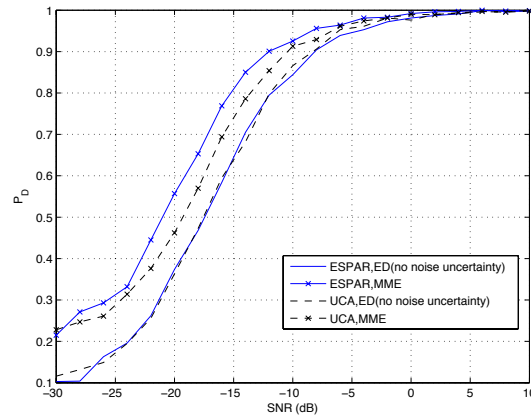
FIGURE 5.4: Probability of detection using MAX and MME detectors with noise uncertainty (scenario 1), $N_s = 1000$ and $P_F = 0.1$

.

(a) $N_s = 1000$ samples

(b) $N_s = 200$ samples

FIGURE 5.5: Probability of detection using the energy detector and MME detector (scenario 2), $P_F = 0.1$.

145

5.4.2 Performance of AoA Estimation

In this section we examine the AoA estimation of the ESPAR antenna using the proposed CS-based method compared to that using the RD-MUSIC algorithm. We also compare the performance of the ESPAR antenna to that of the UCA. For the CS-based method, the overcomplete dictionary $\tilde{A}$ is constructed using the angle grid with 1° sampling $N_\theta = 360$. The reasons for using 360 samples in the overcomplete dictionary are: first, in the simulations, the ESPAR antenna with 6 parasitic elements (thus 6 beampatterns) is considered, and the number of source signals can be recovered is up to 5 (5 is much smaller than 360), thus using 360 samples in the overcomplete dictionary is enough to represent a sparse signal in the AoA estimation problem; secondly, increasing the number of samples leads to the increase in computational complexity significantly, which may impose difficulty especially for applications of the small-size low-power terminals; last but not the least, the adaptive grid refining method can be employed to achieve better precision.

We first examine the performance of the ESPAR antenna under scenario 1, where there is one primary signal coming from the AoA of 20°. Figure 5.6 shows the simulated results using $N_s = 1000$ samples, with varying SNR values. We can see that both the RD-MUSIC and the CS method based on both the ESPAR antenna and UCA are able to detect the direction of the source, even the SNR value is dropped to -10 dB. In particular, we can observe the spectrum peak (maximum energy response) occurs 20°, which is the direction of the signal source.

Then, we reduce the sampling number to $N_s = 200$, and present the results in Figure 5.7. We can make the observations as follows. First, for the UCA, the CS method outperforms the MUSIC algorithm, when SNR drops -10 dB, where there is a big deviation from the true direction. Second, for teh ESPAR antenna, in this scenario the difference between the CS method and MUSIC algorithm is not significant. Finally, the ESPAR antenna performs better than the UCA when SNR=-10 dB, due to the use of directional beampatterns.
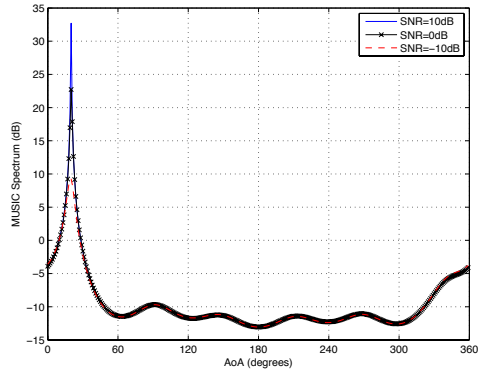
(a) MUSIC based on an ESPAR
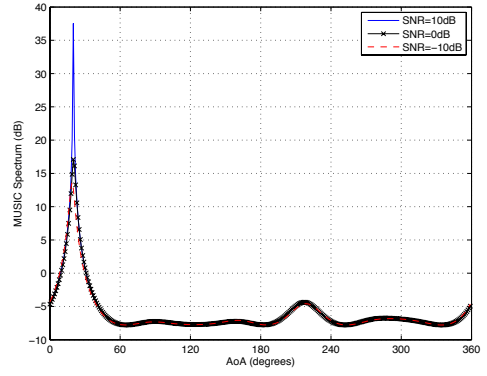
(b) MUSIC based on a UCA
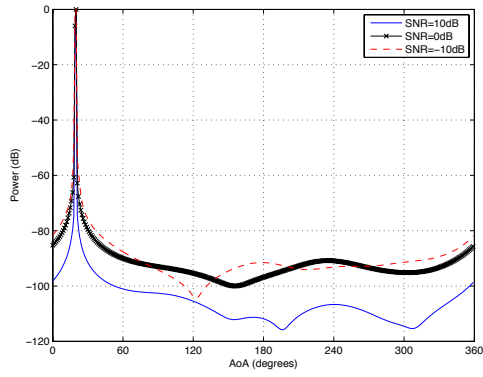
(c) CS based on an ESPAR
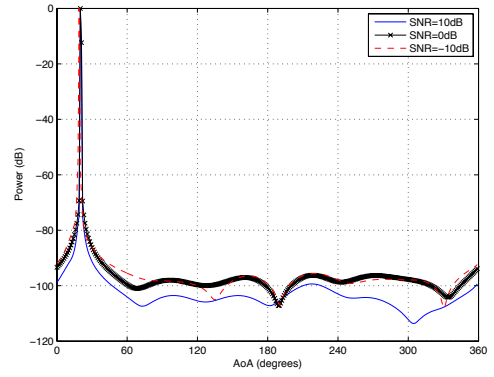
(d) CS based on a UCA

FIGURE 5.6: AoA estimation performance with 1 PU from $20°$, $N_s = 1000$.

(a) MUSIC based on an ESPAR

(b) MUSIC based on a UCA

(c) CS based on an ESPAR

(d) CS based on a UCA
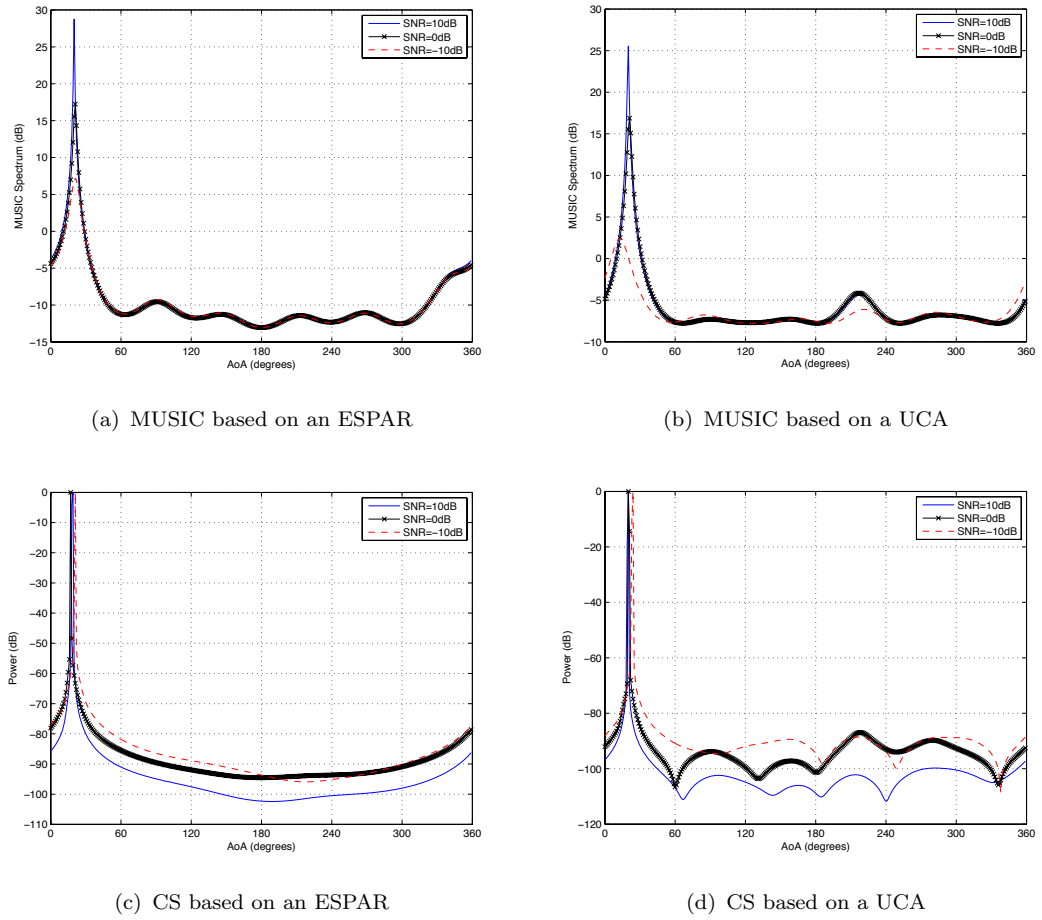
FIGURE 5.7: AoA estimation performance with 1 PU from $20°$, $N_s = 200$.

Now, we will examine the AoA estimation performance in the presence of two source signals from 20° and 50° respectively, i.e., scenario 2. Since we are more concerned about the estimation performance of these algorithms with a smaller number of samples, in the following simulations, we set $N_s = 200$. From Figure 5.8, we can make the following observations. First, for the MUSIC algorithm, when SNR=10 dB, both the ESPAR antenna and UCA can recover the source signals: that is two peaks in the plots occurs 20° and 50° respectively, which are true AoAs of the sources. Second, the increase in the number of sources degrades the performance of the MUSIC algorithms with both the ESPAR antenna and the UCA. When SNR= 0 dB, the EPSAR antenna cannot resolve the sources using the RD-MUSIC algorithms. On the contrary, in this context, the CS method outperforms the MUSIC algorithm.
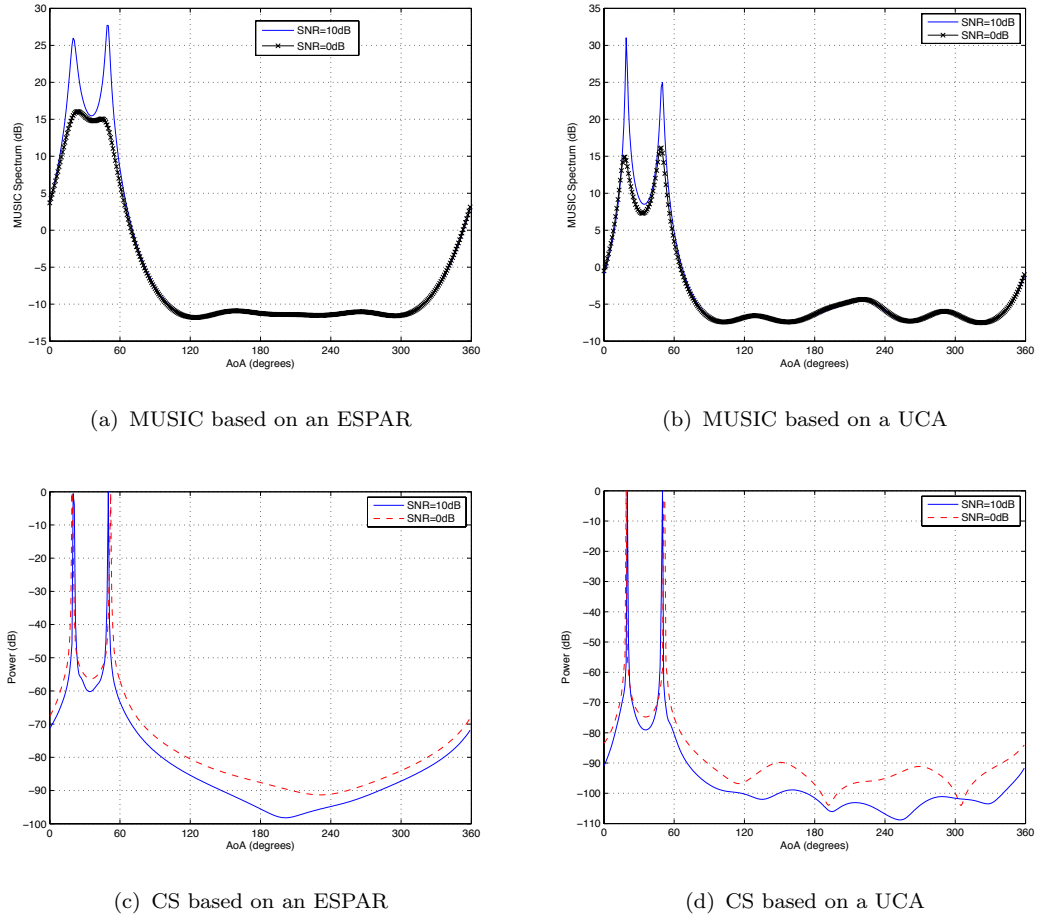

(a) MUSIC based on an ESPAR

(b) MUSIC based on a UCA

(c) CS based on an ESPAR

(d) CS based on a UCA

FIGURE 5.8: AoA estimation performance with 2 PUs from 20° and 50°, $N_s = 200$.
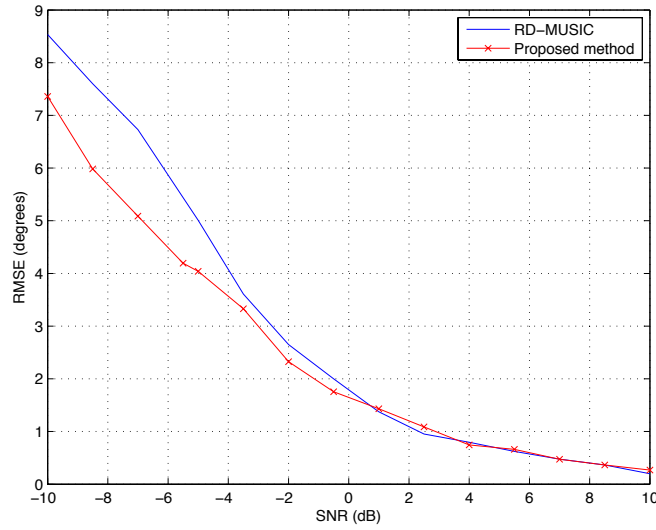
FIGURE 5.9: RMSE of DoA estimation versus SNRs.

To further check the performance of the ESPAR antenna using different algorithms, in Figure 5.9, we show the comparison of the root mean square error (RMSE) of DoA estimation versus input SNR, computed through 200 Monte Carlo trials. Note that we have used the adaptive grid refinement approach proposed in [11] to improve the accuracy: 1° uniform sampling is used for the rough grid and then 0.2° uniform sampling is used for the refined grid. It is shown that the CS method performs better in the low SNR region.

The CS-based AoA estimation method is well known for its capability of distinguishing two closely spaced sources. Thus, we would like to check the AoA estimation performance of an ESPAR antenna when 2 source signals are closer. Figure 5.10 shows the results when 2 sources are from 200° and 215°, respectively, where SNR=10 dB and $N_s = 200$. It is seen that, when the separation between two incoming signals reduces to 15°, only the CS-based method is able to distinguish two signals.

Next, we consider the performance of the ESPAR antenna when the two existing sources are correlated, which may be resulted from the multipath effects in practice. Again, assume that the two source signals are from the 20° and 50°, respectively, and are strongly correlated with a coefficient of 0.95. The simulated
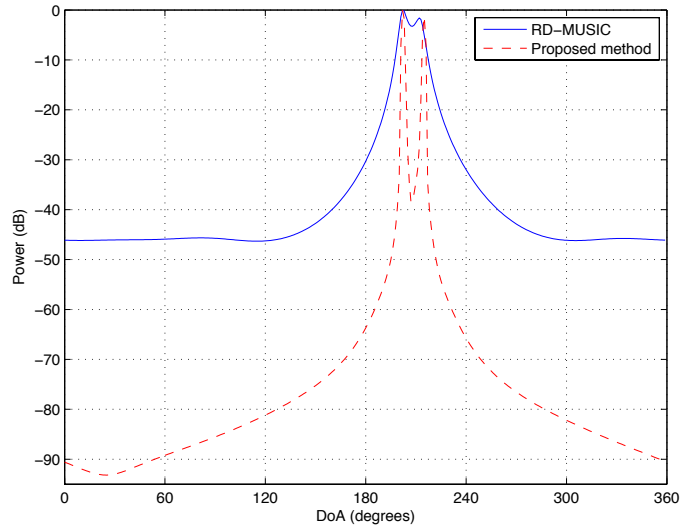
FIGURE 5.10: Simulated results with 2 PUs from 200° and 215°, SNR=10dB, $N_s = 200$.
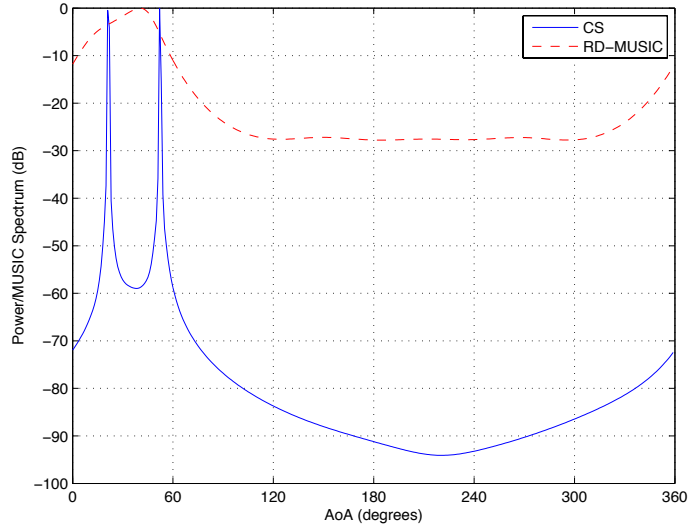
FIGURE 5.11: AoA estimation performance with an ESPAR antenna for two correlated source signals from 20° and 50°,SNR=15 dB, $N_s = 200$.

results are depicted in Figure 5.11, where SNR=15 dB and $N_s = 200$. From Figure 5.8, we know that the RD-MUSIC would be able to resolve two uncorrelated source when SNR is larger than 10 dB. However, it is observed from Figure 5.11 the correlation of the sources degrades the performance of the RD-MUSIC; on the contrary, the CS-based method is able to recover two correlated sources.

5.5 Summary

In the context of CR, a two-stage *spatial spectrum sensing* method is proposed with the use of an ESPAR antenna for compact CR terminal applications. The two-stage sensing method is used to identify the white spectrum space with the dimensions of frequency, time, geographic space and angle. Therefore, not only the *temporal spectrum sensing* methods but also the high-resolution AoA estimation methods have been studied for the ESPAR array.

- In the two-stage method, *temporal spectrum sensing* methods, including the energy detector and eigenvalue-based techniques, are exploited at the first stage to detect occupancy of a frequency subband at a particular time in a given region. If the decision is made that the PU is absent, the sensing process finishes; otherwise, at the second stage the high-resolution AoA estimation is performed by the ESPAR receiver to detect the directions of the existing PU.

- The energy detector and the eigenvalue-base detectors have been studied for the ESPAR antenna for the two-stage method applications. We compared the sensing performance of the ESPAR antenna to that of the ULA. The results demonstrated that the ESPAR antenna outperforms the ULA, since the use of directional beampatterns enhances receive SNR.

- The CS-based AoA estimation method is proposed for the ESPAR antenna and it is compared to the RD-MUSIC algorithm. In order to achieve a sparse representation problem based on the ESPAR antenna, we first use an over-complete dictionary composed of samples from the array manifold. We then introduce a matrix for projecting the sparse signal field into measurements of sector beampatterns, where the sector beampatterns are designed to enable the receive ESPAR scan through its angle space and also increase the receive SNR. The spare spectrum is recovered by using the l_1-SVD method. It is demonstrated that the CS-based method provides a high resolution, as does the RD-MUSIC, with one existing source signal, even with a small number

of samples and low SNR. However, it outperforms the RD-MUSIC with two closely spaced PUs and two correlated primary siganls.

Chapter 6

Conclusions and Further Work

In this thesis, the single-RF ESPAR antenna has been studied for compact wireless terminal applications, combining the emerging techniques ranging from blind interference alignment, small cell networks, and spectrum sensing for cognitive radio to compressive sensing. The ESPAR antenna system is exploited as the alternative to the smart multi-antenna systems which impose challenges in compact terminal applications. The contributions of this work are summarized as follows:

- *Chapter 2:* In this chapter, adaptive beamforming methods are proposed for single-RF reactance-assisted parasitic antenna systems. First, in the single-active antenna array, the signal processing is operated in the reactance-domain, instead of the element-domain as in a multi-active antenna array. In particular, a number of different sets of reactance values (thus a number of different beampatterns) are used on a time division basis to measure signals. In order to achieve signal correlation in the reactance domain, the repeating transmission strategy is employed. However, this method leads to low transmission rate. Based on RD signal processing, MVDR algorithms are developed for the ESPAR array. Due to the lack of a closed-form solution for reactance loads, the beamforming algorithm is developed as an iterative method based on a convex problem and a projector of reactance loads. This algorithm is verified as a fast and efficient adaptive beampattern design

method. Moreover, the genetic algorithm is also studied as a beamforming method for the ESPAR antenna, exploiting a reference signal or knowledge of the desired beampattern. Although the genetic algorithm-based method is a slow convergence method, it might be useful in some applications, since it has the advantage of avoiding becoming trapped in local minima/maxima.

- *Chapter 3:* Chapter 3 studied the ESPAR antenna as a beam switching solution to practically implement blind interference alignment (BIA). The key to BIA is the beam switching at the receiving end, to create heterogeneous block channels seen by different users. In this context, our work is devoted to designing a required number of beampatterns suited to BIA applications. To mimic generic channel vectors seen by a user though beam switching, the random beamforming method (randomly choosing reactance loads from a feasible range) is considered. Sum-rate gains have been found by random beamforming. However, the intrinsic problem of BIA – noise amplification – prohibits applications of BIA in a realistic system such as a cellular system. In this context, we also consider that the beampattern design of the ESPAR antenna can help to improve performance of BIA by enhancing receive SNR. To this end, the sector beampattern selection method and SVD-based beamforming are proposed. Both proper directional beampattern selection and the adaptive beampattern design based on CSIR have been proved to provide sum-rate gains even in the low SNR region, which means that the noise amplification level has been reduced. The ESPAR-based BIA schemes have been compared to the CSIT-based LZFBF technique. It is demonstrated that when the CSI overheads are considered, ESPAR-based BIA provides performance gains comparable with those of the LZFBF.

- *Chapter 4:* In this chapter, the ESPAR antenna has been employed for interference mitigation in femtocells, where the adaptive beamforming of the ESPA antenna as well as the ESPAR-based BIA studied in the previous chapters are used here. In small cell networks, a single omni-directional antenna is generally deployed at both the small BS and the user terminal,

due to size limitation. The use of directional antennas for interference mitigation in the small cell networks is a simple and low-complexity solution. The directional antenna system with a single RF is quite suited to applications of small cell networks. Here consider two scenarios. The first considers that one user is scheduled in each femtocell, i.e., ones that are affected by inter-cell interference. For this scenario, the ESPAR antenna is adopted at both the femto-BSs and UTs. Thus, the ESPAR antenna can operate as a switched-beam to dynamically select a proper sector beampattern to enhance users' SINRs, or operate as an adaptive antenna to design beampattern steering to the desired direction, placing nulls to interferers using knowledge of directions. The feasibility of these processes has been shown in the simulations. In scenario 2, two users are scheduled in each femtocell, and thus they are affected by both intra-cell and inter-cell interference. To address both intra-cell and inter-cell interference, we assume that the ESPAR antenna is adopted at the UTs, while each femto-BS is equipped with a 2-element ULA. Then, the ESPAR-based BIA scheme studied in Chapter 3 is considered for interference mitigation here. The synchronized BIA and virtual BIA schemes are evaluated in this multiple small cell setting. It is shown that the synchronized BIA is more suited for cell-center users; in contrast, virtual BIA works better for cell-edge users.

- *Chapter 5:* This chapter studied the ESPAR antenna as a CR receiver for *spatial spectrum sensing.* A two-stage sensing method is proposed to identify the white spectrum space with the dimensions of frequency, time, geographic space and angle. At the first stage the *temporal spectrum sensing* methods including the energy detector and the eigenvalue-based detectors for the ESPAR antenna to detect occupancy of a frequency subband at a particular time in a given region. The sensing performance of the ESPAR antenna is shown to be better than that of the ULA, due to the use of directional beampatterns. At the presence of the PU, the ESPAR receiver performs AoA estimation of the primary signals. A CS-based AoA estimation method is proposed for the ESPAR antenna. The compassion with the RD-MUSIC

demonstrates that the CS-based method provides higher resolution without a large number of samples, with lower sensitivity to SNR and to correlation of the source signals.

6.1   Further Work

In this thesis, the analysis of the ESPAR antenna focuses on the 2-dimensional channel model, i.e., we assume that the incident signal is from the the same plane as the antenna array. Thus, the array response to the signal is represented as the azimuth plane. In practice, this assumption cannot hold. In order to provide a more accurate examination of the performance of the ESPAR in a realistic communication system (e.g., SCNs), a 3-dimensional channel model should be studied, which takes into account the array responses in both the azimuth plane and the elevation plane. The study of the 3-dimensional channel mode, in turn, is able to help the design of the ESPAR antenna, especially in terms of antenna efficiency, which has not been discussed in this thesis.

A first attempt to apply CS theory to the parasitic antenna is presented in this work for the AoA estimation problem. However, the design of the projection matrix (as well as the overcomplete dictionary/orthogonal basis) is mainly based on the properties of the antenna array. Indeed, the performance of sparse spectrum recovery is related to both the projection matrix and the overcomplete dictionary. That is defined by some conditions, such as the restricted isometry property (RIP) and mutual coherence. In order to improve the compressive sensing based on an ESPAR antenna, an optimization method for the projection matrix or a learning method for the dictionary would help.

Appendix A

Analytical Formulas for Impedance Matrix

In this work, we consider that the parasitic array is comprised of $M+1$ electrical thin dipoles with finite length $l = \lambda/2$: distance between dipoles is denoted by r. The array can be modelled by an impedance matrix $\mathbf{Z}$, in which the entry $Z_{i,i}$ is the self-impedances and $Z_{i,j}, i \neq j$ is mutual impedance between the i-th and j-th element, where $i, j = \{1, \cdots, M+1\}$. Since identical dipoles are used in an array with symmetrical geometry, we have $Z_{0,0} = Z_{1,1} = \cdots = Z_{M+1,M+1}$ and $Z_{i,j} = Z_{j,i}$.

An approached expression of the self-impedance $(Z_{i,i})$ of a dipole is calculated by the impedance of an n half-wavelength long isolated dipole denote by $Z_{i,i} = R_{i,i} + jX_{i,i}$, where the input impedance resistance $R_{i,i}$ is calculate by [129]

$$R_{i,i} = \frac{\eta_f}{2\pi} \left\{ \gamma + ln(\pi n) - C_i(\pi n) + \frac{1}{2}cos(\pi n) \left[\gamma + ln\left(\frac{\pi}{n}\right) + C_i(2\pi n) - 2C_i(\pi n) \right] \right\}, \tag{A.1}$$

and the reactance $X_{i,i}$ is calculated by [129]

$$X_{i,i} = \frac{\eta}{4\pi} \left\{ 2S_i(\pi n) + cos(\pi n) \left[2S_i(\pi n) - S_i(2\pi n) \right] \right\}, \tag{A.2}$$

where $\gamma \approx 0.5772$ is the Euler's constant, $\eta_f = 120\pi$ is the free-space impedance, and $S_i(x)$ and $C_i(x)$ are the sine and cosine integral functions, respectively expressed as

$$S_i(x) = \int_0^x \frac{sin(t)}{t} dt, \tag{A.3}$$

$$C_i(x) = \int_\infty^x \frac{cos(t)}{t} dt. \tag{A.4}$$

The coupling impedances $Z_{i,j} = R_{i,j} + jX_{i,j}, i \neq j$ are calculated using the induced electromotive force method (EFM) [41]

$$R_{i,j} = \frac{\eta_f}{4\pi}[2C_i(\upsilon_0) - C_i(\upsilon_1) - C_i(\upsilon_2)], \tag{A.5a}$$

$$X_{i,j} = -\frac{\eta_f}{4\pi}[2S_i(\upsilon_0) - S_i(\upsilon_1) - S_i(\upsilon_2)], \tag{A.5b}$$

where parameters υ_0, υ_1 and υ_2 are determined by the array configuration: i.e.,

$$\upsilon_0 = kd, \tag{A.6a}$$

$$\upsilon_1 = k(\sqrt{d^2 + l^2} + l), \tag{A.6b}$$

$$\upsilon_2 = k(\sqrt{d^2 + l^2} - l). \tag{A.6c}$$

Appendix B

SOC Programming for l_1-SVD Relaxation

The general second-order cone (SOC) program is defined as [130]

$$\min_{\boldsymbol{x}} \quad \boldsymbol{f}^T \boldsymbol{x} \tag{B.1a}$$

$$s.t. \quad \|\boldsymbol{A}_i \boldsymbol{x} + \boldsymbol{b}_i\| \leq \boldsymbol{c}_i^T \boldsymbol{x} + d_i, \quad i = 1, \cdots, N, \tag{B.1b}$$

where $\boldsymbol{x} \in \mathbb{R}^{n \times 1}$ is the variable being optimized, and the problem parameters are denoted by $\boldsymbol{f} \in \mathbb{R}^{n \times 1}$, $\boldsymbol{A}_i \in \mathbb{R}^{(m_i-1) \times n}$, $\boldsymbol{b}_i \in \mathbb{R}^{(m_i-1) \times 1}$, $\boldsymbol{c}_i \in \mathbb{R}^{n \times 1}$ and $d_i \in \mathbb{R}$. The constraint (B1.b) is called a second-order cone constraint of dimension m_i. The standard or unit second-order cone of dimension m_i is defined as [56]

$$\mathcal{K}_{m_i} = \left\{ \begin{bmatrix} \boldsymbol{u} \\ t \end{bmatrix} \middle| \boldsymbol{u} \in \mathbb{R}^{(m_i-1) \times 1}, t \in \mathbb{R}, \|\boldsymbol{u}\| \leq t \right\}. \tag{B.2}$$

For $m_i = 1$, the unit second-order cone reduces to

$$\mathcal{K}_1 = \{t | t \in \mathbb{R}, 0 \leq t\}. \tag{B.3}$$

We need to rewrite the unconditional optimization problem (5.30) as the form of SOC program defined above, i.e., the objective function should be linear while the

constraints can be second-order cone form or linear inequality. First, we introduce two non-negative variables μ_1 and μ_2, and thus (5.3) is rewritten as a conditional optimization problem as follows

$$\min_{\mu_1,\mu_2,\tilde{\boldsymbol{S}}_{svd}} \quad \mu_1 + \eta\mu_2, \tag{B.4a}$$

$$s.t. \quad \|\boldsymbol{Y}_{svd} - \boldsymbol{W}\tilde{\boldsymbol{A}}\tilde{\boldsymbol{S}}_{svd}\|_F \leq \mu_1, \tag{B.4b}$$

$$\|\tilde{\boldsymbol{s}}^{l_2}\|_1 \leq \mu_2, \tag{B.4c}$$

where η is a constant controls the trade-off between the residual norm and the sparsity of the spectrum.

Recall that the elements of the vector $\tilde{\boldsymbol{s}}^{l_2}$ are computed from the l_2-norm of rows of $\tilde{\boldsymbol{S}}_{svd}$. They are guaranteed to be non-negative real values. Therefore, the constraint (B.4c) reduces to a linear inequality constraint taking the following form:

$$\|\tilde{\boldsymbol{s}}^{l_2}\|_1 = \sum_{i=1}^{N_\theta} \tilde{s}_i^{l_2} \leq \mu_2. \tag{B.5}$$

Then let $\tilde{\boldsymbol{Z}} = \boldsymbol{Y}_{svd} - \boldsymbol{W}\tilde{\boldsymbol{A}}\tilde{\boldsymbol{S}}_{svd}$, and define its vectorization form as $\tilde{\boldsymbol{z}} = vec(\tilde{\boldsymbol{Z}})$. Thus, the constraint (B.4b) is able to reformulated as a SOC constraint, as follows

$$\|\boldsymbol{Y}_{svd} - \boldsymbol{W}\tilde{\boldsymbol{A}}\tilde{\boldsymbol{S}}_{svd}\|_F = \|\tilde{\boldsymbol{z}}\| \leq \mu_1. \tag{B.6}$$

Finally, the full SOC programming for the l_1-SVD relaxation (5.30) is given by

$$\min_{\mu_1,\mu_2,\tilde{\boldsymbol{S}}^{l_2}} \quad \mu_1 + \eta\mu_2, \tag{B.7a}$$

$$s.t. \quad \|\tilde{\boldsymbol{z}}\| \leq \mu_1, \tag{B.7b}$$

$$\tilde{\boldsymbol{z}} = vec(\boldsymbol{Y}_{svd} - \boldsymbol{W}\tilde{\boldsymbol{A}}\tilde{\boldsymbol{S}}_{svd}), \tag{B.7c}$$

$$\sum_{i=1}^{N_\theta} \tilde{s}_i^{l_2} \leq \mu_2. \tag{B.7d}$$

Bibliography

[1] T. Tanaka, I. Chiba, R. Miura, and Y. Karasawa. Digital signal processor for digital multi-beam forming antenna in mobile communication. In *Proc. IEEE VTC*, pages 1507–1511, 1994.

[2] S. A. Ramprashad and G. Caire. Cellular vs. network MIMO: A comparison including the channel state information overhead. In *IEEE PIMRC*, pages 878–884, 2009.

[3] C. Wang, H. C. Papadopoulos, S. A. Ramprashad, and G. Caire. Improved blind interference alignment in a cellular environment using power allocation and cell-based clusters. In *IEEE Int. Conf. Commun. (ICC)*, pages 1–6, 2011.

[4] Y. Zeng and Y. Liang. Eigenvalue-based spectrum sensing algorithms for cognitive radio. *IEEE Trans. Commun.*, 57(6):1784–1793, June 2009.

[5] A. Kortun, T. Ratnarajah, M. Sellathurai, Y. Liang, and Y. Zeng. On the eigenvalue based spectrum sensing and secondary user throughput. *IEEE Trans. Veh. Technol.*, 64(3):1480–1486, March 2014.

[6] Lal Chand L. C. Godara. Application of antenna arrays to mobile communications. II. Beam-forming and direction-of-arrival considerations. *Proc. IEEE*, 85(8):1195–1245, August 1997.

[7] D. E. Dudgeon and D. H. Johnson. *Array Signal Processing: Concepts and Techniques.* Prentice Hall, 1993.

[8] J. Capon. High-resolution frequency-wavenumber spectrum analysis. *Proc. IEEE*, 57(8):1408–1418, June 1969.

[9] R. O. Schmidt. Multiple emitter location and signal parameter estimation. *IEEE Trans. Antennas Propag.*, 34(3):276–280, March 1986.

[10] R. Roy and T. Kailath. ESPRIT – Estimation of signal parameters via rotational invariance techniques. *IEEE Trans. Acoust., Speech, Signal Process.*, 37(7):984–995, July 1989.

[11] D. Malioutov, M. Cetin, and A. S. Willsky. A sparse signal reconstruction perspective for source localization with sensor arrays. *IEEE Trans. Signal Process.*, 53(8):3010–3022, August 2005.

[12] G. Foschini and M. Gans. On limits of wireless communications in a fading environment when using multiple antennas. *Wireless personal communications*, 6(3):311–335, 1998.

[13] E. Telatar. Capacity of multi-antenna gaussian channels. *European transactions on telecommunications*, 10(6):585–595, 1999.

[14] M. Sellathurai and S. Haykin. *Space-time layered information processing for wireless communications*, volume 30. John Wiley & Sons, 2009.

[15] L. Zheng and D. Tse. Diversity and multiplexing: A fundamental tradeoff in multiple-antenna channels. *IEEE Trans. Inf. Theory*, 49(5):1073–1096, May 2003.

[16] S. Cui, A. Goldsmith, and A. Bahai. Energy-efficiency of MIMO and cooperative MIMO techniques in sensor networks. *IEEE J. Sel. Areas Commun.*, 22(6):1089–1098, August 2004.

[17] O. Alrabadi. *MIMO communication using single feed antenna arrays*. PhD thesis, Aalborg University, 2011.

[18] A. Tulino, A. Lozano, and S. Verdú. Impact of antenna correlation on the capacity of multiantenna channels. *IEEE Trans. Inf. Theory*, 51(7):2491–2509, July 2005.

[19] D. Shiu, G. Foschini, M. Gans, and J. Kahn. Fading correlation and its effect on the capacity of multielement antenna systems. *IEEE Trans. Commun.*, 48(3):502–513, March 2000.

[20] H. Yagi. Beam transmission of ultra short waves. *IEEE Proc. the Institute of Radio Engineers, Proceedings*, 16(6):715–740, August 1928.

[21] D. V. Thiel and S. Smith. *Switched parasitic antennas for cellular communications.* Artech House, 2001.

[22] R. J. Dinger. Reactively steered adaptive array using microstrip patch elements at 4 GHz. *IEEE Trans. Antennas Propag.*, 32(8):848–856, January 1984.

[23] K. Gyoda and T. Ohira. Design of electronically steerable passive array radiator (ESPAR) antennas. In *Porc. IEEE International Symposium Antennas and Propagation Society*, volume 2, pages 922–925, 2000.

[24] T. Ohira and K. Gyoda. Electronically steerable passive array radiator antennas for low-cost analog adaptive beamforming. In *Proc. IEEE International Conference on Phased Array Systems and Technology*, pages 101–104, 2000.

[25] M. Taromaru and T. Ohira. Electronically steerable parasitic array radiator antenna– Principle, control theory and its applications. *Proc. Int. Union of Radio Science General Assembly*, 2005.

[26] G. Caire, N. Jindal, M. Kobayashi, and N. Ravindran. Multiuser MIMO achievable rates with downlink training and channel state feedback. *IEEE Trans. Inf. Theory*, 56(6):2845–2866, June 2010.

[27] T. Gou, C. Wang, and S. A. Jafar. Aiming perfectly in the dark-Blind interference alignment through staggered antenna switching. *IEEE Trans. Signal Process.*, 59(6):2734–2744, March 2011.

[28] H. Claussen, L. Ho, and L. Samuel. An overview of the femtocell concept. *Bell Labs Technical Journal*, 13(1):221–245, 2008.

[29] L. Venturino, N. Prasad, and X. Wang. Coordinated scheduling and power allocation in downlink multicell OFDMA networks. *IEEE Trans. Veh. Technol.*, 58(6):2835–2848, July 2009.

[30] V. Chandrasekhar, J. G. Andrews, T. Muharemovict, Z. Shen, and A. Gatherer. Power control in two-tier femtocell networks. *IEEE Trans. Wireless Commun.*, 8(8):4316–4328, August 2009.

[31] H. Lee, D. Oh, and Y. Lee. Mitigation of inter-femtocell interference with adaptive fractional frequency reuse. In *Proc. IEEE ICC*, pages 1–5, 2010.

[32] S. Ali and V. Leung. Dynamic frequency allocation in fractional frequency reused OFDMA networks. *IEEE Trans. Wireless Commun.*, 8(8):4286–4295, August 2009.

[33] Simon S. Haykin. Cognitive radio: Brain-empowered wireless communications. *IEEE J. Sel. Areas Commun.*, 23(2):201–220, Feburary 2005.

[34] A. Goldsmith, S. A. Jafar, I. Maric, and S. Srinivasa. Breaking spectrum gridlock with cognitive radios: An information theoretic perspective. *Proc. IEEE*, 97(5):894–914, May 2009.

[35] T. Yücek and H. Arslan. A survey of spectrum sensing algorithms for cognitive radio applications. *IEEE Commun. Surveys & Tutorials*, 11(1):116–130, First Quarter 2009.

[36] E. Tsakalaki. *Reduced-complexity wireless transceiver architectures and techniques for space-time communications*. PhD thesis, Aalborg University, 2012.

[37] A. Kalis, A. G. Kanatas, and C. B. Papadias. *Parasitic Antenna Arrays for Wireless MIMO Systems*. Springer, 2014.

[38] R. Dinger. Adaptive microstrip antenna array using reactively terminated parasitic elements. In *Proc. IEEE International Symposium of Antennas and Propagation Society*, volume 20, pages 300–303, 1982.

[39] T. Ohira. Adaptive array antenna beamforming architectures as viewed by a microwave circuit designer. In *Proc. IEEE Asia-Pacific Microwave Conference*, pages 828–833, 2000.

[40] C. Sun, A. Hirata, T. Ohira, and N. C. Karmakar. Fast beamforming of electronically steerable parasitic array radiator antennas: theory and experiment. *IEEE Trans. Antennas and Propag.*, 52(7):1819–1832, July 2004.

[41] L. Petit, L. Dussopt, and J. M. Laheurte. MEMS-switched parasitic-antenna array for radiation pattern diversity. *IEEE Trans. Antennas and Propag.*, 54(9):2624–2631, September 2006.

[42] C. A. Balanis. *Antenna theory: Analysis and design.* John Wiley & Sons, 2012.

[43] C. Plapous, J. Cheng, E. Taillefer, A. Hirata, and T. Ohira. Reactance domain MUSIC algorithm for electronically steerable parasitic array radiator. *IEEE Trans. Antennas and Propag.*, 52(12):3257–3264, December 2004.

[44] E. P. Tsakalaki, D. Wilcox, E. De Carvalho, C. B. Papadias, and T. Ratnarajah. Spectrum sensing using single-radio switched-beam antenna systems. In *Proc. IEEE CROWNCOM*, pages 118–123, 2012.

[45] D. Wilcox, E. Tsakalaki, A. Kortun, T. Ratnarajah, C. B. Papadias, and M. Sellathurai. On spatial domain cognitive radio using single-radio parasitic antenna arrays. *IEEE J. Sel. Areas Commun.*, 31(3):571–580, March 2013.

[46] W. F. Gabriel. Adaptive arrays – An introduction. *Proc. IEEE*, 64(2): 239–272, February 1976.

[47] O. N. Alrabadi, B. C. Papadias, A. Kalis, and R. Prasad. A universal encoding scheme for MIMO transmission using a single active element for PSK modulation schemes. *IEEE Trans. Wireless Commun.*, 8(10):5133–5142, Octorber 2009.

[48] V. I. Barousis, A. G. Kanatas, and A. Kalis. Beamspace-domain analysis of single-RF front-end MIMO systems. *IEEE Trans. Veh. Technol.*, 60(3): 1195–1199, March 2011.

[49] J. Cheng, Y. Kamiya, and T. Ohira. Adaptive beamforming of ESPAR antenna using sequential perturbation. In *IEEE MTT-S International Digest Microwave Symposium*, volume 1, pages 133–136, 2001.

[50] V. Barousis, A. G. Kanatas, A. Kalis, and C. Papadias. A stochastic beamforming algorithm for ESPAR antennas. *IEEE Antennas Wireless Propag. Lett.*, 7:745–748, August 2008.

[51] E. D. Thomatos, P. N. Vasileiou, and A. G. Kanatas. ESPAR loads calculation for achieving desired radiated patterns with a genetic algorithm. In *Proc. IEEE European Conference on Antennas and Propagation (EuCAP)*, pages 902–905, 2013.

[52] Q. Han, V. Briend, and T. Ohira. Evaluation of the adaptive beamforming capability of an ESPAR antenna using the genetic algorithm. In *Proc. IEEE European Conference on Wireless Technology*, pages 59–62, 2006.

[53] E. Taillefer, A. Hirata, and T. Ohira. Reactance-domain esprit algorithm for a hexagonally shaped seven-element ESPAR antenna. *IEEE Trans. Antennas and Propag.*, 53(11):3486–3495, November 2005.

[54] E. Taillefer, W. Nomura, J. Cheng, M. Taromaru, Y. Watanabe, and T. Ohira. Enhanced reactance-domain ESPRIT algorithm employing multiple beams and translational-invariance soft selection for direction-of-arrival estimation in the full azimuth. *IEEE Trans. Antennas Propag.*, 56(8):2514–2526, August 2008.

[55] R. Bains. *On the Usage of Parasitic Antenna Elements in Wireless Communication Systems*. PhD thesis, Norwegian University of Science and Technology, 2008.

[56] S. Boyd and L. Vandenberghe. *Convex optimization.* Cambridge University Press, 2009.

[57] R. Qian, M. Sellathurai, and D. Wilcox. A study on MVDR beamforming applied to an ESPAR antenna. *IEEE Signal Process. Lett.*, 22(1):67–70, January 2015.

[58] L. N Psaromiligkos and S. N. Batalama. Interference-plus-noise covariance matrix estimation for adaptive space-time processing of DS/CDMA signals. In *Proc. IEEE Fall Vehicular Technology Conf.*, volume 5, pages 2197–2204, 2000.

[59] R. L. Haupt. Thinned arrays using genetic algorithms. *IEEE Trans. Antennas Propag.*, 42(7):993–999, July 1994.

[60] R. L. Haupt. An introduction to genetic algorithms for electromagnetics. *IEEE Antennas Propag. Mag.*, 37(2):7–15, April 1995.

[61] R. Schlub, J. Lu, and T. Ohira. Seven-element ground skirt monopole ESPAR antenna design from a genetic algorithm and the finite element method. *IEEE Trans. Antennas Propag.*, 51(11):3033–3039, November 2003.

[62] K. Yan and Y. Lu. Sidelobe reduction in array-pattern synthesis using genetic algorithm. *IEEE Trans. Antennas Propag.*, 45(7):1117–1122, July 1997.

[63] M. Mitchell. *An introduction to genetic algorithms.* MIT Press, 1998.

[64] J. Lofberg. YALMIP: A toolbox for modeling and optimization in MATLAB. In *Proc. CACSD Conference*, pages 284–289, 2004.

[65] Imre Polik. Sedumi 1.1 users guide, 2005. URL http://sedumi.ie.lehigh.edu/.

[66] V. R. Cadambe and S. A. Jafar. Interference alignment and degrees of freedom of the K-user interference channel. *IEEE Trans. Inf. Theory*, 54(8): 3425–3441, July 2008.

[67] S. A. Jafar and M. J. Fakhereddin. Degrees of freedom for the MIMO interference channel. *IEEE Trans. Inf. Theory*, 53(7):2637–2642, July 2007.

[68] M. A. Maddah-Ali, A. S. Motahari, and A. K. Khandani. Communication over MIMO X channels: Interference alignment, decomposition, and performance analysis. *IEEE Trans. Inf. Theory*, 54(8):3457–3470, August 2008.

[69] M. Razaviyayn, M. Sanjabi, and Z. Luo. Linear transceiver design for interference alignment: Complexity and computation. *IEEE Trans. Inf. Theory*, 58(5):2896–2910, May 2012.

[70] Huiqin H. Du, T. Ratnarajah, M. Sellathurai, and C. Papadias. Reweighted nuclear norm approach for interference alignment. *IEEE Trans. Commun.*, 61(9), September 2013.

[71] G. Caire and S. Shamai. On the achievable throughput of a multiantenna Gaussian broadcast channel. *IEEE Trans. Inf. Theory*, 49(7):1691–1706, July 2003.

[72] C. S. Vaze and M. K. Varanasi. The degree-of-freedom regions of MIMO broadcast, interference, and cognitive radio channels with no CSIT. *IEEE Trans. Inf. Theory*, 58(8):5354–5374, May 2012.

[73] Syed A S. A. Jafar. Blind interference alignment. *IEEE J. Sel. Topics Signal Process.*, 6(3):216–227, June 2012.

[74] Joseph C Liberti and Theodore S Rappaport. A geometrically based model for line-of-sight multipath radio channels. In *Poc. IEEE Veh. Technol. Conference*, volume 2, pages 844–848, 1996.

[75] J. Fuhl, A. F. Molisch, and E. Bonek. Unified channel model for mobile radio systems with smart antennas. In *Proc. Ins. Elect. Eng. - Radar Sonar Navigation*, volume 145, pages 32–41. IET, 1998.

[76] C. Wang, H.C. Papadopoulos, S.A. Ramprashad, and G. Caire. Design and operation of blind interference alignment in cellular and cluster-based

systems. In *IEEE Information Theory and Applications Workshop (ITA)*, pages 1–10, 2011.

[77] R. Qian, M. Sellathurai, and D. Wilcox. On the design of blind interference alignment using ESPAR antenna. In *Proc. IEEE International Conference on Communications and Networking in China (CHINACOM)*, pages 866–870, 2012.

[78] R. Qian and M. Sellathurai. Performance of the blind interference alignment using ESPAR antennas. In *Proc. IEEE International Conference on Communications (ICC)*, pages 4885–4889, 2013.

[79] R. Qian and M. Sellathurai. Design of ESPAR based blind interference alignment for cellular systems. In *Proc. IEEE Wireless Communications and Networking Conference (WCNC)*, pages 3083–3087, 2013.

[80] H. Viswanathan, S. Venkatesan, and H. Huang. Downlink capacity evaluation of cellular networks with known-interference cancellation. *IEEE J. Sel. Areas Commun.*, 21(5):802–811, June 2003.

[81] T. Yoo and A. Goldsmith. On the optimality of multiantenna broadcast scheduling using zero-forcing beamforming. *IEEE J. Sel. Areas Commun.*, 24(3):528–541, March 2006.

[82] V. Chandrasekhar, J. Andrews, and A. Gatherer. Femtocell networks: A survey. *IEEE Commun. Mag.*, 46(9):59–67, 2008.

[83] R. Razavi and H. Claussen. Self-configuring switched multi-element antenna system for interference mitigation in femtocell networks. In *Proc. IEEE PIMRC*, pages 237–242, 2011.

[84] A. Tsai, J. Huang, L. Wang, and R. Hwang. High capacity femtocells with directional antennas. In *Proc. IEEE WCNC*, pages 1–6, 2010.

[85] S. Chen, Z. Feng, Q. Zhang, and P. Zhang. Interference mitigation and capacity optimization in cooperative public femtocell networks with cognitive enabled multi-element antennas. In *IEEE Globecom Workshops*, pages 652–656, 2012.

[86] R. Razavi, L. Ho, H. Claussen, and D. López-Pérez. Improving small cell performance through switched multi-element antenna systems in heterogeneous networks. *IEEE Trans. Veh. Technol.*, PP:1–13, August 2014.

[87] J. Hoydis, M. Kobayashi, and M. Debbah. Green small-cell networks. *IEEE Veh. Technol. Mag.*, 6(1):37–43, March 2011.

[88] Furkan Can Kavasoglu, Yichao Huang, and Bhaskar D Rao. Semi-blind interference alignment techniques for small cell networks. *IEEE Trans. Signal Process.*, 62(23):6335–6348, December 2014.

[89] A. Saleh and R. Valenzuela. A statistical model for indoor multipath propagation. *IEEE J. Sel. Areas Commun.*, 5(2):128–137, Feburary 1987.

[90] Q. Spencer, B. Jeffs, M. Jensen, and A. Swindlehurst. Modeling the statistical time and angle of arrival characteristics of an indoor multipath channel. *IEEE J. Sel. Areas Commun.*, 18(3):347–360, March 2000.

[91] Y. Cho, J. Kim, W. Yang, and C. Kang. *MIMO-OFDM wireless communications with MATLAB*. John Wiley & Sons, 2010.

[92] J. Wallace and M. Jensen. Modeling the indoor MIMO wireless channel. *IEEE Trans. Antennas Propag.*, 50(5):591–599, May 2002.

[93] J. B. Andersen and R. Vaughan. Channels, Propagation and Antennas for Mobile Communications. *IEE Electromagnetic Waves Series*, 50, 2003.

[94] C. Sun, T. Hunziker, and M. Taromaru. Employing directional antennas in double-directional radio channel. In *IEEE Int. Symposium on Wireless Communication Systems*, pages 581–585, 2005.

[95] R. Qian and M. Sellathurai. Interference mitigation in femtocell networks using singleradio parasitic antennas. In *IEEE International Conference on Communications (ICC)*, London, June 2015.

[96] E. Taillefer, C. Plapous, J. Cheng, K. Iigusa, and T. Ohira. Reactance-domain MUSIC for ESPAR antennas (experiment). In *Proc. IEEE WCNC*, volume 1, pages 98–102, 2003.

[97] E. J. Candès and M. B. Wakin. An introduction to compressive sampling. *IEEE Signal Process. Mag.*, 25(2):21–30, March 2008.

[98] J. Xie, Z. Fu, and H. Xian. Spectrum sensing based on estimation of direction of arrival. In *IEEE International Conference on Computational Problem-Solving (ICCP)*, pages 39–42, 2010.

[99] R. Qian, M. Sellathurai, and T. Ratnarajah. Directional spectrum sensing for cognitive radio using ESPAR arrays with a single RF chain. In *IEEE Eur. Conf. Networks and Communications (EuCNC)*, pages 1–5, 2014.

[100] F. F. Digham, M Alouini, and M. K. Simon. On the energy detection of unknown signals over fading channels. *IEEE Trans. Commun.*, 55(1):21–24, Janurary 2007.

[101] L. Råde and B. Westergren. Beta β mathematics handbook. *Studentlitteratur Chartwell-Bratt, 2 ed.*, 1990.

[102] J. Lehtomaki, M. Juntti, H. Saarnisaari, and S. Koivu. Threshold setting strategies for a quantized total power radiometer. *IEEE Signal Processing Lett.*, 12(11):796, November 2005.

[103] T. Ratnarajah. Spatially correlated multiple-antenna channel capacity distributions. In *IEE Proc. Communications*, volume 153, pages 263–271, April 2006.

[104] T. Ohira and K. Gyoda. Hand-held microwave direction-of-arrival finder based on varactor-tuned analog aerial beamforming. In *Proc. IEEE Asia-Pacific Microwave Conf. (APMC)*, volume 2, pages 585–588, 2001.

[105] E. Taillefer, A. Hirata, and T. Ohira. Direction-of-arrival estimation using radiation power pattern with an ESPAR antenna. *IEEE Trans. Antennas Propag.*, 53(2):678–684, Feburary 2005.

[106] T. Svantesson and M. Wennstrom. High-resolution direction finding using a switched parasitic antenna. In *Proc. IEEE Signal Processing Workshop on Statistical Signal Processing, pages=508–511, year=2001,*.

[107] S. L. Preston, D. V. Thiel, T. A. Smith, S. G. OḰeefe, and J. Lu. Base-station tracking in mobile communications using a switched parasitic antenna array. *IEEE Trans. Antennas Propag.*, 46(6):841–844, June 1998.

[108] R. Vaughan. Switched parasitic elements for antenna diversity. *IEEE Trans. Antennas Propag.*, 47(2):399–405, Feburary 1999.

[109] I. Gorodnitsky and B. Rao. Sparse signal reconstruction from limited data using FOCUSS: A re-weighted minimum norm algorithm. *IEEE Trans. Signal Process.*, 45(3):600–616, March 1997.

[110] S. Cotter. Multiple snapshot matching pursuit for direction of arrival (DOA) estimation. In *Proc. Eur. Signal Process. Conf.*, pages 247–251, 2007.

[111] D. Donoho. Compressed sensing. *IEEE Trans. Inf. Theory*, 52(4):1289–1306, April 2006.

[112] E. Candès and T. Tao. Decoding by linear programming. *IEEE Trans. Inf. Theory*, 51(12):4203–4215, December 2005.

[113] S. Mallat and Z. Zhang. Matching pursuits with time-frequency dictionaries. *IEEE Trans. Signal Process.*, 41(12):3397–3415, December 1993.

[114] J. lanchard and J. Tanner. Performance comparisons of greedy algorithms in compressed sensing, 2013. URL http://people.maths.ox.ac.uk/tanner/papers/PCGACS.pdf.

[115] S. Chen, D. Donoho, and M. Saunders. Atomic decomposition by basis pursuit. *SIAM J. Sci. Comput.*, 20(1):33–61, 1998.

[116] D. Malioutov. A sparse signal reconstruction perspective for source localization with sensor arrays. Master's thesis, Massachusetts Institute of Technology, 2003.

[117] D. L. Donoho, M. Elad, and V. N. Temlyakov. Stable recovery of sparse overcomplete representations in the presence of noise. *IEEE Trans. Inf. Theory*, 52(1):6–18, January 2006.

[118] B. D. Rao and K. Kreutz-Delgado. Basis selection in the presence of noise. In *Proc. IEEE Thirty-Second Asilomar Conf. Signals, Syst., Comput.,*, volume 1, pages 752–756, 1998.

[119] J. Fuchs. Detection and estimation of superimposed signals. In *Proc. IEEE ICASPP*, volume 3, pages 1649–1652, 1998.

[120] E. Candès, J. Romberg, and T. Tao. Robust uncertainty principles: Exact signal reconstruction from highly incomplete frequency information. *IEEE Trans. Inf. Theory*, 52(2):489–509, Feburary 2006.

[121] E. Candès and T. Tao. Near-optimal signal recovery from random projections: Universal encoding strategies. *IEEE Trans. Inf. Theory*, 52(12): 5406–5425, December 2006.

[122] E. Candès, J. Romberg, and T. Tao. Stable signal recovery from incomplete and inaccurate measurements. *Communications on Pure and Applied Mathematics*, 59(8):1207–1223, 2006.

[123] D. Achlioptas. Database-friendly random projections: Johnson-Lindenstrauss with binary coins. *Journal of Computer and System Sciences*, 66(4):671–687, 2003.

[124] S. Cotter, B. Rao, K. Engan, and K. Kreutz-Delgado. Sparse solutions to linear inverse problems with multiple measurement vectors. *IEEE Trans. Signal Process.*, 53(7):2477–2488, July 2005.

[125] J. Tropp. Algorithms for simultaneous sparse approximation. Part II: Convex relaxation. *Signal Process.*, 86(3):589–602, 2006.

[126] Y. Eldar and M. Mishali. Robust recovery of signals from a structured union of subspaces. *IEEE Trans. Inf. Theory*, 55(11):5302–5316, November 2009.

[127] M. Hyder and K. Mahata. Direction-of-arrival estimation using a mixed $l_{2,0}$ norm approximation. *IEEE Trans. Signal Process.*, 58(9):4646–4655, September 2010.

[128] Yonghong Zeng, Ying-Chang Liang, Edward Chu Yeow Peh, and Anh Tuan Hoang. Cooperative covariance and eigenvalue based detections for robust sensing. In *Proc. IEEE Global Telecommunications Conference*, pages 1–6, 2009.

[129] P. Banerjee and T. Bezboruah. Some aspects of finite length dipole antenna design. In *Proc. of the World Congress on Engineering (WCE)*, volume 1, 2014.

[130] M. Lobo, L. Vandenberghe, S. Boyd, and H. Lebret. Applications of second-order cone programming. *Linear Algebra and Its Applications*, 284(1):193–228, 1998.